eman ta zabal zazu

Universidad
del País Vasco

Euskal Herriko
Unibertsitatea

A pre-targeting approach to boron neutron capture therapy: towards multipurpose boron-enriched therapeutic agents

Irene V. J. Feiner

Donostia-San Sebastián, **2020**

A pre-targeting approach to boron neutron capture therapy: towards multipurpose boron-enriched therapeutic agents

PhD thesis

to obtain the degree as Doctor of Philosophy in Chemistry
at the University of the Basque Country (UPV/EHU)

by

Irene V. J. Feiner

Donostia-San Sebastián, **2020**

Thesis superviser: Dr. Jordi LLop Roig (Radiochemistry and Nuclear Imaging Lab, CIC biomaGUNE)

University tutor: Prof. Dr. María Esther Lete Expósito (Department of Organic Chemistry, Faculty of Science and Technology, University of the Basque Country, UPV/EHU)

Table of Contents

Acknowledgments

It was my greatest pleasure to conduct the experimental work of my PhD at the CIC biomaGUNE research center, a multi-disciplinary center with outstanding facilities. For that opportunity I would like to thank Prof. Manuel Martín Lomas and Prof. Luis M. Liz-Marzán, former and current scientific directors of CIC biomaGUNE, respectively.

I would like to express my sincere appreciation and thanks to my research supervisor Dr. Jordi Llop! He was great support throughout my PhD with an always open door for questions, doubts and guidance when needed. His own fascination for the radiochemistry and nuclear imaging research field is contagious and I learned many new things every day. I'm very grateful that I could be part of his research group for the past 3 years of my PhD!

I would furthermore like to acknowledge my tutor Prof. Dr. Esther Lete from the University of the Basque Country (UPV/EHU), for her help and support.

A special thanks to Dr. Vanessa Gómez-Vallejo for her steady help and organization skills to make sure labs and experiments are running smooth.
A warm thanks to all my former and current colleges in the Radiochemistry and Nuclear Imaging Group together with the radiochemistry platform: Olatz, Luka, Unai, Ane, Kepa, Angel, Marcos, Rossana, Cristina, Ana, Pilar, Riccardo, Oscar, Ana B., Elisabetta, Cinzia, Victor, Xabi and Aitor. Especially to Zuriñe for her constant help and moral support and to Krishna, who was highly involved in my experiments. I feel happy and grateful that I could be part of this group of stunning people, thank you all for three amazing years!

Furthermore, I would like to thank everyone at CIC biomaGUNE who was involved in any kind making my thesis successful, especially platform members and animal facilities: Unai Cossío, Ainhoa Cano Garmendia, Ander Arrieta, Paola Ferreira Cabeza, Javier Calvo, Dorleta Otaegui Ansa, Irantzu Llarena, Daniel Padro and Desire Di Silvio.
I would also like to thank all the people of administration, maintenance, information technology and other supporting departments.

For the collaboration with Biodonostia in developing the breast cancer mouse model I'm deeply thankful to Prof. Charles Lawrie and Dr. María Muñoz Caffarel.

Yet, a big part of this PhD was the European Marie Curie ITN PET3D. Therefore, I first would like to thank our project manager Dr. Debbie McLaggan and the project coordinator Prof. Matteo Zanda. Furthermore, for the opportunity of secondments at the VUmc in Amsterdam and at the University of Aberdeen many thanks to Prof. Bert Windhorst, Dr. Daniëlle Vugts, Prof. Matteo Zanda and all their students who made me feel welcome and appreciated, especially to Marion and Beatrice for their help and contribution to my research.

Finally, I would like to take the opportunity to pronounce my deepest gratitude to my parents, my brother and sister and their families who always supported me throughout my life in every possible way!

Summary

Despite the effort, time and money contributed to treat cancer, it is still the second leading cause of death worldwide. Boron Neutron Capture Therapy (BNCT), which is able to balance high therapeutic efficacy with low undesired side effects, is a promising tool to treat cancer. BNCT is a binary approach where two components with low-toxicity require co-localization in tumor tissue to be activated as therapeutic agent. That is, high accumulation of boron-10 (^{10}B) in tumor tissue needs to be achieved and subsequently irradiated by thermal neutrons. A nuclear reaction will be triggered in which boron-10 captures a neutron and decays into lithium while releasing an alpha particle (^{10}B(n, α, γ)^{7}Li). The originated particles generate cellular damage which subsequently leads to cell death.

To achieve efficient and successful BNCT certain conditions need to be fulfilled. A physical challenge was the provisioning of neutrons in clinics, but newly developed accelerators, producing high intensity epithermal neutron beams, are now available. Furthermore, boron delivery agents able to deliver sufficient amounts of ^{10}B selectively into tumor tissue need to be produced. To date, only two compounds (sodium borocaptate (BSH) and boronophenylalanine (BPA)) are used in clinical trials, yet, their pharmacological limitations arise need for new and improved BNCT drugs.

Nanomaterials have been increasingly used in drug delivery due to their high loading abilities, low cytotoxicity and high bio-compatibility. Additionally, abnormal conditions in diseased tissue, such as inflammation or tumor growth, open the possibility of passive targeting for nanomaterials due to the enhanced permeability and retention (EPR) effect.

In the current PhD thesis, we have worked on the development of small, but highly boronated particles as ^{10}B carriers for the application in BNCT. Therefore, two different nanoparticles were developed and evaluated; one gold-nanomaterial based (AuNP) with a core diameter of 3 - 5 nm and one carbon based (carbon dots; CDs) with a core size of around 7 nm. Particles of small size come generally with the advantage of a rather fast clearance and elimination, hence, lower toxicity due to reduced organ and tissue uptake compared to bigger particles. However, high uptake in the diseased organ/tissue, such as a tumor, is desired. In this PhD we approached the challenge to achieve the balance between small and fast clearing particles but retention in tumor tissue by introducing a pre-targeting strategy.

The principle of pre-targeting is based on the high specificity of monoclonal antibodies (mAbs) towards their target. In tumor tissue such targets can be certain over-expressed cell membrane receptors. In our case we worked with breast cancer tumor models, using the antibody Trastuzumab (Herceptin®), which targets the membrane receptor HER2. For pre-targeting the antibody is functionalized with a moiety able to undergo a bioorthogonal click reaction (here *trans*-cyclooctene, TCO) with the drug delivery agent, itself functionalized with the counterpart for the click reaction (here tetrazine). The conjugated mAb is injected intravenously and after it is cleared from blood and healthy tissue, the drug delivery agent is administered. It clicks to the mAb in tumor tissue and is retained, whereas otherwhere fast eliminated.

The work of this thesis started with the functionalization of monoclonal antibodies and the analysis of the obtained conjugates. Besides TCO for the pre-targeting strategy, the chelator,

Summary

p-NCS-Bz-DFO (a desferrioxamine derivative) was used to enable the radiolabeling of the mAb with the positron emitter zirconium-89 (^{89}Zr) and thus the tracking of such *in vivo* by Positron Emissions Tomography (PET) imaging. The conjugation of both ligands was achieved by random conjugation, that is, by coupling reactions to free available amine groups of lysine residues in the mAb. This method is favored due to its mild reaction conditions together with rather easy and fast results. However, this non-site-specific method leads to a mixture with a high variety of conjugates. With the ratio of moieties per mAb playing an important role to determine the efficacy of the functionalized conjugate, we wanted to gain closer insight of the obtained mAb species. Therefore, three different analytical methods were used: (i) a direct titration method, (ii) MALDI/TOF MS (Matrix-Assisted Laser Desorption-Ionization / Time Of Flight Mass Spectrometry) and (iii) UPLC/ESI-TOF MS (Ultra High Performance Liquid Chromatography / Electrospray ionization - Time Of Flight Mass Spectrometry). The aim was to not only achieve the average number of moieties per mAb in the heterogenic mixture, but also to obtain a distribution of the different conjugates present. We, furthermore, wanted to answer the question if the number of moieties available on the surface of the mAb correlates with the total number of attached ligands by comparing the direct method (giving the available ligands) to mass analytic (giving the total number of ligands). For these investigations we used two different FDA and EMA approved mAbs: the above mentioned Trastuzumab and Bevacizumab (Avastin®, targets VEGF-A, a vascular endothelial growth factor). The study, described in Chapter 3, showed how challenging the analysis of antibodies, conjugated with a respectively small ligand, is. Direct titration offered quantitative results about the average number of functionalizations per mAb in all cases. MALDI/TOF MS showed in our hands questionable results, but UPLC/ESI-TOF MS offered the desired insight of the distribution of conjugates, with higher accuracy for DFO- compared to TCO-conjugates.

After the evaluation of the TCO-functionalized Trastuzumab for its binding affinity, biodistribution and internalization properties, we tackled the synthesis and characterization of small spherical gold nanoparticles (AuNPs), loaded with boron clusters, named COSAN (Cobalt *bis*[dicarbollide]), and functionalized with tetrazine to enable the click reaction. The particles, analyzed by transmission electron microscopy (TEM), showed homogeneous distribution, with a core size of 3-5 nm, increasing to 12-15 nm in diameter after functionalization. The AuNPs were radiolabeled by doping the gold core with [^{64}Cu]CuCl$_2$, allowing *in vivo* experiments while tracking the particles by PET imaging. Evaluating the distribution of the particles showed slower clearance than expected from such small particles, with high liver and spleen accumulation. The slow clearance from tumor tissue, with highest accumulation at 48 h post injection, limited improvement under pre-targeting conditions. Chapter 4 was concluded that the small AuNPs do not possess the desired properties for pre-targeting, yet, high boron loading was achieved and tumor uptake due to the EPR effect could be witnessed.

To overcome the hurdle of a slow clearing boron delivery agent as experienced with the AuNPs, we changed the type of particles from a metal core to organic boron carbon dots (B-CDs). This work is described in Chapter 5. High biocompatibility, low cytotoxicity and rather fast and inexpensive synthesis of carbon dots suggest their potential application as boron-10 delivery agents in the context of BNCT. Yet, to the best of our knowledge, B-CDs

have never before been investigated for BNCT. For the pre-targeting approach and *in vivo* studies, we functionalized with tetrazine and radiolabeled with a fluorine-18-prosthetic group ([^{18}F]FPyTFP), respectively. The distribution of the dots *in vivo* showed the desired fast clearance via kidney and bladder from all organs and tissue, including the tumor. When applying the pre-targeting strategy, the tumor accumulation was about 2.8 %ID/cm^3, but the desired retention in tumor tissue could be achieved. Hence, B-CDs, combined with a pre-targeting strategy, are promising new BNCT agents.

Resumen

A pesar del esfuerzo económico y humano destinado en las últimas décadas a combatir el cáncer, éste sigue constituyendo una de las principales enfermedades en el mundo desarrollado y representa la segunda causa de muerte a nivel mundial. Además, su incidencia se espera que aumente en los próximos años, debido a la mayor esperanza de vida, factores ambientales y hábitos poco saludables. Por este motivo, es imperativo desarrollar nuevas terapias que resulten más efectivas y produzcan menos efectos tóxicos y secundarios sobre los pacientes.

La terapia de captura de neutrones por boro (BNCT, del inglés *Boron Neutron Capture Therapy*) es una estrategia terapéutica binaria, que puede combinar *a priori* una elevada eficacia terapéutica mientras se minimizan los efectos secundarios. El principio de funcionamiento de la BNCT es sencillo en concepto y muy intuitivo, y se basa en la capacidad que presentan ciertos átomos, entre ellos el ^{10}B (el boro es un elemento con dos isótopos estables, ^{10}B y ^{11}B, con abundancias del 20 y 80%, respectivamente) de capturar neutrones térmicos. Dicha captura se traduce en la formación de un átomo de boro excitado, que se desintegra mediante fisión dando lugar a la formación de una partícula alfa y un ion de litio (reacción nuclear notada como ^{10}B(n, α, γ)^{7}Li). La partícula alfa y el ion litio tienen una energía elevada, y presentan una transferencia de energía lineal muy alta y un rango cercano al diámetro de una célula. De este modo, si se consigue acumular una cantidad suficiente de átomos de ^{10}B de manera preferente o selectiva en el tejido tumoral, y posteriormente éste se irradia con neutrones térmicos, la reacción de captura neutrónica y subsiguiente emisión de iones resulta en el daño y muerte celular en la zona tumoral. Aquellas zonas en las que no hay átomos de boro no se ven prácticamente afectadas por la terapia (Figura 1).
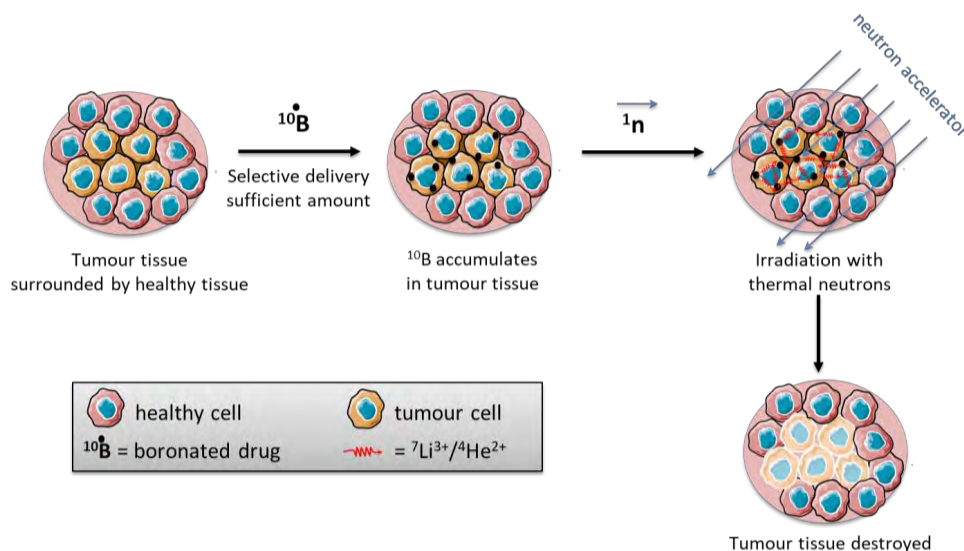
Figura 1: Principio de funcionamiento de la BNCT. Tras acumulación selectiva de átomos de ^{10}B en las células tumorales, se lleva a cabo una irradiación neutrónica, produciendo la reacción nuclear ^{10}B(n, α, γ)^{7}Li, que en última instancia produce el daño celular en el tumor, sin afectar al tejido sano.

Para lograr que la BNCT resulte eficiente y exitosa, es necesario que se den ciertas condiciones. En primer lugar, su aplicación se ha visto tradicionalmente limitada por la necesidad de acceder a fuentes de neutrones, que hasta hace pocos años requería llevar a

cabo las intervenciones en las inmediaciones de un reactor nuclear. Sin embargo, en los últimos años se han desarrollado ciclotrones que permiten obtener haces de neutrones de intensidad y energía adecuadas para llevar a cabo los estudios terapéuticos, facilitando por lo tanto la traslación al entorno clínico. El segundo problema relacionado con la BNCT es la necesidad de desarrollar entidades químicas capaces de acumular una cantidad suficiente de átomos de boro en el tumor, manteniendo baja la acumulación en tejido sano y en sangre. Generalmente, se acepta que una concentración de 25-30 µg de ^{10}B por gramo de tumor y una relación de concentración tumor/tejido sano y tumor/sangre de 4/1 son suficientes para garantizar eficacia terapéutica con efectos secundarios mínimos. Históricamente, se ha aprovechado el metabolsimo acelerado en los tumores y la sobre-expresión de determinados receptores para conseguir la acumulación preferencial de compuestos ricos en boro en el tejido tumoral. Sin embargo, y a pesar de más de 80 años de esfuerzo, en la actualidad tan sólo se utilizan en el entorno clínico dos compuestos: borocaptato de sodio (BSH) y boronofenilalanina (BPA), aunque ambos presentan poca especificidad por el tejido tumoral y sólo son eficaces en determinado tumores.

Con la emergencia de la nanotecnología, se han empezado a utilizar nanosistemas como potenciales portadores de boro con el fin de acumular una gran cantidad de boro en el tejido tumoral. De hecho, es posible preparar nanomateriales con alta biocompatibilidad y larga circulación en sangre. Además, gracias al efecto conocido como *enhanced permeability and retention* (EPR) los nanosistemas se acumulan de manera preferente en los tumores, ya que los tumores presentan una vasculatura imperfecta con fenestraciones y un drenaje linfático deficitario.

En esta tesis doctoral se ha combinado la experiencia previa adquirida en el grupo de investigación de Radioquímica e Imagen Nuclear relativa a (i) nanotecnología; (ii) química del boro; y (iii) imagen nuclear y experimentación animal, para abordar la implementación de una estrategia de pre-targeting basada en nanotecnología para su aplicación en BNCT. Concretamente, se ha trabajado en el desarrollo de partículas pequeñas y ricas en boro. Por un lado, se han desarrollado y evaluado nanopartículas de oro (AuNP) con un diámetro de núcleo de 3 - 5 nm, y por otro lado nanopartículas de carbono (CDs, del inglés *carbón dots*) con un tamaño de núcleo de alrededor de 7 nm. Se eligieron nanopartículas (NPs) de pequeño tamaño ya que éstas presentan generalmente un aclarado relativamente rápido y poca acumulación en los órganos del sistema reticuloendotelial (RES), actualmente conocido como MPS (del inglés *Mononuclear phagocytic system*). Esto resulta en una menor toxicidad ya que hay menos acumulación en tejido sano. Es importante mencionar que un aclarado rápido también se traduce en una menor biodisponibilidad. En consecuencia, uno de los retos de esta tesis doctoral consistía precisamente en conseguir un equilibrio entre el aclarado del organismo y la acumulación en el tejido tumoral.

La novedad principal de la presente tesis doctoral se basa en la utilización de la estrategia de *pre*-targeting para conseguir la acumulación en tumor. Dicha estrategia es conocida y ha sido utilizada en el contexto de la imagen molecular, pero no de la terapia. El *pre*-targeting se basa en conseguir la acumulación de un fármaco (componente 2) utilizando para ello la acumulación previa de otro componente (componente 1). El componente 1 se acumula en el tumor gracias a una interacción específica, como puede ser la unión a un receptor

determinado que se encuentra sobre-expresado en células tumorales. En el caso de la tesis doctoral, se ha utilizado como componente 1 un anticuerpo (mAb), concretamente Trastuzumab (Herceptin®), que tiene gran afinidad por los receptores de membrana HER2. Dicho anticuepro se funcionalizó con un ligando capaz de producir una reacción bioortogonal (trans-ciclooceno, TCO). El componente 2, en nuestro caso las NPs ricas en boro, se funcionalizaron con el grupo complementario para dar la reacción bioortogonal (en este caso, tetrazina). Para llevar a cabo la estrategia de *pre-targeting* se inyecta en primer lugar el mAb funcionalizado por vía intravenosa. Una vez se ha producido la acumulación en tumor y el aclaramiento de la sangre y tejido sano, se administra el componente 2, que se distribuye por todo el cuerpo pero se acumula únicamente donde es capaz de producirse la reacción bioortogonal con el componente 1, es decir en el tumor (Figura 2).
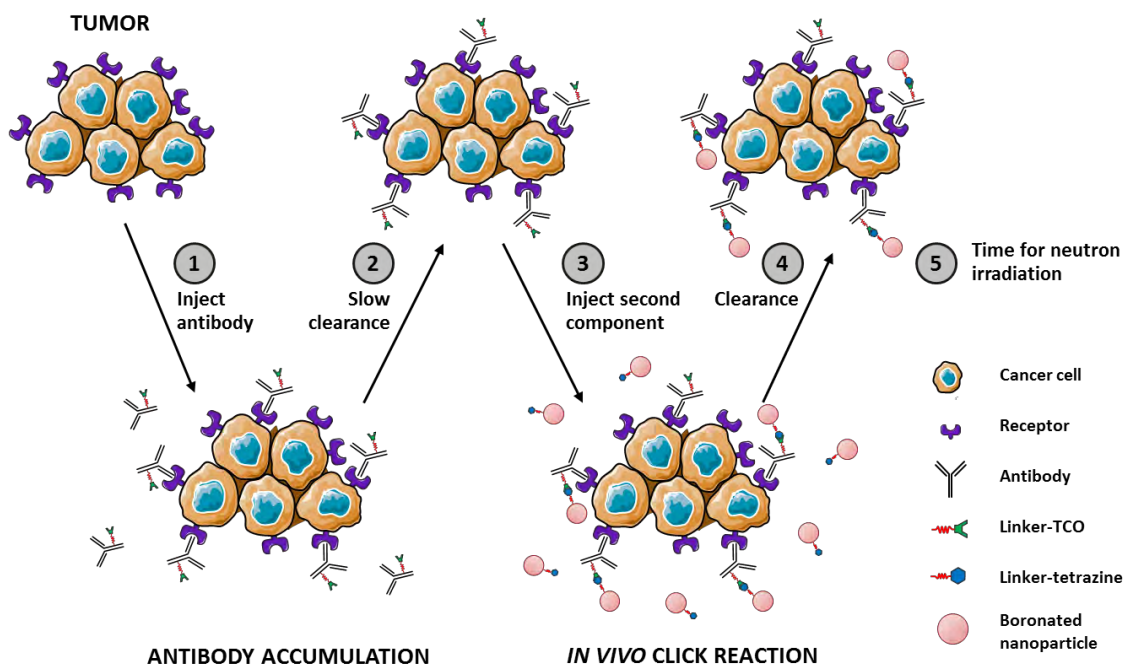
Figura 2: esquema de la estrategia de pre-targeting. En primer lugar, se administra un anticuerpo funcionalizado con un grupo capaz de dar lugar a una reacción bioortogonal (1). Una vez se ha producido la acumulación en tumor y aclaramiento (2) se administra el segundo componente (3), que en este caso es una nanopartícula con una funcionalidad capaz de dar la reacción bioortogonal. La reacción bioortogonal entre los dos componentes se da únicamente en el tumor, produciendo la acumulación del segundo componente (4), momento en el que debería llevarse a cabo la irradiación neutrónica (5).

El trabajo de esta tesis se inició implementado metodologías para la funcionalización de los anticuerpos y el análisis de los conjugados obtenidos (capítulo 3). Además del TCO, necesario para dar la reacción bioortogonal, se decidió incorporar un quelante bifuncional, concretamente p-NCS-Bz-DFO (un derivado de la desferrioxamina) con el fin de permitir el marcaje radiactivo utilizando el isótopo emisor de positrones zirconio-89 (^{89}Zr), que permitiría de este modo su seguimiento tras administración *in vivo* utilizando tomografía por emisión de positrones (PET). La conjugación de ambos ligandos simultáneamente se logró mediante la conjugación aleatoria, es decir, mediante reacciones de acoplamiento a grupos amino disponibles, debido a la presencia de lisinas en el mAb. Este método es muy atractivo ya que requiere unas condiciones de reacción suaves resulta muy sencillo. Sin embargo, se

trata de un método no específico, y en consecuencia no se conocen *a priori* ni el número ni la distribución de las funcionalidades incorporadas, resultando generalmente en mezclas de conjugados. Así pues, el primer objetivo de la tesis doctoral fue establecer métodos analíticos para una correcta caracterización de los mAbs funcionalizados, con el fin de conocer el número de funcionalizaciones promedio, así como conocer mejor la distribución de mAbs con cada número de funcionalizaciones, y el número de dichas funcionalizaciones que están "disponibles" para una eventual reacción de formación del complejo (caso del DFO) o de reacción bioortogonal (caso del TCO). Con tal fin, se utilizó una combinación de métodos analíticos, incluyendo: (i) un método de valoración directa, (ii) MALDI/TOF MS (*Matrix-Assisted Laser Desorption-Ionization / Time Of Flight Mass Spectrometry*) y (iii) UPLC/ESI-TOF MS (Cromatografía Líquida de Ultra-resolución / Ionización de Electrospray - Espectrometría de Masa de Tiempo de Vuelo). Para estas investigaciones, se utilizaron dos mAbs aprobados por la FDA y la EMA diferentes: el mencionado anteriormente Trastuzumab, y Bevacizumab (Avastin®, que es específico para el factor de crecimiento endotelial vascular VEGF-A. Los métodos de valoración directa permitieron obtener datos cuantitativos acerca del número de funcionalizaciones promedio por mAb. La técnica de MALDI ofreció resultados algo ambiguos, debido a la poca resolución de la técnica y a la pequeña masa molecular de las funcionalizaciones incorporadas, que impidieron una correcta resolución de las diferentes señales. Por contrapartida, la técnica UPLC/ESI-TOF MS permitió obtener datos cuantitativos fiables acerca de la presencia de diferentes grados de funcionalización, especialmente en el caso del DFO.

Una vez caracterizada la funcionalización del Trastuzumab, se abordó el trabajo relativo al desarrollo de nanosistemas y su evaluación *in vivo*. En primer lugar se ensayó la síntesis y caracterización de nanopartículas de oro esféricas (AuNP), cargadas con clústeres de boro. Concretamente, como unidad rica en boro se utilizó el COSAN (Cobalto bis[dicarballuro]), que es un complejo mixto de cobalto que integra dos clústeres de carborano, cada uno de ellos con 9 átomos de boro y con carga global negativa. Asimismo, se incorporó a las NPs ligandos funcionalizados con tetrazina, con el fin de permitir la reacción bioortogonal con el TCO. Las partículas se analizaron mediante microscopía electrónica de transmisión (TEM), que demostró una distribución homogénea de tamaño de núcleo (3-5 nm). El marcaje de las NPs para su posterior evaluación mediante PET se llevó a cabo mediante dopaje del núcleo de oro utilizando el isótopo emisor de positrones cobre-64. La evaluación de la distribución de las partículas se llevó a cabo en un modelo animal de cáncer de mama, generado mediante inoculación subcutánea de células BT-474 en ratones inmunodeprimidos. Los estudios de imagen mostraron un aclarado de las NPs más lento del esperado, con alta acumulación de hígado y bazo. Esto resultó en una baja biodisponibilidad, y en consecuencia también en una baja acumulación tumoral. Posteriormente, se ensayó la estrategia de *pre-targeting*. Para ello, se ensayó en primer lugar la biodistribución del anticuerpo funcionalizado y marcado con ^{89}Zr, observándose una buena acumulación en el tumor a las 24-48 horas tras la administración intravenosa (Figura 3). Puesto que los estudios *in vivo* e *in vitro* llevados a cabo demostraron que se producía la internalización del anticuerpo en las células tumorales, se decidió abordar los estudios de *pre-targeting* administrando el componente 2 (NPs de oro) a las 24 horas tras la administración del anticuerpo. De este modo, se adquirió un compromiso entre la acumulación en tumor, el aclarado de sangre y tejido sano, y la posible internalización del

mAb, que en última instancia reduce la probabilidad de que se produzca la reacción bioortogonal en el tumor. Los estudios llevados a cabo demostraron que la acumulación de las NPs en el tumor no es superior cuando se utiliza la estrategia de *pre-targeting*, cuando se compara con la acumulación alcanzada con las NPs inyectadas individualmente. La falta de resultados positivos se interpretó en términos de la retención de las NPs en el tumor. Puesto que dicha retención es alta, tal y como se observó en los estudios llevados a cabo sólo con las NPs, no se observa una mejora cuando se aplica la estrategia de *pre-targeting*.
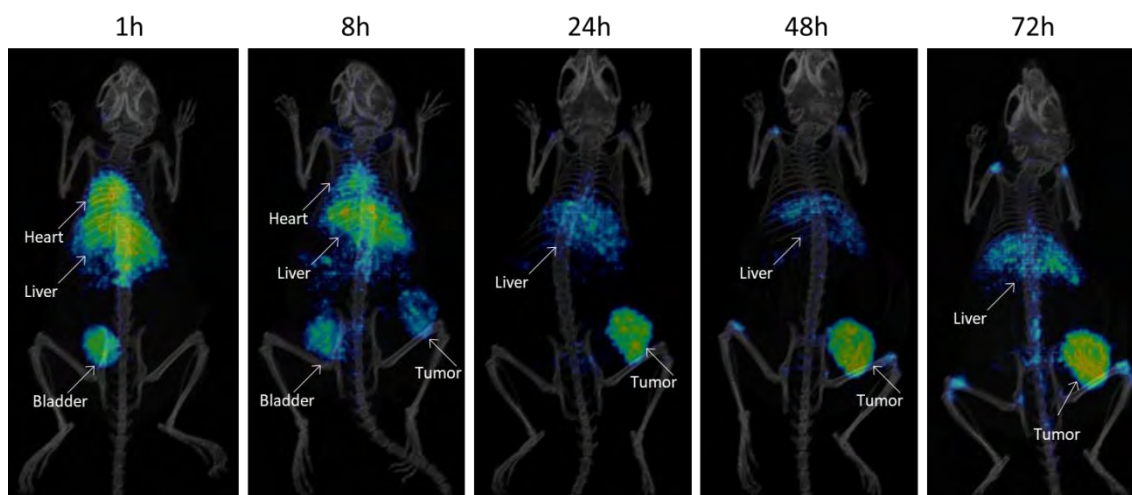

Figura 3: Imágenes PET obtenidas a diferentes tiempos tras administración de Trastuzumab funcionalizado y marcado con ^{89}Zr, en un modelo animal de cáncer de mama generado por inoculación subcutánea de células BT-474 en ratones inmunodeprimidos.

Para superar el obstáculo que supone el aclaramiento lento de las NPs, se optó porsteriormente por ensayar nanosistemas de menor tamaño, concretamente nanopartículas de base carbono, conocidas habitualemnte como *carbon dots* (CDs), dopadas con boro (B-CDs). Se escogieron estos nanosistemas ya que presentan una elevada biocompatibilidad, baja citotoxicidad y su síntesis es relativamente rápida y económica. La estrategia planteada fue la misma que la expuesta anteriormente para las NPs de oro. Sin embargo, en este caso se utilizó como componente 2 de la estrategia de *pre-targeting* los mencionados B-CDs, preparados para presentar grupos amino libres sobre la superficie, los cuales se aprovecharon para incorporar las unidades de tetrazina (con el fin de permitir la reacción bioortogonal) y el radiomarcaje, el cual se logró utilizando el grupo prostético [^{18}F]FPyTFP, que presenta alta reactividad hacia los grupos amino.

Los ensayos efectuados con los B-CDs mediante PET en el mismo modelo animal anteriormente mencionado demostraron un aclaramiento y eliminación vía orina muy rápidos según lo esperado, y una acumulación baja en el tumor. Al ensayar la estrategia de *pre-targeting*, se obtuvo un patrón de biodistribución muy parecido, con una eliminación rápida y una baja acumulación en el tumor. Sin embargo, un análisis más exhaustivo de la acumulación de los B-CDs en tumor en función del tiempo demostró que, mientras que la concentración de B-CDs en el tumor disminuye con el tiempo en el grupo control (administración únicamente de los B-CDs), dicha concentración se mantiene constante en condiciones de *pre-targeting*. Este resultado demuestra una mayor retención de los nanosistemas cuando el experimento se lleva a cabo en condiciones de *pre-targeting*, y

corrobora que la reacción bioortogonal se produce (Figura 4). Los resultados sugieren que la estrategia es válida, si bien para un funcionamiento óptimo podría ser adecuado seleccionar un anticuerpo con menor internalización celular, y aplicar el segundo componente de la reacción a tiempos más largos. Así mismo, una mayor circulación (eliminación más lenta) del segundo componente (nanosistema) ofrecería también mejores resultados.
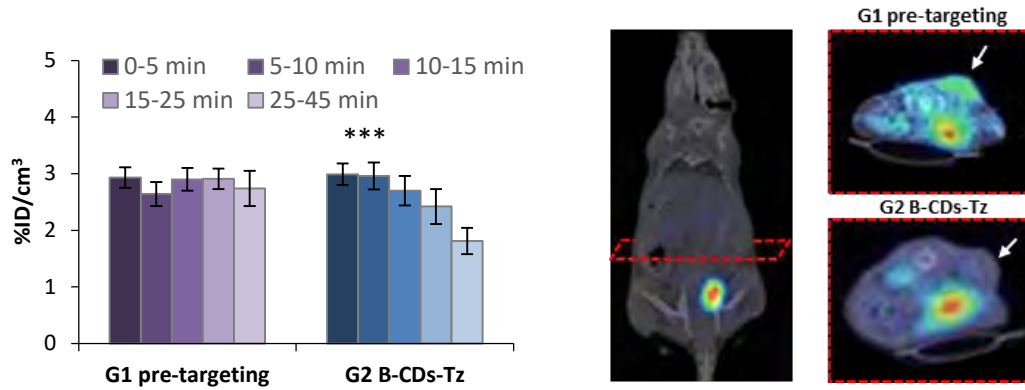
Figura 4: Izquierda: Concentración de B-CDs en el tumor a diferentes tiempos tras administración intravenosa en un modelo animal de cáncer de mama. En violeta, resultados obtenidos en condiciones de *pre-targeting*. En azul, concentraciones obtenidas tras administración únicamente de los B-CDs; derecha: imágenes PET-CT representativas de cuerpo completo, y de acumulación selectiva en la zona tumoral en condiciones de *pre-targeting* (arriba) y de no *pre-targeting* (abajo).

Chapter 1: General introduction

1.1 Cancer

The term cancer embraces different diseases which can affect any part of the body. All in common have a (mostly) fast growth of cells out of their usual behavior. They penetrate into surrounding tissue, forming a tumor. Some cancer types even spread to other organs to form metastases. This stage usually leads to an immense increase of the death rate. In Figure 1 the incidence and mortality of the most common types of cancer worldwide are shown (2018):
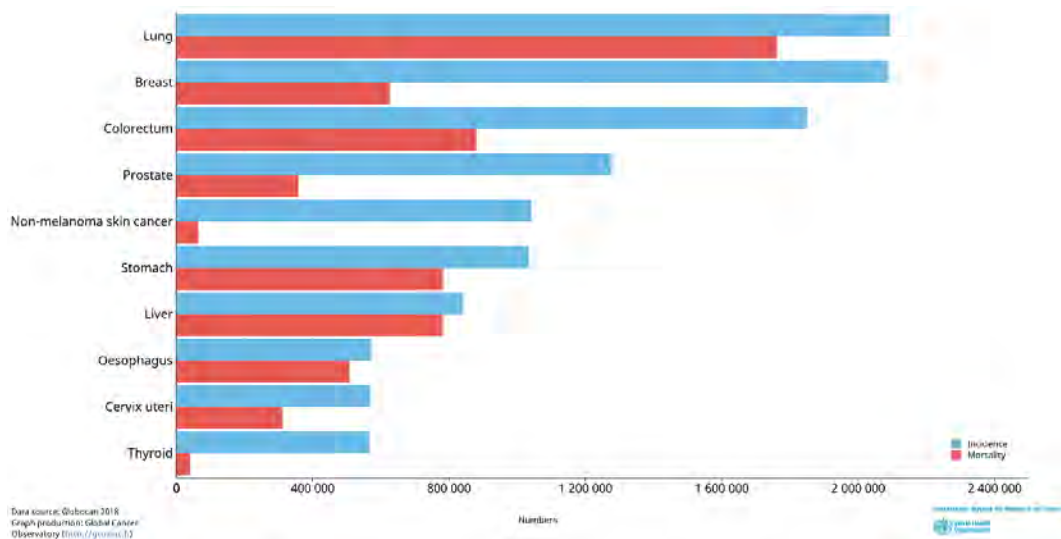
Figure 1: Estimated number of incident cancer cases and deaths worldwide in 2018 (both sexes, all ages) (1).

As the second leading cause of death worldwide (about 1 out of 6 deaths), cancer was responsible for an estimated 9.6 million deaths in 2018. The highest risk factors leading to cancer (about 30 % of all cases) are overweight, a lack of fruit and vegetables in diet, too little physical activity as well as the use of tobacco and alcohol. Whilst in 2017 in high-income countries 90 % reported treatment services are available, in low-income countries it´s only 26 % (2).

The major difficulties of curing cancer are not only the variety of the different kinds of tumors but also the late-stage presentation and inaccessibility for diagnosis and treatment. Therefore, the development of new therapies and improvement of existing ones is required where therapeutic efficacy and harmful side effects are carefully balanced.

1.2 Boron neutron capture therapy

1.2.1 General discription

Boron neutron capture therapy (BNCT) is a unique way to treat cancer. It is a binary approach where two non- or low-toxic components require co-localization in tumor tissue to become effective. In the process, a compound enriched with stable boron-10 (approximately 20 % of the natural element boron) is injected intravenously and accumulates in tumor tissue. A neutron beam, directed to the affected tissue, leads to a nuclear reaction of boron-10 (^{10}B) into a recoiled lithium nucleus ($^{7}Li^{3+}$) and an alpha particle ($\alpha = {}^{4}He^{2+}$)

(Figure 2). The high cross section of Boron-10 atoms (σ = 3840 barns) enables the capture of thermal neutrons and hence, the nuclear reaction $^{10}B(n,\alpha,\gamma)^7Li$. Gordon Locher proposed this principle first in 1936 (3).
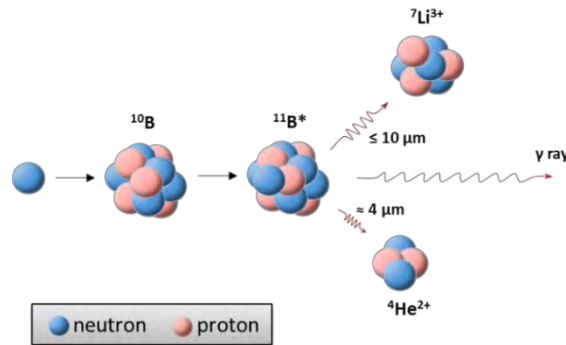
Figure 2: Nuclear reaction in BNCT. ^{10}B is capable to capture thermal neutrons, resulting in the formation of an unstable ^{11}B atom which ultimately disintegrates with the consequent emission of one alpha particle, one lithium ion and one gamma ray.

The particles released following neutron capture are highly charged and have a high molecular weight. Those properties result in a high linear energy transfer (LET); that is, they can release a high amount of energy to the material traversed per unit distance. Therefore, the pathway is short with a fast loss of energy, producing a severe damage to the environment. Exactly these properties are used in BNCT. The emitted ions, when selectively or preferentially accumulated in tumor tissue, will induce severe damage on a length range smaller than the diameter of a single cell (4-10 μm, Figure 2) (4) and tumor cells will be destroyed while the surrounding healthy tissue is spared (Figure 3). Selectivity also refers to the fact that no other main constituent elements of the body, i.e. oxygen, nitrogen and carbon, have a high cross section for neutrons. Nitrogen and hydrogen are able to capture neutrons (nuclear reactions: $^{14}N(n,p)^{14}C$ and $^1H(n,y)^1H$) with σ = 10^{-24} barns, which is negligible when compared to ^{10}B cross section (3840 barns). Nevertheless, this feasibility limits the strength of the neutron beam due to the abundance of these elements (5).

Figure 3: The principle of BNCT. If boron atoms can be selectively accumulated in tumor cells, neutron irradiation results in the emission of ionizing particles which result in tumor cell damage while sparing healthy tissue.

For boron to be able to capture a neutron, the neutrons need to have low energy (thermal neutrons; E < 0.5 eV) when reaching the boron atoms. However, thermal neutrons only have a very limited depth of penetration into tissue (3-4 cm) and are only of use for skin tumors like melanoma. No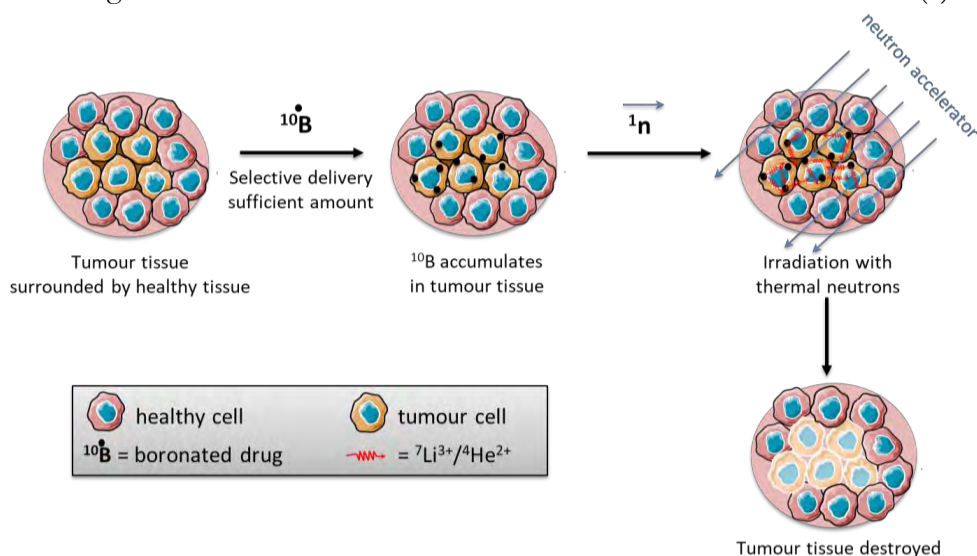wadays neutrons with higher energy (epithermal neutrons, > 0.5 eV < 10 keV) are used for the beam. They lose energy during the penetration (8 cm) of the tissue and reach the boron enriched compound with the energy of thermal neutrons (5).

The advantages of BNCT are the high efficiency, high selectivity towards tumor tissue and a high chance to target multicentric deposits of tumors at the same time. However, these features can only be reached by a high dose gradient between cancer cells and healthy tissue. Recent research is focused on (i) the availability of neutrons via neutron accelerators to enable BNCT away from nuclear reactors; (ii) the optimization of neutron penetration into tissue; and (iii) delivering a sufficient amount of boron-10 while keeping the ratio between tumor and normal tissue high to guarantee low background and therefore minimize side effects.

1.2.2 Boron delivery agents - general requirements

Many requirements are given for a successful boron delivery agent besides low toxicity. It needs to be able to deliver a sufficient amount of boron into the tumor tissue. The aim is to reach at least 20 μg ^{10}B/g tumor (~10^9 atoms/cell). On the other hand, the uptake of boron in other tissue should be low, obtaining a ratio of ≥ 5 between tumor to normal tissue and tumor to blood. Furthermore, a rapid clearance from blood and normal tissue is desired, but persistence in tumor until and during neutron irradiation should happen (5). The development of boron-10 delivery agents capable to selectively accumulate in tumor cells at a therapeutic dose still remains a major challenge.

1.2.3 From history to recent research

In 1932 Chadwick discovered the neutron which was the fundament for Locher to describe in 1936 the principle of a neutron capture therapy for cancer (6). However, the first actual performance of a BNCT trial on a malignant glioma was not conducted until 1951, when finally, the graphite research reactor in Brookhaven was available as neutron source (4).

The very first compounds to deliver ^{10}B into tumor tissue were in the 1950s boric acid and its derivatives. However, they are non-selective and have a very low retention time in tumor tissue (see Table 1). The second generation of boron delivery agents was developed in the 1960s. The compounds were boron-rich bio-molecules with low molecular weight, such as carbohydrates, amino acids, nucleic acids and small peptides. The advantages were the low toxicity and an increased residence time in the tumor when evaluated in animal models. The only two BNCT delivery agents currently used in clinical trials are from that second generation. Sodium mercaptoundecahydro-closo-dodecaborate (Na$_2$B$_{12}$H$_{11}$SH), commonly known as sodium borocaptate (BSH), and the boron containing amino acid (L)-4-dihydroxy-borylphenylalanine, known as boronophenylalanine (BPA) (Figure 4) (7; 8; 9). However, none of them fulfills the required criteria as described above. Most commonly used for high grade gliomas and recurrent head and neck cancer (7), their main drawback is, besides low

selectivity and retention time, a high variety in tumor uptake among tumor regions as well as between patients (10).

Figure 4: Chemical structures of sodium Borocaptate (BSH, left) and boronophenylalanine (BPA, right); currently the only compounds used in the clinics.

For further improvement, compounds have to be enriched with a number of boron atoms as high as possible, in order to deliver a sufficient amount into tumor tissue. One alternative to achieve this is to attach one or more polyhedral borane anions or carboranes (boron clusters) to small, tumor targeting bio-molecules or to monoclonal antibodies. One such boron cluster analogue is the so called COSAN (cobalt bis(dicarbollide)), which is a metallocarborane in which a cobalt atom is sandwiched between two carboranyl clusters (11). The net charge of the complex, which is delocalized over the whole cluster, is -1, which makes COSAN an amphiphilic compound (Figure 5).
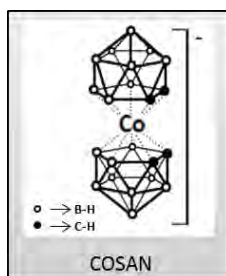
Figure 5: Structure of COSAN.

This third generation of delivery agents was hence able to transfer a higher amount of ^{10}B into the tumor when coupled to targeting moieties (9; 10; 12). In Table 1 an overview of the three generations of boron delivery agents is shown.

Table 1: Progress of delivery agents since the 1950th with boric acid derivatives as first generation. The second generation refers to boron-rich bio-molecules with low molecular weight, whereas the third generation uses boron cluster for higher boron loadings.

	First Generation	Second Generation	Third Generation
Example	Boric acid	Boronated amino acid (BPA)	Carbohydrate with boron cluster

Further progress focused on the fact that the effect of BNCT is proportional to the number of ^{10}B atoms accumulated in tumor cells. Hence, macromolecules such as polymers and dendrimers (Figure 6) containing a high number of boron atoms were developed and linked to targeting vectors (10; 13). These compounds were finally close to all the requirements to

become promising BNCT drug candidates. However, all of them present certain limitations and none of them has replaced BPA and BSH, which are still the two main compounds used in clinical practice. Hence, there is still room for improvements: the side effects, which occur mainly through insufficient tumor-to-healthy tissue ratios, still need to be reduced. Additionally, compounds capable to accumulate a high amount of ^{10}B atoms in different types of tumors still need to be developed.
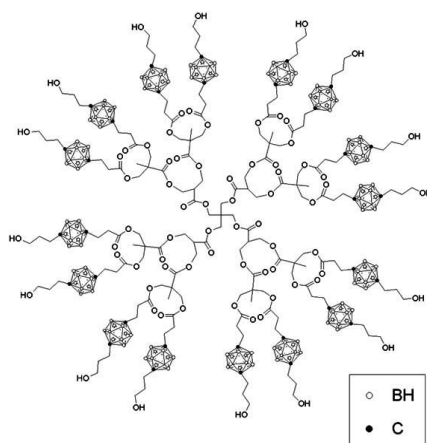
Figure 6: Example of a heavy boronated dendrimer (13).

1.2.4 Nanomaterials as boron delivery agents

Nanoparticles (NPs) can be defined as particles with a size lower than 100 nm in at least one dimension. Due to their small size, their physic-chemical properties differ from bulk materials. Additionally, NPs present a high surface to volume ratio, can be functionalized with a wide range of molecules and loaded with significant amount of cargo. Because of this, they have emerged as key elements in the drug development pipeline. This fact is even more relevant in oncology, where the differences between tumor and healthy tissue allow passive targeting by the enhanced permeability and retention (EPR) effect. EPR is based on the nature of most tumors to grow fast, which results in the need to change tissue conditions. Angiogenesis, the growth of additional blood vessel out of existing ones, is present. However, these new vessels are leaky, the permeability for NPs from blood to tissue is enhanced, and also the lymphatic system is less developed which leads to a prolonged retention time of NPs in tumor tissue (Figure 7) (14; 15).
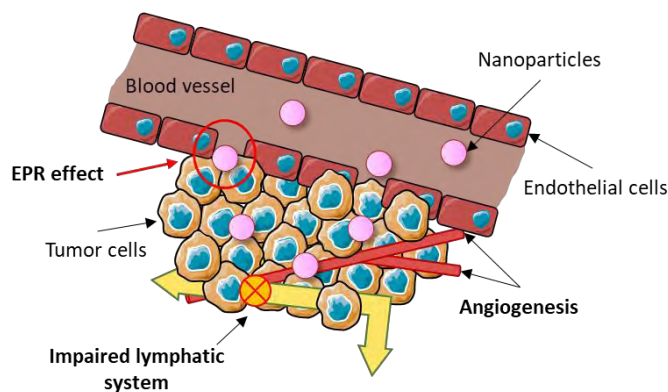
Figure 7: EPR effect. The process of neoangeogenesis occurring in tumors results in leaky vasculature with an immature lymphatic drainage, facilitating penetration of nanoparticles from blood into the tissue and prolonged retention.

The emergence of NPs in biomedicine has also impacted BNCT, and nanosystems have gained attention as boron delivery agents. The idea is to achieve a high boron loading, a longer circulation half-life and passive tumor targeting through the EPR effect. Liposomes, as example, are able to carry small boronated molecules both in their lipophilic bilayer and/or in their hydrophilic core (Figure 8, left) (16). Also, Micelles and other nanomaterials like carbon nanotubes (Figure 8, right) (17) and silicon nanowires are in research. In this project, however, gold nanoparticles as well as boron carbon dots are chosen as delivery agents.
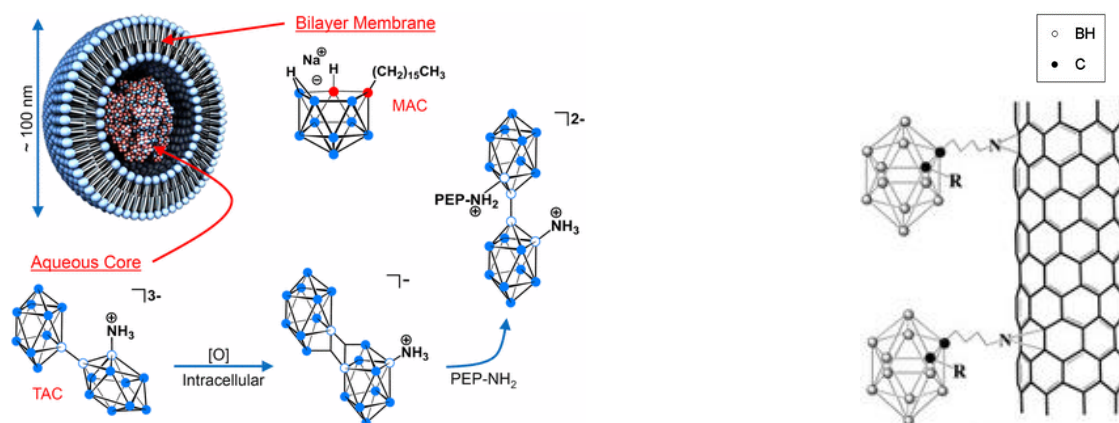

Figure 8: Left: Liposome, containing boronated molecules (16), right: boron cluster on a carbon nanotube (adapted from (17)).

1.2.4.1 Gold nanoparticles

Gold nanoparticles (AuNP) are one of the key materials in biomedicine. They are suitable as drug delivery agents for several reasons. They are biocompatible, have low toxicity, are tunable in shape and size (which affects their biodistribution) and easy to functionalize with high loadings on their surface (18). There are, among others, spherical NPs, nanorods (NR) and gold stars which can be easily modified on their surface by a covalent sulfide bonding. To influence the circulation time, surface and charge of the particles can be modified. Positively charged particles have a higher rate of internalization, whereas negatively charged particles typically show a longer blood circulation time (19). Another advantage is the possibility to synthesize AuNP in aqueous solutions, which makes the transfer to physiological media easy. Many different strategies have been reported for the preparation of AuNP (20), being the most commonly employed the direct reduction of chloroauric acid ($HAuCl_4$) in the presence of e.g. sodium borohydride or citrate, which results in the formation of nearly monodisperse AuNP in sizes up to 200 nm (21).

In this work we focused on small spherical AuNPs (core: 3-5 nm, shell: 10-15 nm) loaded with COSAN (see 1.2.3 From history to recent research). The low size results in a high surface area to volume ratio which allows heavy loading with therapeutic agents next to other functionalization. Furthermore, the biodistribution of smaller particles show increased accumulation and penetration into tumor tissue through the EPR effect (14).

1.2.4.2 Carbon Dots

Carbon dots (CDs) are part of the carbon allotrope family and have gained increasing attention since their discovery in 2004 by Scrivens *et al.* (22). They are quasi-spherical, smaller than 10 nm in size, low in cytotoxicity and high in biocompatibility. They consist primarily

of carbon next to hydrogen, oxygen and nitrogen. The benefits of CDs are their optical characteristics with an intense fluorescence together with flexible physio-chemical properties (e.g. hydrophilic or hydrophobic) due to variations in their synthesis and varying functional groups on the surface, leading to a broad field for application like metal detection, solar cells and biological approaches such as drug delivery agents (23). Another advantage besides their flexibility is a rather easy, usually one step synthesis via microwave out of relatively inexpensive compounds such as citric acid and ethylene diamine.

Even though, the detailed mechanism of the formation of CDs is still unclear and surely different for each type of dots. However, it is commonly accepted that the major steps are polymerization of the single compounds followed by carbonization and formation of the CDs (Figure 9) (23). The most common functional groups left on the surface on hydrophilic CDs are carboxyl-, hydroxyl- and/or amino- groups (24).
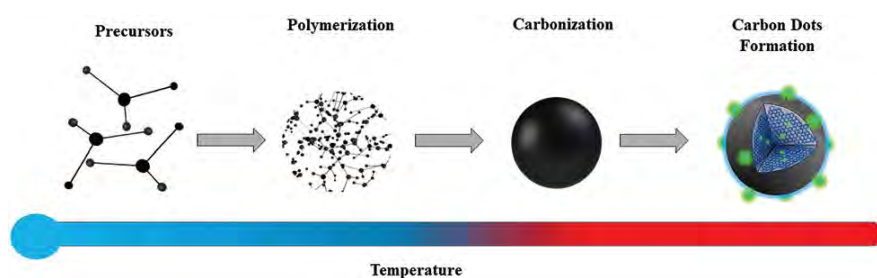
Figure 9: Schematic mechanism of CDs formation (23).

In this work we focused on hydrophilic CDs due to the advantage that physiological buffers can be used as solvents and therefore, the particles can be used in biological systems. Other than the AuNPs, where boron was attached at the surface of the particles, carbon dots can be doped with boron, forming so called Boron Carbon Dots (B-CDs), using e.g. sodium tetraborate to form the core of the particles.

1.3 Pre-targeting

1.3.1 Bioorthogonal 'click' reaction

Pre-targeting is based on a certain type of a chemical reaction which can occur *in vivo*, the bioorthogonal 'click' reaction. A coupling reaction *in vivo* needs to fulfill very specific properties. Certainly, nontoxicity of the reaction compounds but also of any possible side products generated by the coupling reaction. Furthermore, the reaction needs to be optimized for aqueous medium at the temperature of 37 °C. To gain good yields in biological systems a fast reaction rate which enables the coupling reaction even with very low concentrations is essential. If the reaction additionally does not interfere with any other native biochemical processes, it belongs to the field of bioorthogonal chemistry.

Recently several such reactions were investigated and described (25; 26; 27). But one of these showed outstanding qualities: The inverse-electron-demand Diels Alder coupling between a tetrazine derivative (Tz, diene) and a *trans*-cyclooctene (TCO, dienophile) derivative (Figure 10) (28). Opposite to most click reactions described so far, this reaction does not need a catalyst. Moreover, the only by-product is N_2, which is nontoxic, and high yields are reached at an incredible speed (reaction rate constant of k = 2000 $M^{-1}s^{-1}$).
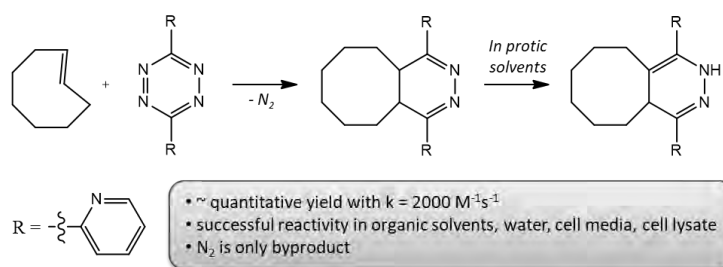
Figure 10: Scheme of an inverse-electron-demand Diels Alder reaction, example from (29).

1.3.2 The principle of pre-targeting

The origin of the pre-targeting strategy arose in the field of radioimmunology where a radiolabeled monoclonal antibody (mAb) accumulates in tumor tissue by binding to a specific target. This way, depending on the radionuclide, either imaging or therapy can be performed. However, one major drawback is a high radiation dose for the patient due to slow distribution and clearance (days) of mAbs from blood and healthy tissue. To prevent negative side effects by radiation doses to non-tumor tissue, the strategy of pre-targeting was introduced (15; 28; 30; 31). In such a strategy, a functionalized mAb, which is enabled to undergo a bioorthogonal 'click' reaction is injected intravenously. After its accumulation in tumor tissue and clearance from blood and healthy tissue, a small molecule carrying the radionuclide is injected. This small compound distributes and clears fast from the body. However, passing through the tumor it will 'click' to the antibody and remain, resulting in high sensitivity and low background signal (Figure 11).

In the context of pre-targeting, there are certain key factors that need to be taken into consideration: (i) a high, selective (or preferential) accumulation of the mAb in the target tissue (in this case, the tumor) is required; (ii) the second compound, capable to undergo the bioorthogonal click reaction with the mAb, needs to be injected once the mAb is cleared from the blood, in order to avoid the click reaction to occur in the blood, which would prevent the reaction taking place in the tumor; and (iii) the second compound needs to clear fast from the body. In the context of imaging, this results in a decrease of background signal and hence enhances image quality and sensitivity. In the context of therapy, the fast clearance prevents high radiation dose in healthy tissue. In most cases, the pre-targeting strategy does not result in higher accumulation than direct targeting, although higher tumor to healthy tissue ratios can be achieved.
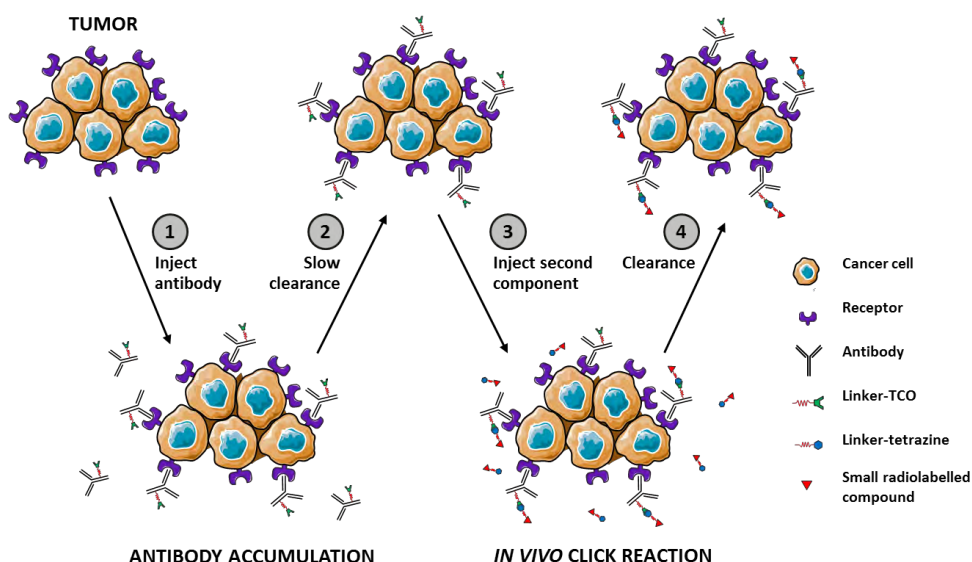
Figure 11: Original pre-targeting strategy. First, a functionalized mAb is administered, which accumulates in the tumor tissue (1). After clearance of the unbound mAb (2), the second component is administered (3), and the bioorthogonal reaction occurs in the tumor (4) with consequent entrapment.

Because of the above-mentioned requirements, the second component is typically a small molecule. However, in this work we envisaged the possibility to apply the pre-targeting strategy from a slightly different perspective. Our idea was based on the following rationale: First, a TCO-functionalized mAb is administered and accumulates in tumor tissue by binding to an overexpressed receptor. After the slow clearance, fast clearing boron loaded NPs (AuNPs or B-CDs) functionalized with tetrazine moieties (to enable the click reaction with TCO-functionalized mAbs) are injected. By the time that a high concentration of particles had reached the tumor tissue and cleared from other tissue, the irradiation with neutrons can take place to initiate the nuclear reaction of ^{10}B into ^{7}Li^{3+} with the release of alpha particles which leads to the desired cell death in tumor tissue (Figure 12).
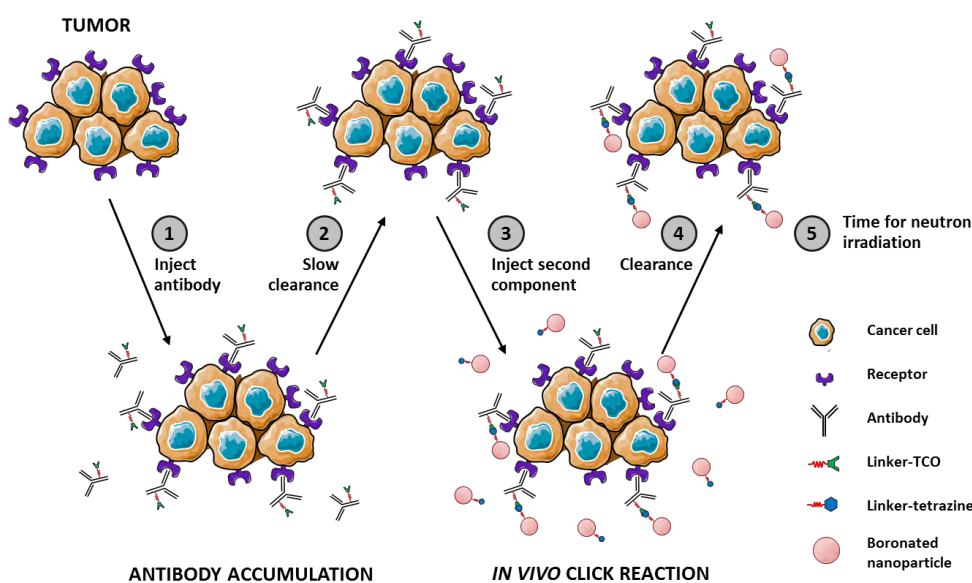
Figure 12: Pre-targeting strategy using highly boronated nanoparticles as second component.

1.3.3 Why pre-targeting?

Delivery agents, such as NPs, should have a sufficient size, to ensure uptake and retention in the desired tissue like a tumor (32). However, this property is non-specific and therefore the retention is also prolonged in other tissues such as the liver which could lead to non-desired side effects (e.g. drug induced liver injury). Moving to smaller particles the situation can be reversed; the clearance is too fast, the particles are not retained in tissue and are not able to deliver their therapeutic effect, yet toxicity is usually very low (33). Introducing pre-targeting, using small, but highly boronated NPs, functionalized with a tetrazine moiety, the advantages of small and fast clearing agents can be met, that is, fast clearance from blood and healthy tissue and low toxicity, yet, the retention in tumor tissue is assured by the click reaction to the pre-injected antibody.

1.4 The need for tracking: Nuclear imaging

One of the key aspects in BNCT is the appropriate selection of the time window in which boron irradiation needs to be applied, this is, when after administration of the drug the boron accumulation in the tumor and both the tumor to healthy tissue and the tumor to blood ratios are maximal, in order to maximize therapeutic effect while minimizing off target side effects. Hence, there is a need to determine the pharmacokinetic properties of new chemical entities before their evaluation in therapeutic experiments. This information can be obtained using classical pharmacokinetic studies (e.g. fluid and organ extraction followed by analysis using chromatographic techniques). However, an elegant and non-invasive alternative relies in nuclear imaging techniques.

Nuclear imaging includes single photon emission computerized tomography (SPECT) and positron emission tomography (PET). Both *in vivo* imaging techniques are ultra-sensitive and minimally invasive. After administration of a trace amount of a gamma (SPECT) or positron (PET) emitting labeled compound, the ultimately occurring high energy photons (gamma ray) are detected. The origin of the decay and therefore the location of the radiolabel can be quantitatively calculated. These techniques are often combined with computerized tomography (CT) or newly also with magnetic resonance imaging (MRI) to achieve both, anatomical (CT, MRI) and metabolic (SPECT, PET) information. In this work we focused on PET-CT which has higher spatiotemporal resolution over SPECT.

1.4.1 Positron emission tomography

Positron emission tomography (PET) is an excellent tool to image biochemical processes *in vivo*. In PET, the distribution of a compound labeled with a positron emitter (radiotracer) can be followed and represented in a three-dimensional image. In most cases, the radiotracers accumulate in a certain area of the body and hence, make them visible by photon detectors. PET is most frequently used in cardiology (34), neurological (35) and oncological (36) diseases either for diagnosis and/or therapy progress. However, also in research PET is a very helpful tool (see 1.4.2 PET in drug development).

Positron emitting isotopes decay by a β^+-emission. The nucleus of these nuclides is rich in protons. To stabilize this unbalanced situation a proton (p) turns into a neutron (n) whereas a positron (β^+, antiparticle of the electron, therefore also written as 'e$^+$') and an electron-neutrino (ν) are emitted (Figure 13). The electron-neutrino takes part of the energy and serves

the spin preservation. The positron in contrast takes the other part of the energy and balances the charge. Following, the equations of the β^+ decay are shown: 1) nucleus level, 2) isotopic level.

$$_1^1p^+ \rightarrow {_0^1}n + {_1^0}e^+ + {_0^0}\nu_e + Q \tag{1}$$

$$_Z^A X_N \rightarrow {_{Z-1}^A}Y_{N+1} + {_1^0}e^+ + {_0^0}\nu_e + Q \tag{2}$$
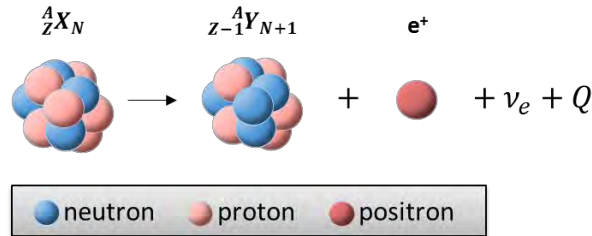
Figure 13: Schematic representation of the radioactive decay by positron emission.

During this procedure the nuclide (X) transforms into another element (Y), the daughter product. Q describes the energy of the decay and the difference of the mass of the transformation (E = mc^2).

The emitted positron (β^+), which has a specific kinetic energy related to the nuclide (although positrons are not emitted with a single energy but following an energy distribution, which is characteristic for each positron emitter), will interact with an electron of the environment after losing energy to a certain point and a short-lived positronium will arise (37). The positronium in turn decays by annihilation, a procedure in which two gamma quanta (photons) with the energy of 511 keV are transmitted to the opposite side of each other (180°). These photons are detected by PET scanners. The detection of two photons simultaneously by two opposite detectors (coincidence detection) defines a line of response (LOR). The detection of hundreds of thousands of coincidences enables the reconstruction of a three-dimensional image which contains quantitative information of the regional distribution of the radiotracer. A drawback in PET is the fact that the emission of the positron is not in the exact same place as the emission of the two photons. This difference coincides with the distance that the positron travels before annihilating (positron range; typically a few millimeters), and depends on the energy of the emitted positron. Ultimately, this fact results in a decreased spatial resolution. However, new devices are able to statistically correct for this to a certain extent, and the resolution of modern PET scanners (especially preclinical ones) is close or below the positron range (Figure 14) (38).
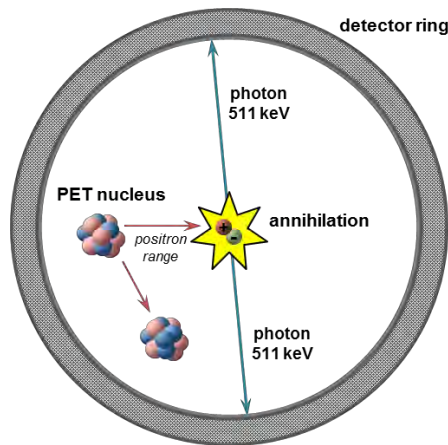
Figure 14: Scheme of PET principle. A positron is emitted and after travelling a certain distance (positron range) it annihilates with an electron, resulting in the formation of 2 photons (511 keV each) which are emitted in opposite directions and detected by special detectors as coincidence events.

A competitive way for proton rich nuclei to stabilize is to decay via electron capture (EC). A proton in the nucleus absorbs an electron from the close K- or L- electron shell. The proton converts into a neutron with the emission of an electron-neutrino (Figure 15). The generated daughter nuclide is in an excited state and therefore releases excitement via x-ray or Auger electrons (filling of the inner-shell vacancy by an electron of a higher-energy shell of the same atom, the thereby released energy emits another electron and a chain reaction can arise). Following, the equations of the EC are shown: 3) nucleus level, 4) isotopic level.

$$\begin{array}{cc} {}_1^1p^+ + {}_1^0e^- \rightarrow {}_0^1n + {}_0^0\nu_e + Q & (3) \end{array}$$

$$\begin{array}{cc} {}_Z^A X_N + {}_1^0e^- \rightarrow {}_{Z-1}^A Y_{N+1} + {}_0^0\nu_e + Q & (4) \end{array}$$
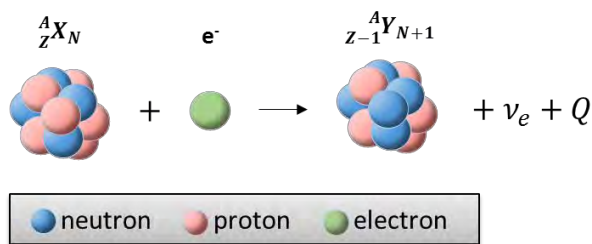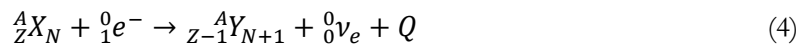
Figure 15: Schematic representation of the radioactive decay by electron capture.

Other than in the β^+ decay where the freed energy is split between the β^+-particle and the neutrino which leads to a continuous energy spectrum, here the entire energy is carried by the neutrino and gives a single sharp energy profile. However, as no positron is emitted this decay is not useful for PET and radionuclides need to be selected carefully with a high percentage of β^+ decay, as other radiation types do not contribute to image quality but increase the radiation dose to the investigated subject.

1.4.2 PET in drug development
Besides the use of PET in clinics for diagnostic and to follow the progress of a disease and its therapy, it is increasingly used in drug development. PET is a useful tool to evaluate

pharmacokinetic properties (like biodistribution and metabolism) but also in proof of target (does the drug aim for the predicted target?), proof of mechanism (is a downstream component affected?) and proof of efficacy (to predict the outcome before clinical studies) of a new drug (39).

Irrespective of the application, it has to be considered that a radionuclide (positron emitter) needs to be inserted into the new drug. Ideally the radioisotope 'simply' exchanges an existing stable atom, e.g. ^{11}C for ^{12}C, or ^{13}N for ^{14}N. Yet, for more complex compounds such as proteins, antibodies or NPs, this way of radiolabeling is not possible. Hence, the radionuclide is additionally attached and therefore the structure of the compound changed. In these cases, it becomes necessary to evaluate if behavior and properties remain unaffected. Furthermore, it is obligatory to keep in mind that the PET image represents the distribution of the radionuclide, not to the actual drug. That is, if the radiolabeling is not stable, or if the drug decomposes *in vivo*, the visible PET image is due to the fragment which contains the radionuclide and misinterpretation of the obtained image is possible. Because of this, evaluation of the stability of the label and determination of metabolism is paramount for proper image interpretation.

In the particular case of pre-targeting for therapeutic applications as proposed in this PhD thesis, PET is very helpful as it enables: (i) the determination of the ideal time window when the second component has to be administered. This is, the time point at which the concentration of the mAb in the tumor is maximum, which can be determined by radiolabeling the mAb and performing PET studies at different time points after administration; and (ii) the time at which neutron irradiation should be performed, that is, the time window at which the accumulation of the second component in the tumor is maximum. This can be determined by radiolabeling the second component (in our case, the NP), and performing PET studies at different time points after administration (Figure 16). The radiolabeling strategy and the radionuclide to be used depend on different factors, as discussed below (see 1.4.3 PET nuclides).
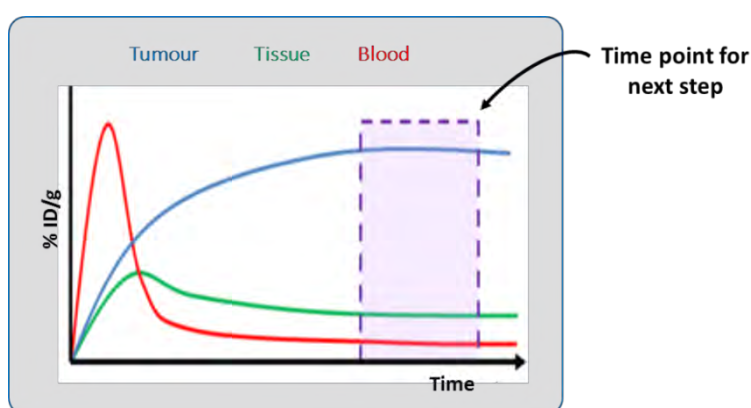

Figure 16: Timing in pre-targeting. PET imaging can provide information about the concentration of the labeled species over time, thus enabling appropriate selection of the time window to proceed to the following step: administration of the second component or neutron irradiation.

1.4.3 PET nuclides

To acquire good-quality PET images, no matter if in clinic or in research, the choice of the radionuclide is critical. The most important PET nuclides are summarized in Table 2.

Table 2: The most important PET radionuclides and their properties.

Nuclide	Half-life	Transformation (Frequency %)	Max. β^+- energy [MeV]	Max. β^+-range in H_2O [mm]	Method of production
^{11}C	20.40 min	β^+ (99.8) EC (0.2)	0.96	3.8	^{10}B(d,n)^{11}C ^{14}N(p,α)^{11}C
^{13}N	9.96 min	β^+ (100.0)	1.19	5.0	^{12}C(d,n)^{13}N ^{16}O(p,α)^{13}N
^{15}O	2.03 min	β^+ (99.9) EC (0.1)	1.73	7.6	^{14}N(d,n)^{15}O ^{15}N(p,n)^{15}O
^{18}F	109.65 min	β^+ (96.9) EC (3.1)	0.63	2.2	^{18}O(p,n)^{18}F
^{64}Cu	12.70 h	β^+ (17.8) β^- (38.4) EC (43.8)	0.65	2.5	^{64}Ni(p,n)^{64}Cu ^{64}Ni(d,2n)^{64}Cu
^{68}Ga	67.71 min	β^+ (89.1) EC (10.9)	1.90	13.6	^{68}Ge/^{68}Ga-Generator
^{89}Zr	78.41 h	β^+ (22.3) EC (76.6)	0.90	3.8	^{89}Y(p,n)^{89}Zr

The selection of the nuclide depends on many different factors. The main required property for a PET nuclide is obviously the β^+-decay, in best cases with a high percentage. But, also the energy of the positron is relevant. It should be low to have a short positron range (see 1.4.1 Positron emission tomography) which will improve the resolution of the image.

Another important characteristic is the half-life. It is to be taken into account that the radiotracer needs to be synthesized and purified, then passes a quality-control and sometimes needs to be delivered to another institution. Furthermore, the half-life needs to suit the biological half-life of the molecule under investigation so that the subject is not affected by a high radiation dose but the radiotracer is still detectable during its whole process.

Besides, the chemical properties of the nuclide will dictate the way of radiolabeling, either by covalent binding of non-metal nuclides or through the use of a chelator which will generate a stable complex with a metal nuclide.

Finally, the availability of the nuclide places a role in the selection. Some are synthesized by nuclide generators (e.g. ^{68}Ga which is produced in commercially available ^{68}Ge/^{68}Ga generators) which are usually very easy to handle for daily hospital work. Many others are generated in a cyclotron (e.g. ^{18}F, ^{11}C, ^{89}Zr, ^{64}Cu). This equipment is much more complex and more expensive in maintenance. Thus, just some institutions are able to afford it. Finally, nuclides can be synthesized within a nuclear reactor which needs again more personal care, more safety and more financial afford (e.g. the SPECT nuclide ^{131}I).

As described above there are many factors to be considered when choosing a radionuclide. In this study very different components with different requirements concerning the nuclide had to be labeled. In the following section, a brief introduction to the PET radionuclides used in the context of this PhD thesis is included.

Nuclide for antibodies - ^{89}Zr

^{89}Zr properties at a glance

$t_{1/2}$ = 3.3 d = 78.4 h = 4704.6 min

EC: 76.6 %

β^+: 22.3 %
$E_{ave}(\beta^+)$ = 397 keV
$E_{max}(\beta^+)$ = 897 keV

$E(\gamma)$ = 909 keV

The biodistribution of monoclonal antibodies is very slow. Therefore, a nuclide needs to be selected which is able to follow its nature, thus a nuclide with a long enough half-life. At present the most common nuclide in immuno-PET is Zirconium-89 (^{89}Zr). Its half-life is 3.27 days (78.41 h) and is therefore ideal to monitor the pharmacokinetic of mAbs in tumors.

The most common way to produce ^{89}Zr is the bombardment of an natural yttrium foil with protons in a cyclotron *via* the nuclear reaction of ^{89}Y(p,n)^{89}Zr (40). After irradiation the metal foil is dissolved in acid (6 M HCl), then purified by a hydroxamate column (e.g. functionalized Waters Sep-Pak® Plus Accell CM cation exchanged resin), which can selectively trap ^{89}Zr and be finally eluted with oxalic acid (41).

The decay of ^{89}Zr to stable Yttrium-89 (^{89}Y) occurs to 76.6 % by electron capture (EC) and 22.3 % by positron emission (β^+-decay), which makes it suitable for PET. However, before stable ^{89}Y forms, a metastate of ^{89m}Y is generated which de-excites in only 16 seconds to its stable nuclide, with emission of a gamma ray with an energy of 909 keV. A scheme of the decay is shown in Figure 17.
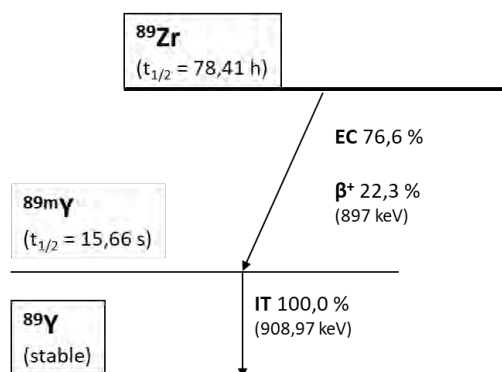

Figure 17: Decay scheme for ^{89}Zr (max energy shown).

Finally, the chemical route for radiolabeling the mAb needs to be considered. As ^{89}Zr is a metal, a covalently bound chelator is used to build a stable complex in physiological

conditions with the nuclide. To date desferrioxamine (DFO) - chelators are the state of the art. The labeling conditions are very mild which allows to label mAbs without denaturizing them. The *p*-isothiocyanatobenzyl-DFO (*p*-SCN-Bz-DFO) can be covalently bound to amine groups of lysine residues present in the amino acid sequence forming a thiourea bond (Figure 18). Recently, Vugts *et al.* are investigating more stable chelator-radionuclide complexes like the tetrahydroxamate chelator called DFO* (DFO star) (42).
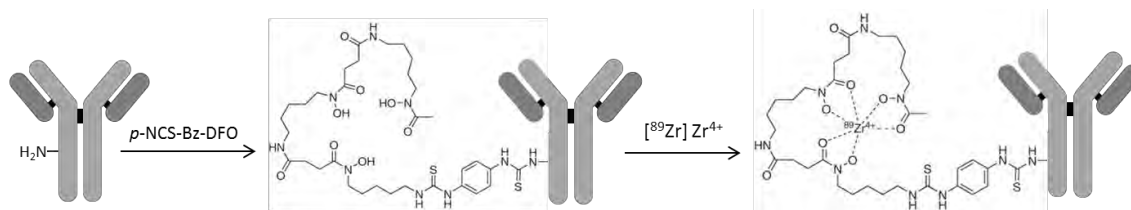

Figure 18: Schematic representation of mAb conjugation with *p*-SCN-Bz-DFO and labeling with ^{89}Zr

Nuclide for AuNP- ^{64}Cu

^{64}Cu properties at a glance

$t_{1/2}$ = 12.7 h = 762.0 min

EC: 43.8 %

β^- = 38.4 %

β^+ = 17.8 %
$E_{ave}(\beta^+)$ = 278 keV
$E_{max}(\beta^+)$ = 653 keV

$E(\gamma)$ = 1.35 MeV

There are several different methods to radiolabel NPs with a metal-nuclide, e.g. (i) using pre-radiolabeled synthons, which are incorporated into the NPs during production; (ii) direct NP activation where the radioisotope is generated *in situ* using nuclear reactions; and (iii) after-loading, where the isotope is incorporated, attached or entrapped after the synthesis of the NPs (43). Labeling on the surface allows adding the radiolabel as last step after the synthesis and functionalization of the particles, simplifying the handling during those procedures and minimizing radiation dose to the operator. However, the labeling is an additional moiety, which might change the surface properties. Therefore, in this work we focused on the incorporation of the radio metal into the gold core during synthesis, by doping the core with ^{64}Cu (44). Even though the radiolabeling yield is usually lower, the high stability of the label and preventing changes to the properties are significant advantages (43).

Using ^{64}Cu with its half-life of almost 13 hours gives the necessary flexibility for the evaluation of NPs. It is used for both, smaller molecules as well as bigger and slower clearing components. Therefore, it is ideal to monitor smaller AuNPs, which distribute faster than big compounds like antibodies, but slower than small molecules.

The production of ^{64}Cu can be done either with a cyclotron or a nuclear reactor. However, the most common methodology is by the ^{64}Ni(p,n)^{64}Cu (45) nuclear reaction. In this process,

a gold disk, electroplated with enriched nickel-64 is irradiated in the cyclotron with protons. After the bombardment ^{64}Cu is separated from ^{64}Ni by an ion exchange column. The enriched nickel can be recovered and reused which makes the pricey procedure more cost-efficient (46).

The isotope Copper-64 is highly unusual as it decays by three different processes; into ^{64}Ni with 43.8 % electron capture and 17.8 % positron emission, which makes it suitable for PET, and with 38.4 % to ^{64}Zn by beta minus (electron, β$^-$) emission, which makes it also eligible for therapy (Figure 19).
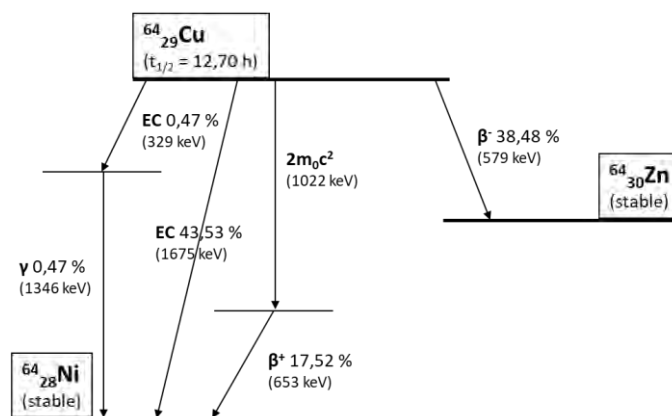
Figure 19: Decay scheme for ^{64}Cu (max energy shown).

Nuclide for B-CDs - ^{18}F

^{18}F properties at a glance

$t_{1/2}$ = 1.8 h = 109.8 min

EC: 3.1 %

β$^+$: 96.9 %

$E_{ave}(β^+)$ = 250 keV
$E_{max}(β^+)$ = 633 keV

$E(γ)$ = 511 keV

Whereas antibodies and AuNPs are rather slow distributed and cleared from the *in vivo* subject by elimination mainly through liver and spleen, B-CDs are eliminated in only minutes through the kidneys. Therefore, a radionuclide with shorter half-life can be chosen. ^{18}F is probably the most used PET-nuclide and with a half-life of close to 2 hours ideal to evaluate the distribution of B-CDs. However, other than ^{89}Zr and ^{64}Cu, ^{18}F is no metal and needs to be coupled to the molecule by covalent bonding. Yet, the possible coupling reactions are limited to the product of the ^{18}F production by cyclotron. Its either produced as [^{18}F]F$^-$ or as [^{18}F]F$_2$ enabling fluorinations by nucleophilic or electrophilic substitution, respectively (47). Furthermore, a late introducing of the radiolabel in the synthesis is favored. Therefore, and to increase possibilities of radiolabeling, so called prosthetic groups are introduced. Those are small organic molecules, radiolabeled in very few steps, containing a functional group which enables easy binding to another component, like e.g. NPs (48; 49).

In this work [^{18}F]F$^-$ was produced by irradiating ^{18}O-enriched water ([^{18}O]H$_2$O) with protons leading to the nuclear reaction of ^{18}O(p,n)^{18}F. A precursor (TfO$^-$Me$_3$NPyTFP$^+$) was fluorinated to obtain the prosthetic group [^{18}F]F-Py-TFP (Figure 20) which could be coupled to amine residues of the B-CDs (50).

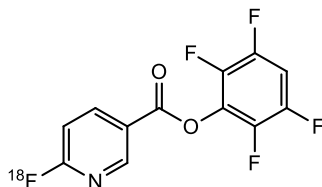**Figure 20:** [^{18}F]F-Py-TFP prosthetic group.

Besides its convenient half-life, a decay into ^{18}O of 97 % by positron emission and only 3 % electron capture makes ^{18}F an almost perfect PET nuclide. Furthermore, the low energy of its positrons leads to high resolution PET images. A scheme of its decay is shown in Figure 21.
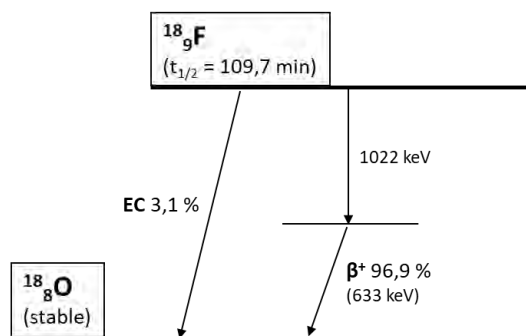

Figure 21: Decay scheme for ^{18}F (max energy shown).

1.5 References

1. International Agency for Research on Cancer. *Global Cancer Observatory.* [Online] 2018. [Cited: December 27, 2019.] http://gco.iarc.fr/today/online-analysis-multi-bars.

2. World Health Organization. *Cancer.* [Online] September 2018. [Cited: December 27, 2019.] https://www.who.int/news-room/fact-scheets/detail/cancer.

3. *Biological effects and therapeutic possibilities of neutrons.* **GL, Locher.** 1936, Am J Roentgenol Radium Ther, Vol. 36, p. 1.

4. *Critical review with an optimistic outlook on Boron Neutron Capture Therapy (BNCT).* **Moss, R.L.** 2014, Appl. Radiat. Isotopes, pp. 1-10.

5. *Boron Neutron Capture Therapy for Cancer.* **Rolf F. Barth, M.D., Albert H . Soloway, Ph.D., Ralph G. Fairchild, Ph.D. and Robert M . Brugger, Ph.D.** 12, December 15, 1992, Cancer, Vol. 70, pp. 2995-3007.

6. *The production of mutations in drosophila with neutron radiation.* **Locher, Mary A. Nagai and Gordon L.** 1937, GENETICS, Vol. 23, pp. 179-189.

7. *A realistic appraisal of boron neutron capture therapy as a cancer treatment modality.* **Rolf F. Barth, Zizhu Zhang and Tong Liu.** 2018, Cancer Communications.

8. *Prospects for the new era of boron neutron capture therapy and subjects for the future.* **Ono, Koji.** 2018, Therapeutic Radiology and Oncology.

9. *Boron Neutron Capture Therapy - A Literature Review.* **Kavitaa Nedunchezhian, Nalini As wath, Manigand an Thiruppathy, Sarumathi Thirugnanamurthy.** 12, 2016, Journal of Clinical and Diagnostic Research, Vol. 10, pp. 1-4.

10. *Boron delivery agents for neutron capture therapy of cancer.* **Rolf F. Barth, Peng Mi and Weilian Yang.** 2018, Cancer Communications.

11. *Carborane Analogues of Cobalticinium Ion.* **Andrew, M. Frederick Hawthorne and Timothy D.** 1965, CHEMICAL COMMUNICATIONS, Vol. 19, pp. 443-444.

12. *Boron agents for neutron capture therapy.* **Kuan Hu, Zhimin Yang, Lingling Zhang, Lin Xie, Lu Wang, Hao Xu, Lee Josephson, Steven H. Liang, Ming-Rong Zhang.** s.l. : Elsevier B.V., 2020, Coordination Chemistry Reviews, Vol. 405.

13. *Boron Containing Macromolecules and Nanovehicles as Delivery Agents for Neutron Capture Therapy.* **Gong Wu, Rolf F. Barth, Weilian Yang, Robert J. Lee, Werner Tjarks, Marina V. Backer and Joseph M. Backer.** s.l. : Bentham Science Publishers Ltd., 2006, Anti-Cancer Agents in Medicinal Chemistry, Vol. 6, pp. 167-184.

14. *The new era of nanotechnology, an alternative to change cancer treatment.* **Jurj, Ancuta.** 2017, Drug Design, Development and Therapy, pp. 2871–2890.

15. *Pretargeting in nuclear imaging and radionuclide therapy: Improving efficacy of theranostics and nanomedicines.* **E. Johanna L. Stéen, Patricia E. Edem, Kamilla Nørregaard, Jesper T. Jørgensen, Vladimir Shalgunov, Andreas Kjaer, Matthias M. Herth.** s.l. : Elsevier Ltd., 2018, Biomaterials, Vol. 179, pp. 209-245.

16. *Boron neutron capture therapy demonstrated in mice bearing EMT6 tumors following selective delivery of boron by rationally designed liposomes.* **Kueffer, Peter J.** 2013, PNAS, pp. 6512–6517.

17. *Application of Cycloaddition Reactions to the Syntheses of Novel Boron Compounds.* **Yinghuai Zhu, Xiao Siwei, John A. Maguire and Narayan S. Hosmane.** 2010, Molecules, Vol. 15, pp. 9437-9449.

18. *Recent biomedical applications of gold nanoparticles: A review.* **Narges Elahia, Mehdi Kamali, Mohammad Hadi Baghersad.** 2018, Talanta.

19. *Mechanisms of Nanoparticle Internalization and Transport Across an Intestinal Epithelial Cell Model: Effect of Size and Surface Charge .* **Azzah M. Bannunah, Driton Vllasaliu, Jennie Lord, and Snjezana Stolnik.** October 19, 2014, Mol. Pharmaceutics , pp. 4363-4373.

20. *Recent trends and methodologies in gold nanoparticle synthesis – A prospective review on drug delivery aspect.* **Manimegalai Sengania, Alexandru Mihai Grumezescub, V. Devi Rajeswaria.** s.l. : Elsevier Inc., 2017, OpenNano, Vol. 2, pp. 37–46.

21. *Controlled Nucleation for the Regulation of the Particle Size in Monodisperse Gold Suspensions.* **Frens, G.** s.l. : Nature Publishing Group, 1973, Nature Physical Science, Vol. 241, pp. 20-22.

22. *Electrophoretic Analysis and Purification of Fluorescent Single-Walled Carbon Nanotube Fragments .* **Xiaoyou Xu, Robert Ray, Yunlong Gu, Harry J. Ploehn, Latha Gearheart, Kyle Raker, and Walter A. Scrivens.** 2004, pp. 12736-12737.

23. *Microwave-assisted synthesis of carbon dots and their applications.* **Tayline V. de Medeiros, John Manioudakis, Farah Noun, Jun-Ray Macairan, Florence Victoriaab and Rafik Naccache**. 2019, J. Mater. Chem. C, pp. 7175-7195.

24. *Surface modification and chemical functionalization of carbon dots: a review.* **Zhou, Fanyong Yan & Yingxia Jiang & Xiaodong Sun & Zhangjun Bai & Yan Zhang & Xuguang.** 2018, Microchimica Acta - Springer, pp. 1-34.

25. *Bioorthogonal Chemistry: Fishing for Selectivity in a Sea of Functionality.* **Bertozzi, Ellen M. Sletten and Carolyn R.** s.l. : Wiley-VCH Verlag GmbH & Co. KGaA, Weinheim, 2009, Angew. Chem. Int. Ed.- Bioorthogonal Chemistry, Vol. 48, pp. 6974 – 6998.

26. *Bioorthogonal chemistry: strategies and recent developments.* **Lin, Carlo P. Ramil and Qing.** s.l. : The Royal Society of Chemistry, 2013, Chem. Commun., Vol. 49, pp. 11007-11022.

27. *The Future of Bioorthogonal Chemistry.* **Devaraj, Neal K.** s.l. : American Chemical Society, 2018, ACS Cent. Sci., Vol. 4, p. 952−959.

28. *Fast and Sensitive Pretargeted Labeling of Cancer Cells through a Tetrazine/trans-Cyclooctene Cycloaddition.* **Neal K. Devaraj, Rabi Upadhyay, Jered B. Haun, Scott A. Hilderbrand, and Ralph Weissleder.** 2009, Angew. Chem., Vol. 48, pp. 7013-7016.

29. *Tetrazine Ligation: Fast Bioconjugation Based on Inverse-Electron-Demand Diels-Alder Reactivity.* **Melissa L. Blackman, Maksim Royzen, and Joseph M. Fox.** 2008, J. AM. CHEM. SOC., pp. 13518–13519.

30. *In Vivo Chemistry for Pretargeted Tumor Imaging in Live Mice.* **Raffaella Rossin, Pascal Renart Verkerk, Sandra M. van den Bosch, Roland C. M. Vulders, Iris Verel, Johan Lub, and Marc**

S. Robillard. s.l. : Wiley-VCH Verlag GmbH & Co. KGaA, 2010, Angew. Chem. Int. Ed.-Bioorganic Chemistry, Vol. 49, pp. 3375 –3378.

31. *Optimization of a Pretargeted Strategy for the PET Imaging of Colorectal Carcinoma via the Modulation of Radioligand Pharmacokinetics.* **Brian M. Zeglis, Christian Brand, Dalya Abdel-Atti, Kathryn E. Carnazza, Brendon E. Cook, Sean Carlin, Thomas Reiner, and Jason S. Lewis.** s.l. : American Chemical Society, 2015, Mol. Pharmaceutics.

32. *Macromolecular Therapeutics.* **Khaled Greish, Jun Fang, Takao Inutsuka, Akinori Nagamitsu, Hiroshi Maeda.** 13, s.l. : Adis Data Information BV, 2003, Clin Pharmacokinet, Vol. 42, pp. 1089-1105.

33. *Renal clearance of quantum dots.* **Hak Soo Choi, Wenhao Liu, Preeti Misra, Eiichi Tanaka, John P Zimmer, Binil Itty Ipe, Moungi G Bawendi & John V Frangioni.** 10, s.l. : Nature Publishing Group, 2007, NATURE BIOTECHNOLOGY, Vol. 25, pp. 1165-1170.

34. *Handbook of nuclear cardiology: Cardiac SPECT and cardiac PET.* **Heller, G. V. and Hendel, R. C.** 2013, pp. 1-221.

35. *Hybrid SPECT/CT Imaging in Neurology.* Andrea Ciarmiello, **Elisabetta Giovannini, Martina Meniconi, Vincenzo Cuccurullo, and Maria Chiara Gaeta**. s.l. : Bentham Science Publishers, 2014, Current Radiopharmaceuticals, Vol. 7, pp. 5-11.

36. *SPECT/CT and tumour imaging.* **Keidar, Gad Abikhzer & Zohar.** s.l. : Springer, 2014, Eur J Nucl Med Mol Imaging, Vol. 41, pp. 67-80.

37. *Chemistry of the Positron and of Positronium.* **Ache, Hans J.** 3, 1972, Angew. Chem. internat. Edit., Vol. 11, pp. 179-199.

38. *The Impact of Positron Range on PET Resolution, Evaluated with Phantoms and PHITS Monte Carlo Simulations for Conventional and Non-conventional Radionuclides.* **L. M. Carter, Adam Leon Kesner, E. C. Pratt, V. A. Sanders, A. V. F. Massicano, C. S. Cutler, S. E. Lapi, Jason S. Lewis.** s.l. : World Molecular Imaging Society, 2019, Molecular Imaginga and Biology.

39. *Radiochemistry: A Useful Tool in the Ophthalmic Drug Discovery.* **Krishna Reddy Pulagam, Vanessa Gómez-Vallejo, Jordi Llop, Luka Rejc.** s.l. : Bentham Science Publishers, 2019, Current Medicinal Chemistry.

40. *Production of $^{88,89}Zr$ by proton induced activation of nat Y and separation by SLX and LLX.* **Binita Dutta, Moumita Maiti, Susanta Lahiri.** s.l. : Akadémiai Kiadó, 2009, J Radioanal Nucl Chem, pp. 663–667.

41. *Standardized methods for the production of high specific-activity zirconium-89.* **Jason P. Holland, Yiauchung Sheh, Jason S. Lewis.** s.l. : Elsevier, 2009, Nuclear Medicine and Biology, Vol. 36, pp. 729-739.

42. *Comparison of the octadentate bifunctional chelator DFO*-pPhe-NCS and the clinically used hexadentate bifunctional chelator DFO-pPhe-NCS for ^{89}Zr-immuno-PET.* **Dongen, Danielle J. Vugts & Chris Klaver & Claudia Sewing & Alex J. Poot & Kevin Adamzek & Seraina Huegli & Cristina Mari & Gerard W. M. Visser & Ibai E. Valverde & Gilles Gasser & Thomas L. Mindt & Guus A. M. S. van.** s.l. : Springer, 2017, Eur J Nucl Med Mol Imaging , Vol. 44, pp. 286–295.

43. **Jordi Llop Roig, Vanessa Gómez-Vallejo, Peter Neil Gibson**, [ed.]. *Isotopes in Nanoparticles: Fundamentals and Applications.* s.l. : Pan Stanford Publishing Pte.Ltd., 2016. 978-981-4669-08-5.

44. *Copper-64-Alloyed Gold Nanoparticles for Cancer Imaging: Improved Radiolabel Stability and Diagnostic Accuracy.* **Yongfeng Zhao, Deborah Sultan, Lisa Detering, Sangho Cho, Guorong Sun, Richard Pierce, Karen L. Wooley, and Yongjian Liu.** s.l. : Wiley-VCH Verlag GmbH & Co. KGaA, Weinheim, 2014, Angew. Chem. Int. Ed., Vol. 53, pp. 156-159.

45. *Efficient Production of High Specific Activity ^{64}Cu Using A Biomedical Cyclotron .* **Deborah W. McCarthy, Ruth E. Shefer, Robert E. Klinkowstein, Laura A. Bass, William H. Margeneau, Cathy S . Cutler, Carolyn J. Anderson and Michael J. Welch.** s.l. : Elsevier Science, 1997, Nuclear Medicine & Biology, Vol. 24, pp. 35-43.

46. *The Copper Radioisotopes: A Systematic Review with Special Interest to ^{64}Cu.* **Artor Niccoli Asabella, Giuseppe Lucio Cascini, Corinna Altini, Domenico Paparella, Antonio Notaristefano, and Giuseppe Rubini.** s.l. : Hindawi Publishing Corporation, 2014, Bio Med Research International, pp. 1-9.

47. *Fluorine-18 Radiochemistry, Labeling Strategies and Synthetic Routes.* **Orit Jacobson, Dale O. Kiesewetter, and Xiaoyuan Chen.** s.l. : American Chemical Society, 2014, Bioconjugate Chem., Vol. 26, pp. 1-18.

48. *Small Prosthetic Groups in ^{18}F-Radiochemistry: Useful Auxiliaries for the Design of ^{18}F-PET Tracers.* **Ralf Schirrmacher, PhD, Björn Wängler, PhD, Justin Bailey, PhD, Vadim Bernard-Gauthier, PhD, Esther Schirrmacher, PhD, and Carmen Wängler, PhD.** s.l. : Elsevier Inc. , 2017, Semin Nucl Med.

49. *Fluorine-18 labelled building blocks for PET tracer synthesis.* **Dion van der Born, Anna Pees, Alex J. Poot, Romano V. A. Orru, Albert D. Windhorst and Danielle J. Vugts**. s.l. : The Royal Society of Chemistry, 2017, Chem.Soc.Rev., Vol. 46, p. 4709.

50. *One Step Radio synthesis of 6-[^{18}F]Fluoronicotinic Acid 2,3,5,6-Tetrafluorophenyl Ester ([^{18}F]F-Py-TFP): A New Prosthetic Group for Efficient Labeling of Biomolecules with Fluorine-18.* D**ag E. Olberg, Joseph M. Arukwe, David Grace, Ole K. Hjelstuen, Magne Solbakken, Grete M. Kindberg, and Alan Cuthbertson.** s.l. : American Chemical Society, 2010, J. Med. Chem., Vol. 53, pp. 1732-1740.

Chapter 2: Motivation and objectives

2.1 Justification of the study: the PET3D project

Drug development usually takes a lot of time, money and resources, such as chemicals, biologicals and *in vivo* subjects. Positron emission tomography (PET) can be used to minimize the use of experimental animals, and accelerate the whole process by identifying poor candidates at early stages in the process, thus saving time and money while increasing the effectiveness to design and develop drugs.

The PET3D project (**PET** imaging in **D**rug **D**esign and **D**evelopment) originated out of this statement. It is a MSCA-ITN (Marie Skłodowska-Curie Actions Innovative Training Network), funded by the European Commission under the H2020 – MSCA-ITN-2015 program (grant agreement No. 675417) for a duration of 4 years (June 2016 – May 2020) (1). The aim of the project was to train 15 early stage researchers (ESR), located at 8 different institutions in Europe, to become experts in PET imaging and drug development. The institutions involved were the University of Aberdeen (with Professor Matteo Zanda as project coordinator, later in Loughborough University), the VUmc Amsterdam (now UMC), the Vrije Universiteit Brussel, the University of Bergen, CIC biomaGUNE in Donostia-San Sebastián (host of this PhD), the European Institute for Molecular Imaging in Münster and two industrial partners, Imanova (now Invicro; UK) in London and AstraZeneca in Mölndal (Sweden). Covering the main diagnostic/therapeutic areas in which PET is used (oncology, cardiovascular and central nervous system) PET3D was coordinated in five research work packages (WP) (Figure 1).
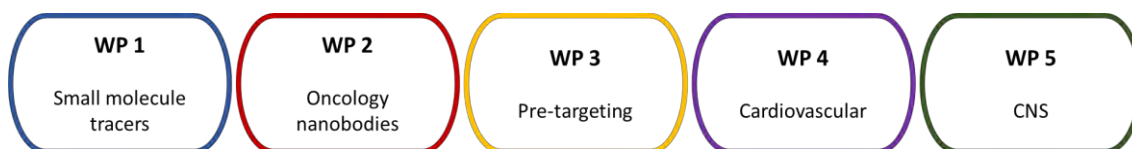

Figure 1: Research work packages of the European project PET3D: WP1: 'Nanoparticles and Small Molecule Tracers in Oncology PET Imaging'; WP 2: 'Biologicals as Tracers in Oncology PET Imaging'; WP 3: 'Pre-targeted Labeling of Biomolecules in Oncology PET Imaging'; WP 4: 'Cardiovascular PET Imaging'; WP 5: 'CNS PET Imaging'.

The advantages of using PET in drug development have already been discussed in chapter one (1.4.2 PET in drug development). Besides the evaluation of pharmacokinetic properties, questions like '*What and where is the disease?', 'Is the disease accurately targeted by the therapy?'* and '*Is the treatment effective?'* can be answered before going into the third clinical phase, not only preventing a late failure of the drug in the process of evaluation, but also achieving an immense improvement in time and cost (2).

The PhD in hand, titled "A pre-targeting approach to boron neutron capture therapy: towards multipurpose Boron-Enriched Therapeutic Agents" was carried out in the frame of WP3, 'Pre-targeted Labeling of Biomolecules in Oncology PET Imaging'. It builds on the existing knowledge (including chemistry, radiochemistry, nanotechnology and *in vitro* and *in vivo* analysis) in the radiochemistry and molecular imaging group at CIC biomaGUNE under the supervision of Dr. Jordi Llop. His expertise in boron chemistry, radiochemistry, nanotechnology and molecular imaging is proven by publications (3; 4; 5; 6; 7), previous and

current research projects, and invited national and international lectures. The core of the experimental work was executed at the host institution CIC biomaGUNE in Donostia-San Sebastián, Spain. Additionally, secondments were carried out taking advantage of the expertise existing in other institutions of PET3D. The expertise in antibodies (conjugation and radiolabeling) available in the radiology and nuclear medicine group with Dr. Daniëlle Vugts at the VUmc (now UMC) in Amsterdam, Netherlands, and the expertise in medicinal chemistry (bioorthogonal click chemistry) at the Institute of Medical Sciences at the University of Aberdeen, Scotland, in the group of Prof. Matteo Zanda.

Cancer, still being the second leading cause of death worldwide (8), brings great need in the design and development of new drugs. This PhD focuses on the promising cancer therapy of BNCT (see Chapter 1). Even though there are already successful clinical trials being conducted, the lack of a boron delivery agent able to deliver a sufficient amount of ^{10}B into tumor tissue combined with high selectivity has limited the use of BNCT and impeded the move to become a more standardized therapy. To reach the aim of this PhD, the development of novel BNCT agents on multi-functionalized NPs, able to selectively accumulate boron atoms in tumor tissue using a pre-targeting strategy, the following objectives were appointed.

2.2 Objectives
The specific objectives of this PhD thesis were:

1. To select and radiolabel a cancer cell targeting monoclonal antibody (mAb) suitable for pre-targeting; to optimize the trans-cyclooctene (TCO) functionalization of the selected candidate to enable the *in vivo* click reaction.
2. To analyze the randomly conjugated antibody, comparing mass analysis with direct methods, to predict the efficiency for pre-targeting.
3. To investigate the pharmacokinetic properties of the functionalized antibody in a subcutaneous tumor mouse model using PET-CT.
4. To investigate the internalization of the antibody *in vitro* and *in vivo*.
5. To design, synthesize, characterize and radiolabel multifunctionalized nanoparticles (gold NPs and boron-carbon dots), heavily loaded with boron to ensure a sufficient delivery to tumor tissue, and functionalized with tetrazine to enable the *in vivo* click reaction with the TCO functionalized antibody.
6. To evaluate the pre-targeting strategy *in vivo* in subcutaneous tumor mouse models using PET-CT.

2.3 References

1. **Comission, European.** CORDIS. *PET Imaging in Drug Design and Development.* [Online] Managed by the EU Publications Office, July 08, 2019. [Cited: January 21, 2020.] https://cordis.europa.eu/project/id/675417.

2. **PET3D.** PET3D. [Online] 2017 PET3D Privacy Policy. [Cited: January 22, 2020.] https://www.pet3d.eu/.

3. *C-C Plasticity in Boron Chemistry: Modulation of the Cc-Cc Distance in Mixed Pyrrolyl/Dicarbollide Complexes.* **Jordi Llop, Clara Vinas, Francesc Teixidor, Lluis Victori, Raikko Kivekäs and Reijo Sillanpää.** s.l. : American Chemical Society, 2001, Organometallics, Vol. 20, pp. 4024-4030.

4. *Tracing nanoparticlesin vivo: a new general synthesis of positron emitting metal oxide nanoparticles by proton beam activation.* **Carlos Perez-Campana, Vanessa Gomez-Vallejo, Abraham Martin, Eneko San Sebastian, Sergio E. Moya, Torsten Reese, Ronald F. Ziolo and Jordi Llop.** s.l. : The Royal Society of Chemistry, 2012, Analyst, Vol. 137, pp. 4902–4906.

5. **Jordi Llop, Vanessa Gomez-Vallejo, Peter Neil Gibson, [ed.].** *Isotopes in Nanoparticles: Fundamentals and Applications.* s.l. : Stanford Publishing, 2016. 978-9814669085.

6. *[^{18}F]Fluorination of o-carborane via nucleophilic substitution: towards a versatile platform for the preparation of ^{18}F-labelled BNCT drug candidates.* **Kiran B. Gona, Vanessa Gomez-Vallejo, Daniel Padro and Jordi Llop.** s.l. : The Royal Society of Chemistry, 2013, Chem.Commun, Vol. 49, pp. 11491-11493.

7. *Gold Nanoparticles as Boron Carriers for Boron Neutron Capture Therapy: Synthesis, Radiolabelling and In Vivo Evaluation.* **Krishna R. Pulagam, Kiran B. Gona, Vanessa Gómez-Vallejo, Jan Meijer, Carolin Zilberfain, Irina Estrela-Lopis, Zuriñe Baz, Unai Cossío and Jordi Llop.** 19, 2019, Molecules , Vol. 24, p. 3609.

8. World Health Organization. *Cancer.* [Online] September 2018. [Cited: December 27, 2019.] https://www.who.int/news-room/fact-scheets/detail/cancer.

Chapter 3: Conjugation and analysis of monoclonal antibodies

3.1 Introduction

Over the last decades monoclonal antibodies (mAbs) have experienced a huge increase in interest as scientific tool as well as human therapeutics. Their unrivaled property is a very high specificity towards their target (antigen) with high affinity and avidity. This property is due to the antigen binding site of the mAbs (Figure 1).
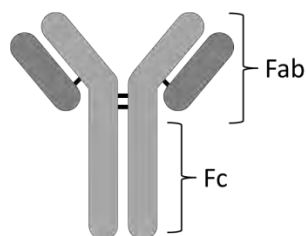

Figure 1: Schematic structure of an immunoglobulin type mAb (IgG), consisting out of two heavy chains (light grey) and two light chains (dark grey), as well as the antigen binding fragment (Fab) and the constant fragment (Fc). The black connections visualize disulfide bonds.

Monoclonal antibodies can be functionalized with a wide variety of molecules to introduce different properties. For example, by generating antibody-drug conjugates to act as drug carriers in which the targeting properties of the mAb are combined with the therapeutic abilities of the drug (1; 2); additionally, they can be functionalized with imaging capabilities by attaching radionuclides or fluorescent dies, enabling subsequent *in vivo* tracking using nuclear imaging techniques such as Positron Emission Tomography (PET) or Single Photon Emission Computed Tomography (SPECT) (3), or enabling their tracking both at microscopic and macroscopic levels using different optical microscope modalities or tomographic techniques, respectively (4; 5). Finally, they also can be functionalized with molecules capable to undergo bioorthogonal reactions *in vivo*, to be applicable in pre-targeting strategies (6; 7; 8).

When tackling the modification of mAbs, several aspects are to be considered. Most important, the conditions need to be mild to prevent denaturation and degradation of the protein and therefore loss of its biological function. Then, the newly formed bond must be stable under physiological conditions and finally it must not significantly compromise the specificity of the antibody-antigen binding site. To overcome issues related to the latter, over the last years many groups have investigated site-specific conjugation (3; 9; 10; 11), which consists of conjugating the functionality to a selective functional group of the mAb, usually present on both heavy chains. Common methods are functionalizing the glycans or reducing the sulfide bonds and using the resulting reactive groups to couple the ligand (Figure 2). Advantages of the site-selective conjugation are a defined number of ligands per antibody, homogeneity and a higher chance to keep the antigen binding site unchanged.
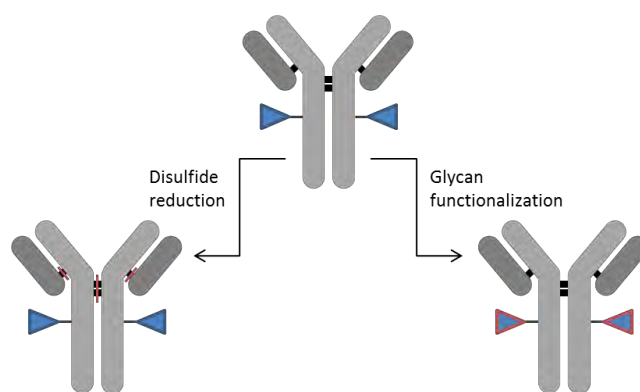
Figure 2: Schematic presentation of site-specific conjugation by reducing disulfide bonds (black) or functionalizing glycans (blue).

However, more frequently used is the random conjugation (6; 12; 13; 14), where the ligand is attached to the accessible primary amines group of lysine residues via *N*-hydroxysuccinimide ester (NHS-ester) or isothiocyanates, or to the thiol group of cysteine residues via maleimides through thio-Michael addition reactions (Figure 3). Disadvantages of those methods are the lack of site-specificity and stoichiometric control, the production of a high heterogeneity of conjugates and the risk of modifications to the antibody-antigen binding site (15). Despite these aspects, the mild reaction conditions together with the straightforward and rather easy procedure to functionalize mAbs are advantage enough to be the preferred method.
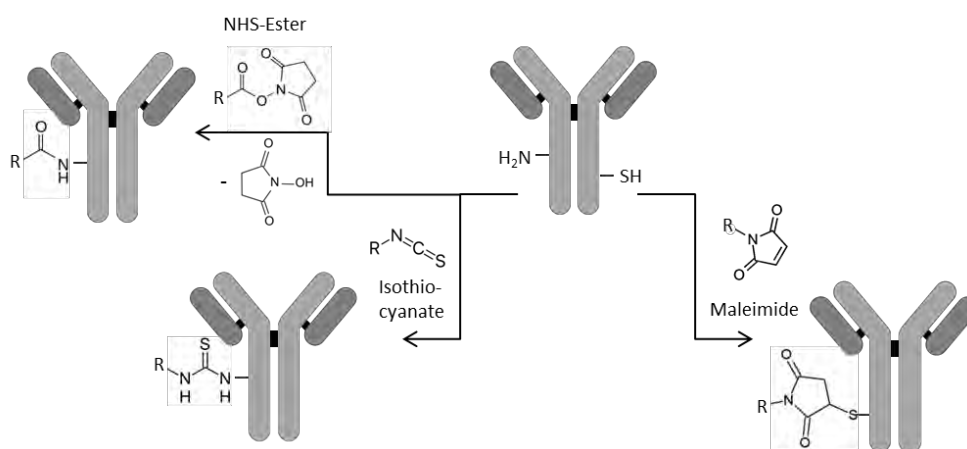
Figure 3: Schematic presentation of random conjugation by using primary amine groups of lysine side chains or thiol groups of cysteine side chains.

For this PhD project two different antibody modifications were performed, using random conjugation to lysine residues: (i) the conjugation with a metal chelator, a desferrioxamine derivative (*p*-NCS-Bz-DFO), to enable radiolabeling with the PET radionuclide Zirconium-89 (^{89}Zr); and (ii) the functionalization with *trans*-cyclooctene (TCO-NHS) to allow the bioorthogonal click reaction with a tetrazine functionalized component required for the pre-targeting strategy. Each mixture of conjugates (Figure 4) was analyzed using a variety of analytical methods, including a direct titration method (photometric for TCO, radiometric for DFO) and mass analysis, including MALDI/TOF MS (Matrix-Assisted Laser Desorption-Ionization / Time Of Flight Mass Spectrometry) and UPLC/ESI-TOF MS

(Ultra High Performance Liquid Chromatography / Electrospray ionization - Time Of Flight Mass Spectrometry). The approach, using different analytical methods, was initiated to enable comparison between the direct method, which gives an average number only of available moieties, and the mass analysis, which gives an average number of all bound moieties per mAb and, with the help of mathematical fittings, the distribution of the different conjugates present in the heterogenic mixture.
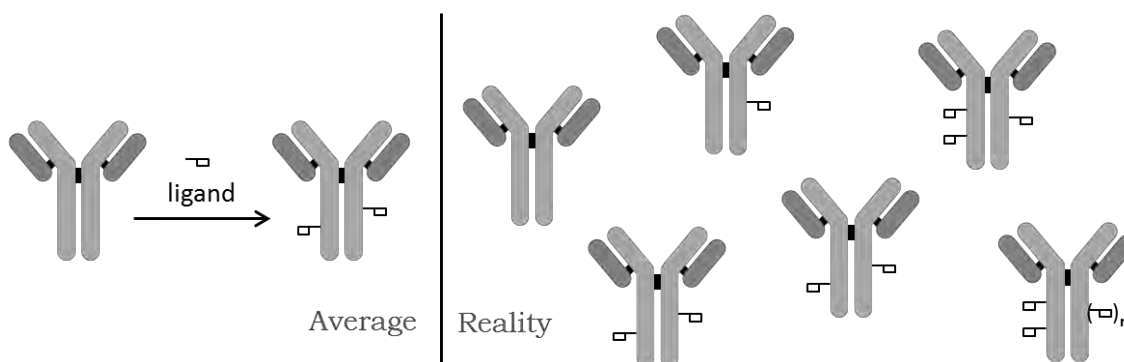

Figure 4: Schematic presentation of the obtained heterogenic conjugates after random conjugation to lysine residues. Although the average ratio of ligand per mAb is usually determined, closer insight in the reality of the obtained heterogenic mixture is more challenging.

Conjugation and analysis have been performed on two different antibodies, both FDA and EMA approved. Bevacizumab (sold under the trade name Avastin®) is a humanized mAb that targets VEGF-A (vascular endothelial growth factor) and hence inhibits the growth of blood vessels (16). Due to the presence of angiogenesis in most cancer types, VEGF-A is generally overexpressed in tumors. Trastuzumab (sold under the trade name Herceptin®), also humanized, targets HER2, an extracellular domain of the epidermal growth factor receptor (EGFR) (16). The pathway of HER2 leads to cell division and growth. By Trastuzumab binding to HER2, an immune-mediated response is induced, which causes internalization and down-regulation of HER2, hence suppressing cell growth. Herceptin is used to treat gastric tumors as well as breast cancer in which HER2 is overexpressed.

3.2 Objectives
The specific objectives of this work were:

1. To conjugate the two antibodies, Bevacizumab and Trastuzumab, in different molar ratios with the ligands TCO-NHS or *p*-NCS-Bz-DFO.
2. To analyze the obtained conjugates with direct titration methods; photometric for TCO, radiometric for DFO.
3. To analyze the obtained conjugates with mass analysis: MALDI/TOF MS and UPLC/ESI-TOF MS, and compare the results to those obtained in Objective 2.

3.3 Results and discussion

3.3.1 TCO conjugation – direct method
TCO is usually attached to mAbs to enable pre-targeting strategies. For an efficient *in vivo* click reaction to occur, the TCO not only needs to be attached to the mAb, but also available for the complement bioorthogonal reagent injected in second place. Hence, during

characterization it is important to determine not only the average ratio of TCO-moieties per antibody after random conjugation, but also those that are available for reaction, as a small moiety like TCO (152 Da; compared to the antibody: 150 kDa) could be masked by hydrophobic interactions with the mAb (17).

First, we tackled the determination of available TCO-groups, information that can be obtained using titration methods. Therefore, we used a tetrazine-fluorophore compound (6-methyl-tetrazine-sulfo-Cy3 = mTzCy3), which undergoes a fast click reaction with the TCO moiety, to establish a direct photometric method. In brief, the antibody was conjugated with different molar-equivalents of TCO-NHS (60 min at room temperature), purified via spin filtration, and mTzCy3 added to induce the click reaction (Figure 5). After incubation (5 min at room temperature) the functionalized mAb was purified again, the UV-VIS-spectra measured and the concentration of both, mAb and fluorophore, determined.
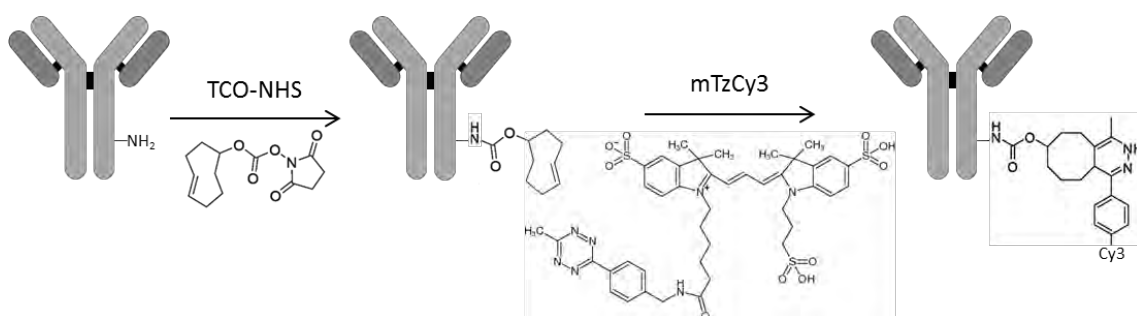

Figure 5: TCO conjugation followed by mTzCy3 coupling to determine the average ratio of TCO/mAb via titration, a direct photometric method.

UV-VIS-spectrophotometric measurements were carried out with a NanoDrop® Spectrophotometer. It uses the Lambeert-Beer's Law ($A = \varepsilon * l * c$; A = absorbance, ε = extinction coefficient, l = path length, c = concentration) to calculate the concentration from the absorbance. The following extinction coefficients have been used: ε(mAb) = $210 \frac{L}{mmol*cm}$ (NanoDrop® default for immunoglobulin type mAbs) and ε(mTzCy3) = $151 \frac{L}{mmol*cm}$ (taken from datasheet of Jena Bioscience). The advantages of NanoDrop® are the fast analysis and the small amount of sample necessary per measurement.

However, to ensure plausibility of the method and investigate possible interferences during the assays (which could alter the determination of concentration needed to calculate the ratio of available TCO per mAb), a preliminary evaluation was performed by measuring the absorbance of different compounds (containing functional groups which are involved in the protocol) at different concentrations in an individual fashion (Figure 6) and after the click reaction (Figure 7).
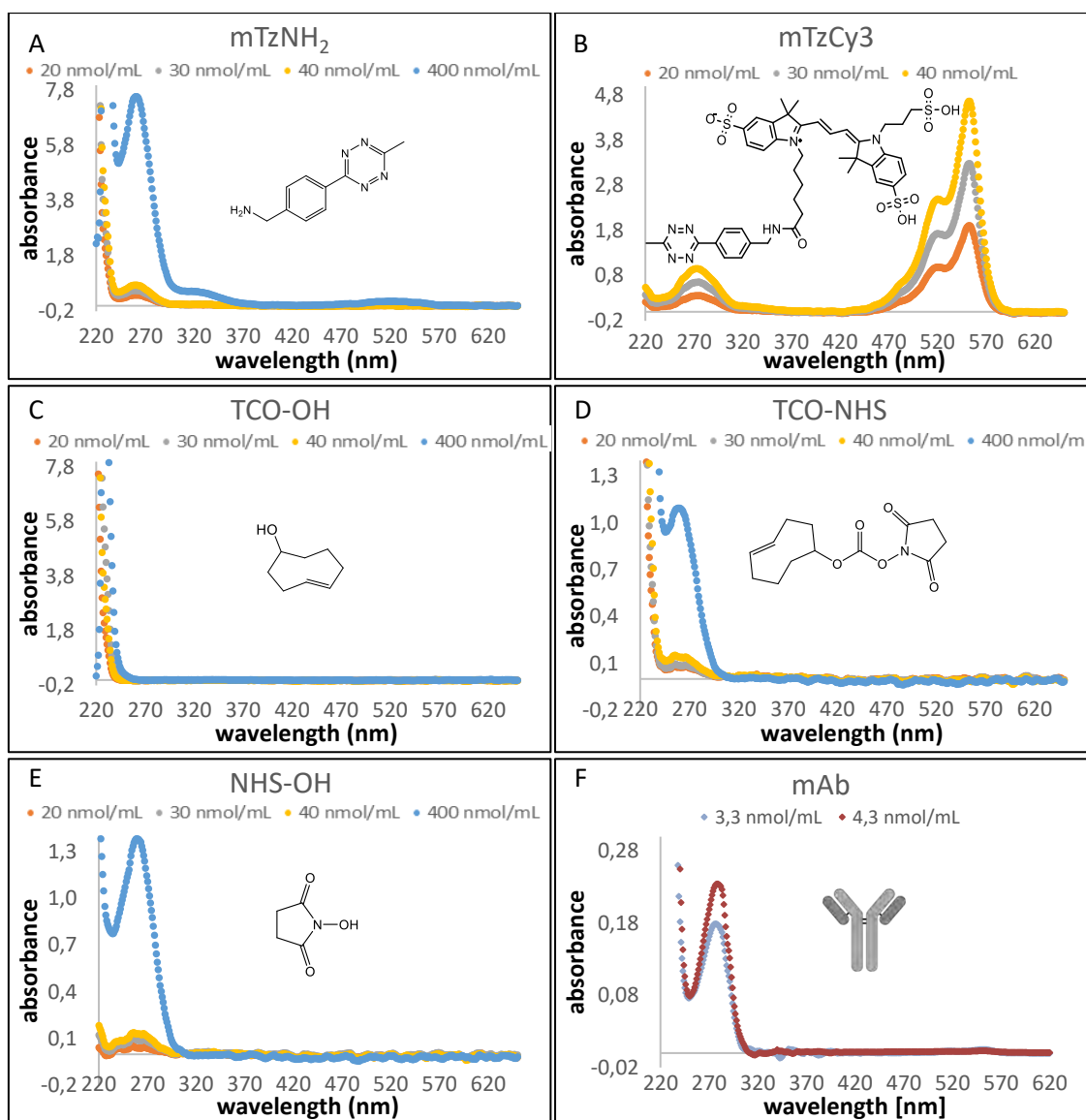
Figure 6: UV-VIS spectra of A) mTzNH$_2$, B) mTzCy3, C) TCO-OH, D) TCO-NHS, E) NHS-OH, F) mAb.

The spectra show that TCO itself has no light absorbance. However, both tetrazine (A) and NHS (E) spectra show their maximum absorbance at around 260 nm which can also be found in the TCO-NHS (D) spectrum (Figure 6). Taking into account that the maximum absorbance of the mAb is at 280 nm (F) interference could apply. However, during the procedure tetrazine moieties would be clicked to TCO moieties resulting in a different chemical structure, which may lead to a different absorbance profile. The NHS moiety on the other hand is cleaved off during the conjugation of the mAb with TCO-NHS and isn't present anymore after purification. Hence, measurements of clicked compounds in different ratios to each other were performed (Figure 7).

Figure 7: UV-VIS spectra after click reaction in different ratios to each other of A) mTzNH2 + TCO-OH, B) mTzNH2 + TCO-NHS, C) mTzCy3 + TCO-OH, D) mTzCy3 + TCO-NHS.

Looking at the spectrum after the click reaction between mTzNH$_2$ and TCO-OH (A) the signal at 260 nm disappears, whereas after the addition of TCO-NHS the signal can still be observed due to th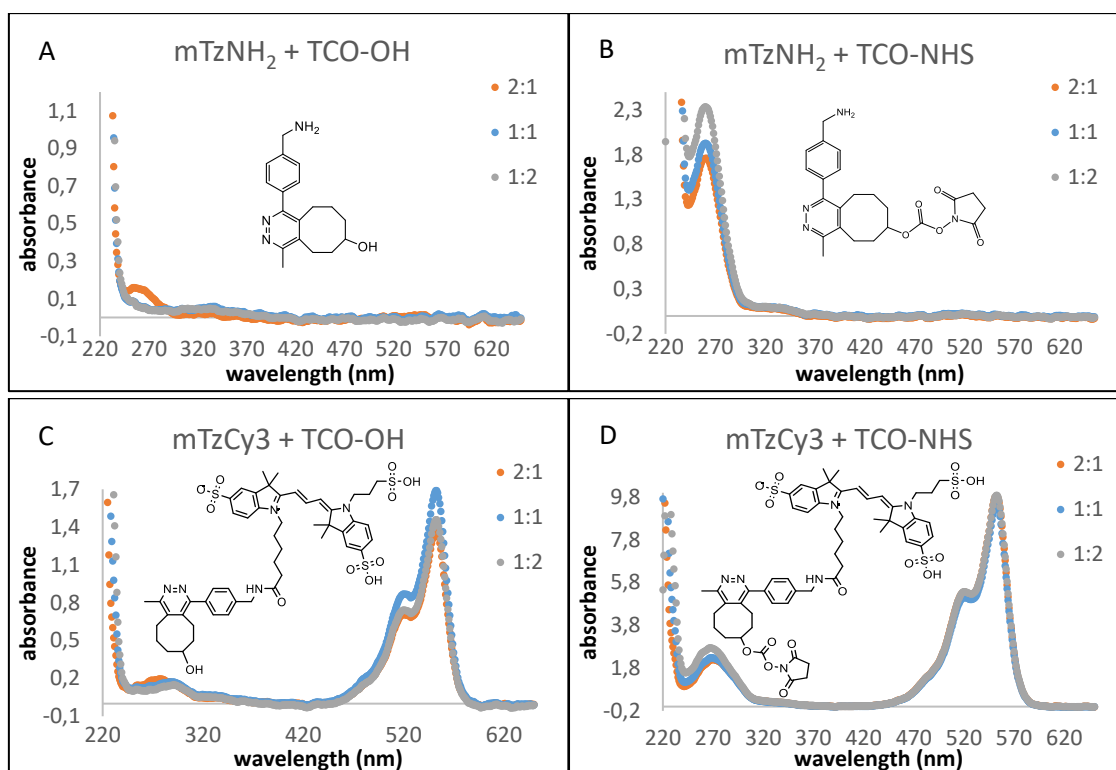e NHS moiety (B). The same behavior can be witnessed using mTzCy3 instead of mTzNH$_2$ (C, D). Hence, the chemical change of tetrazine during the click reaction resolves the possible interference with the mAb signal.

To further evaluate the method a titration with mTzCy3 was carried out to assure a quantitative binding of mTzCy3 to all available TCO moieties. Therefore, Bevacizumab was reacted with 30 eq. TCO-NHS for 90 min at RT, purified, split into 6 fractions and 3 each incubated with either 1/6th or 1/3rd moles mTzCy3 of the initial amount of TCO-NHS (divided by 6 for the 6 fractions). In this case, using initially 30 eq. of TCO-NHS per mAb it would be 5 and 10 eq. mTzCy3 per mAb. The determined ratios of conjugated TCO per mAb were with 1.12 ± 0.03 for 1/6th and 1.13 ± 0.09 for 1/3rd not significant different and it was concluded that the reaction was already quantitative with 1/6th moles mTzCy3 of the initiated amount of TCO-NHS (Table 1).

Table 1: Results of study to ensure quantitative reaction between Bevacizumab-TCO (30 eq. TCO-NHS) and mTzCy3 with 1/6th and 1/3rd moles mTzCy3 per initiated TCO-NHS after 60 min incubation at room temperature (values are expressed as mean $\pm$ standard deviation, n = 3).

mTzCy3/ TCO-NHS	Bevacizumab TCO/mAb
1/6th	1.12 ± 0.03
1/3rd	1.13 ± 0.09

Also, a kinetic study, quenching the mTzCy3 incubation at different time points (1 - 45 min), was carried out. Therefore, Bevacizumab was reacted with 50 eq. TCO-NHS for 60 min at RT, purified, split into 7 fractions and incubated at room temperature with $1/6^{th}$ moles mTzCy3 (in relation to initiated TCO-NHS). After each time point the reaction was stopped by spin filtration. The determined ratios of conjugated TCO per mAb didn't alter significantly between 1 min and 45 min (Table 2), which led to the conclusion that already after 1 min a quantitative reaction was achieved. This outcome was expected as the reaction between TCO and tetrazine, the inverse-electron-demand Diels Alder reaction, is known and used for its very fast and clean reaction (see Chapter 1, paragraph 1.3.1 Bioorthogonal 'click' reaction).

Table 2: Results of kinetic study for the click reaction between Bevacizumab-TCO and mTzCy3 from 1 min to 45 min incubation time at room temperature.

	Bevacizumab
Incubation time (min)	average ratio TCO/mAb
1	2.3
5	2.3
10	2.3
15	2.3
20	2.2
30	2.2
45	2.2

In conclusion, it could be shown that there is no interference in the UV-VIS spectra with the mAb signal due to tetrazine or NHS after the click reaction and a quantitative binding of mTzCy3 could be assured to all available TCO moieties after one minute incubation using $1/6^{th}$ moles of the initial amount of TCO-NHS. Therefore, the plausibility of the method was approved and the evaluation of the mAb conjugation could be performed.

Once demonstrated that the titration method shows no interferences and that the reaction between TCO and tetrazine is quantitative, we tackled the determination of the number of TCO moieties attached and available at the mAb for different mAb/TCO reaction ratios. With that aim, and as described above, the antibody was reacted in different molar ratios with TCO-NHS, purified and incubated with mTzCy3 (Figure 5). After purification by spin filter samples were measured using UV-VIS spectrophotometry (Figure 8) and the concentrations of the antibody as well as the concentrations of the fluorophore (which equals the concentration of bound and available TCOs) were determined.

Noteworthy, precipitation of mAb was observed when high molar ratios of TCO per mAb (≥100:1) were used. The precipitation is, most likely, due to reduced solubility of highly loaded mAbs, either due to loss of their net surface charge by conjugation to lysine residues and/or due to increased hydrophobicity as a consequence of incorporation of ligands (18). The precipitation phenomenon was clearly reflected in the UV-VIS spectra, were lower antibody concentrations were found at high TCO/mAb ratios due to worse recovery from the spin filter after purification (Figure 8).
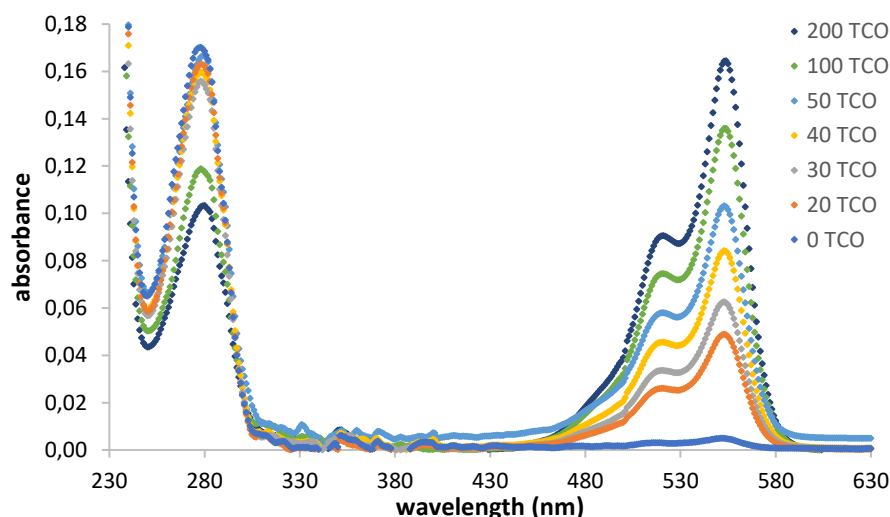
Figure 8: UV-VIS spectra of the direct analysis of mAb-TCO conjugates (here Bevacizumab) with the tetrazine-fluorophore (mTzCy3); TCO was coupled in molar ratios of 1:20, 1:30, 1:40, 1:50, 1:100, 1:200 and 1:0 as control.

Table 3: Results of conjugation efficacy (average TCO/mAb) by direct analysis for Bevacizumab and Trastuzumab (values are expressed as mean ± standard deviation, n(Bevacizumab) ≥ 3, n(Trastuzumab) ≥ 2).

	Bevacizumab	Trastuzumab
Coupling ratio mAb:TCO-NHS	Resulting average conjugate TCO/mAb	
1:0	0.0 ± 0.0	0.0 ± 0.0
1:20	0.6 ± 0.0	1.0 ± 0.3
1:30	1.0 ± 0.1	1.6 ± 0.1
1:40	1.3 ± 0.1	2.0 ± 0.5
1:50	1.9 ± 0.4	2.1 ± 0.1
1:55		2.5 ± 0.8
1:100	2.9 ± 0.4	
1:200	5,2	

The results show that, even after optimizing the reaction conditions, independent of the ratio, the coupling of TCO-NHS to Bevacizumab had a yield of roughly 3 %, to Trastuzumab about 5 %. In other words: out of 30 deployed TCO-NHS only about 1 and 1.6 TCO were bound to Bevacizumab or Trastuzumab, respectively. The most likely reason for the low yield is the instability of NHS-ester in aqueous conditions. The hydrolysis of TCO-NHS into TCO-OH and NHS-OH is faster than the aminolysis, the desired coupling reaction to the amine group (19). The results shown in Table 3 for high ratios of TCO-NHS (1:100 and 1:200) per mAb need to be handled with doubts. As mentioned before, precipitation of the mAb was observed and full recovery of the conjugated mAb from the spin filter wasn't possible. That could have resulted in a false determination of bound TCO/mAb as it is likely that a fraction of mAb with higher conjugations was precipitated, not recovered and therefore not embraced in the asserted result. To yet enable a comparison between the different ratios, despite the loss of antibody in the 1:100 and 1:200 reaction-ratios, the ratio

of the maximum absorbance between the fluorescence (corresponding to available TCO, at 550 nm) and the mAb (at 280 nm) was determined, using the average of all measurements, and is presented in Table 4 as well as in a normalized UV-VIS spectra (Figure 9).

Table 4: Ratio of the absorbance for Bevacizumab conjugations with TCO between the maximum absorbance of the fluorescence (corresponding to TCO) at around 550 nm and the maximum absorbance of the mAb at around 280 nm.

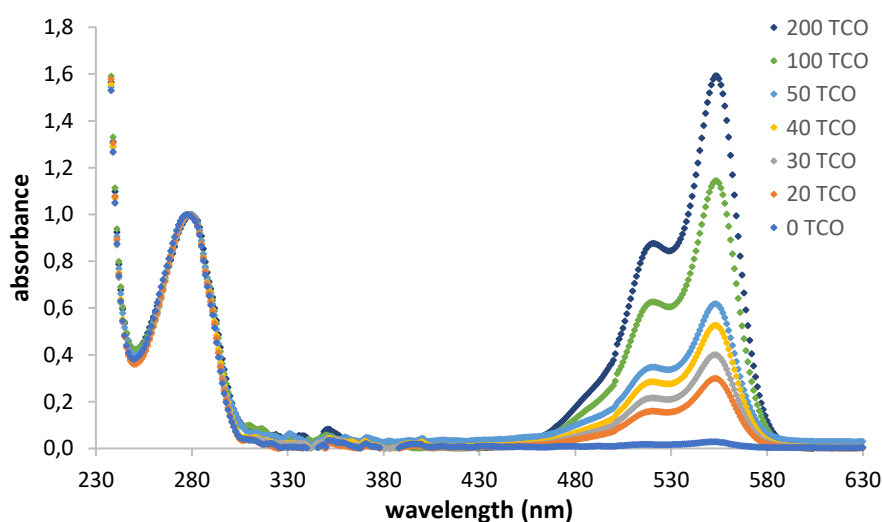|	Bevacizumab
Coupling ratio mAb:TCO-NHS	Ratio of absorbance 550 nm/280 nm
1:0	0.0
1:20	0.3
1:30	0.4
1:40	0.5
1:50	0.6
1:100	1.1
1:200	1.6

Figure 9: Normalized UV-VIS spectra of the direct analysis of mAb-TCO conjugates (here Bevacizumab) with the tetrazine-fluorophore (mTzCy3); TCO was coupled in molar ratios of 1:20, 1:30, 1:40, 1:50, 1:100, 1:200 and 1:0 as control.

The absorbance-ratio between the fluorophore and the mAb show clearly that the conjugation, even though it is a random conjugation, increases proportional to the ratio of the initial reaction-ratio. Looking closer to the higher ratios; the 1:100 reaction is with 1.1 close to the expected ratio, which would be 1.2, twice the ratio of 1:50, whereas the 1:200 is with only 1.6 further away, verifying the theory, that we weren't able to determine the real ratio due to the precipitation of highly conjugated antibody.

3.3.2 DFO conjugation – direct method

The conjugation with the chelator *p*-NCS-Bz-DFO enables the radiolabeling of antibodies with the radionuclide ^{89}Zr. The conjugation was again random to lysine residues of either

Bevacizumab or Trastuzumab; however, this time the coupling was not through an NHS ester as for TCO but via isothiocyanate coupling. For the direct evaluation of the obtained average conjugate, titrations with [89]Zr spiked Zirconium were performed (Figure 10) (20). Therefore, the production of a "cold" (non-radioactive) Zirconium oxalate solution ([90]Zr(C$_2$O$_4$)$_2$) with precise defined concentration was necessary. Zirconium chloride was dissolved in 4 M HCl and a trace of [89]Zr (0.1 - 0.2 μCi; 3700 - 7400 Bq) was added. The solution was passed over a hydroxamate column to trap Zr^{4+}. After washings with hydrochloric acid and water the column was eluted with 1 M oxalic acid and Zr-oxalate collected in different fractions. The radioactivity of each was measured in a gamma counter (Wallach Wizard, PerkinElmer) and used to determine the concentrations. After the zirconium oxalate solutions were decayed the titration could be performed. Therefore, Trastuzumab was conjugated with different molar-equivalents (3, 5, 10 eq.) of *p*-NCS-Bz-DFO and purified. For each conjugation four equal fractions were taken and respectively incubated with a different ratio (0, 1, 2 and 3 molar eq. Zr^{4+} per mAb) of "cold" Zirconium ([90]Zr-oxalate), which however, contained the same trace of "hot" Zirconium ([89]Zr-oxalate, radioactive). After purification with size exclusion column (PD10 GE Healthcare) the radioactivity of each of the four mAb fractions was determined and the fraction with zero eq. of "cold" zirconium was normalized to 100 % labeling yield. The percentage calculated for the other fractions presented the amount of captured Zirconium out of the excess. Naturally, the more "cold" zirconium was added, the less "hot" zirconium was bound and the labeling yield decreased (Figure 11). Out of those relations the average amount of *p*-NCS-Bz-DFO per mAb could be calculated.

Figure 10: *p*-NCS-Bz-DFO conjugation and Zirconium titration to determine average ratio of DFO/mAb via direct radiometric method.
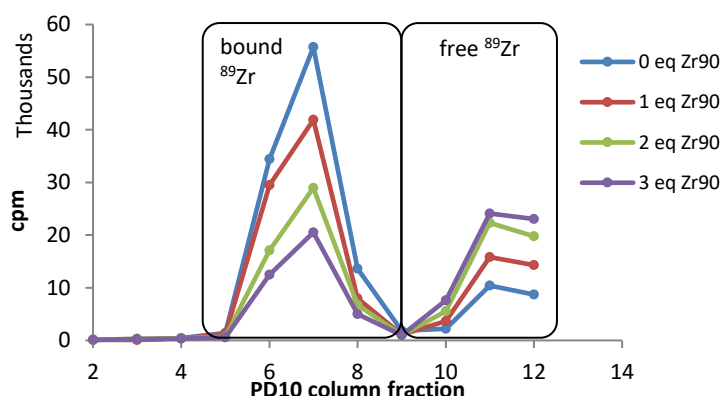

Figure 11: Graphical representation of PD10 purification after [89]Zr spiked labeling to visualize different labeling yields respectively to the excess of "cold" Zirconium.

The results of the *p*-NCS-Bz-DFO conjugation to Bevacizumab and Trastuzumab are shown in Table 5. The coupling yield between DFO and Bevacizumab is slightly higher with 29 %

(3 eq.) 25 % (5 eq.) and 14 % (10 eq.), whereas Trastuzumab achieves yields of only 4 % (3 eq.) 14 % (5 eq.) and 13 % (10 eq.). Unexpected is the very low yield for Trastuzumab with 3 eq. p-NCS-Bz-DFO. A possible explanation could be a wrong determination of the deployed "cold" Zirconium oxalate solution, which was produced on site out of Zirconium chloride ($ZrCl_4 + C_2H_2O_4 * 2\,H_2O \xrightarrow{Hydroxamte\ column} Zr(C_2O_4)_2$) as described above. A repetition of the experiments, including the production of Zirconium oxalate followed by the titration of the DFO conjugated mAb, should be carried out.

Table 5: Results of conjugation efficacy (average DFO/mAb) by direct analysis for Bevacizumab and Trastuzumab (values are expressed as mean ± standard deviation, n = 2).

	Bevacizumab	Trastuzumab
Coupling ratio mAb:p-NCS-Bz-DFO	Resulting average conjugate DFO/mAb	
1:3	0.87 ± 0.32	0.13 ± 0.01
1:5	1.26 ± 0.33	0.70 ± 0.35
1:10	1.47 ± 0.30	1.31 ± 0.20

The objective of this chapter was the determination of obtained ratios after random conjugation between ligand and antibody, using different analytical methods to reveal possible differences of the number of available and actually attached ligands. After the direct analysis by titration of the two ligands, TCO and DFO, mass analyses were performed.

3.3.3 Analysis with MALDI/TOF MS

MALDI is a mild, fast and rather easy method to determine the mass of biomolecules; consequently, it is a commonly used method to analyze antibody-drug-conjugates (18). A typical antibody spectrum shows two signals, corresponding to the single and double charged species of the mAb (Figure 12). By attaching a ligand to the mAb, such as a drug or chelator, the mass increases by a multiple number of the mass of the moiety, leading to a shift of the peak center. Hence the antibody loading can be calculated from the change of the peak position.

To analyze the antibody-samples by MALDI a buffer exchange from PBS (storage buffer) into 0.1 % TFA in water was performed via spin filtration. The samples were measured using the dried droplet method on a polished stainless-steel probe (Bruker Daltonics) using 1 μL sample mixed with 1 μL sDHB matrix (for details see 3.5 Experimental part.)
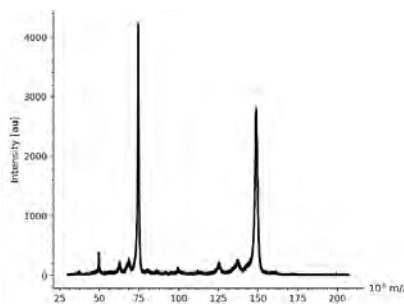

Figure 12: MALDI spectrum of native Bevacizumab, showing the single (150 000 m/z) and double charged (75 000 m/z) species.

As mentioned before, using random conjugation to lysine residues of the mAb yields in a variety of conjugates (Figure 4). Together with the fact that the ligands used in this work are small (TCO: 152 Da and DFO: 753 Da) compared to the size of the mAb (150 kDa) the shift of the peak center between the native mAb and its conjugates was small and difficult to identify as such. Additionally, MALDI-TOF has a relatively poor mass accuracy for large molecules like mAbs (18) and does therefore not give high enough resolution to separate the different species obtained after random conjugation. Hence, mathematical fittings were executed to determine the distribution of present conjugates. The peak of the native mAb was used as reference and fitted with a Lorentz distribution. To analyze the conjugates the multiple mass of the ligand was added to the Lorentzian fit of the native mAb (Figure 13).
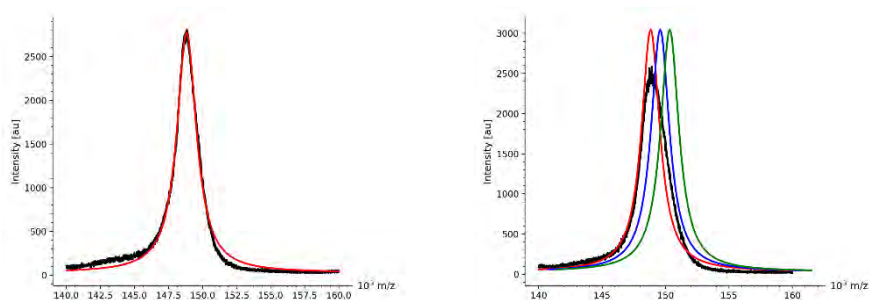
Figure 13: Left: Lorentzian fit to the single charged MALDI signal of native Bevacizumab; right: Lorentzian fit of mAb conjugates with 0 (red), 1 (green) and 2 (blue) DFO added, overlaying the single charged MALDI signal of Bevacizumab conjugated with 5 eq. DFO (black).

Finally the spectra of the conjugates were fitted to identify the percentage of different conjugates obtained after random conjugation of either 3, 5 or 10 eq. p-NCS-Bz-DFO or 30, 40 or 50 eq. TCO-NHS to the two different antibodies Bevacizumab and Trastuzumab (Figure 14 and Figure 15, Table 6 and Table 7).

Figure 14: Mathematical fittings of exemplary MALDI spectra of Bevacizumab conjugated with 0, 3, 5 or 10 eq. DFO (raw data in black) and fitted with Lorentzian distribution for the conjugates with 0 (red), 1 (blue), 2 (green) and 3 (gold) DFO.

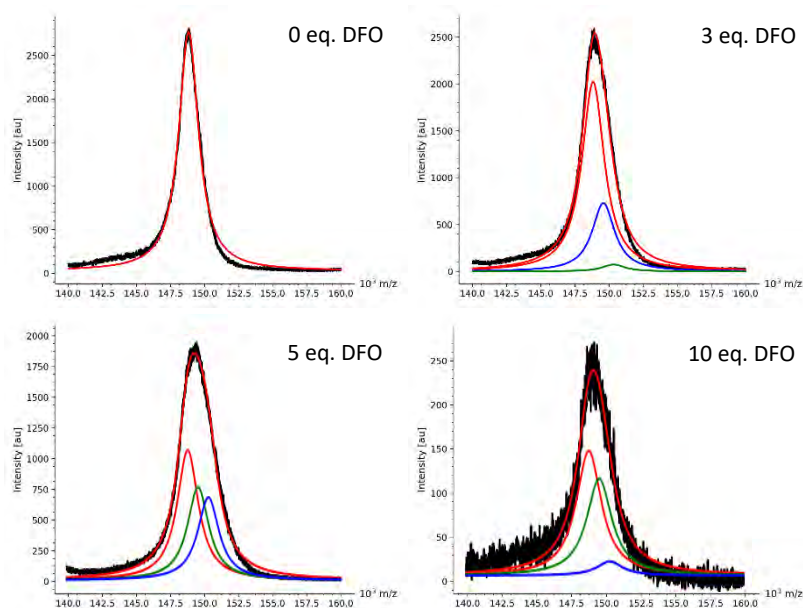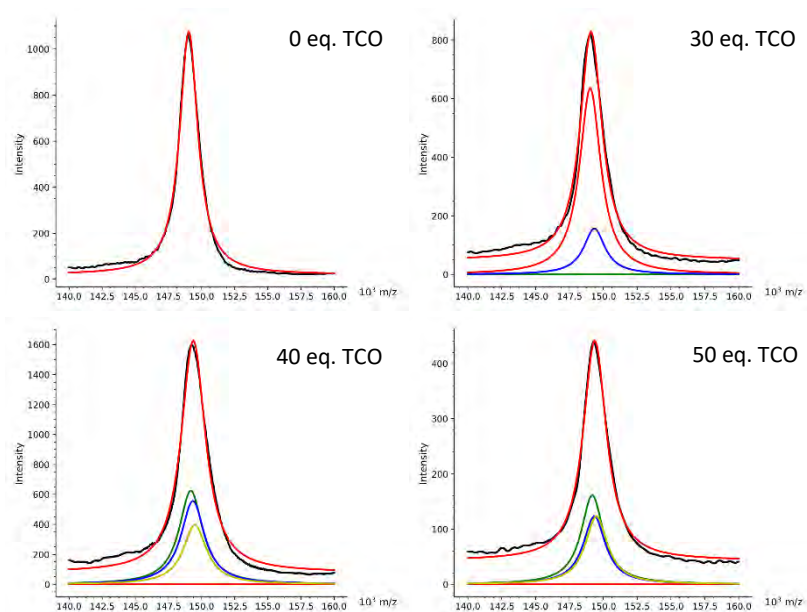**Figure 15:** Mathematical fittings of exemplary MALDI spectra of Bevacizumab conjugated with 0, 30, 40 or 50 eq. TCO (raw data in black) and fitted with Lorentzian distribution for the conjugates with 0 (red), 1 (green), 2 (blue) and 3 (gold) TCO.

Table 6: Results of conjugation efficacy (average DFO/mAb) by MALDI analysis for Bevacizumab and Trastuzumab. In bold the average conjugate, below the percentage of mAb with 0, 1, 2 or 3 DFO (values are expressed as mean $\pm$ standard deviation, n = 2).

		Bevacizumab	Trastuzumab
Coupling ratio mAb:*p*-NCS-Bz-DFO	DFO/mAb	**average conjugate** and distribution DFO/mAb	
1:3	Ø	**0.50 $\pm$ 0.27**	**0.25 $\pm$ 0.36**
	0	62.09 $\pm$ 13.04 %	78.71 $\pm$ 30.11 %
	1	25.52 $\pm$ 0.48 %	17.44 $\pm$ 24.66 %
	2	12.40 $\pm$ 13.88 %	3.85 $\pm$ 5.45 %
1:5	Ø	**0.78 $\pm$ 0.09**	**0.28 $\pm$ 0.31**
	0	47.52 $\pm$ 7.16 %	77.53 $\pm$ 27.25 %
	1	26.95 $\pm$ 4.93 %	16.85 $\pm$ 23.34 %
	2	25.53 $\pm$ 2.23 %	5.63 $\pm$ 3.91 %
1:10	Ø	**0.95 $\pm$ 0.59**	**0.49 $\pm$ 0.13**
	0	41.37 $\pm$ 16.33 %	57.97 $\pm$ 3.52 %
	1	34.11 $\pm$ 9.80 %	35.03 $\pm$ 6.38 %
	2	13.13 $\pm$ 10.02 %	7.00 $\pm$ 9.90 %
	3	11.39 $\pm$ 16.11 %	

Table 7: Results of conjugation efficacy (average TCO/mAb) by MALDI analysis for Bevacizumab and Trastuzumab. In bold the average conjugate, below the percentage of mAb with 0, 1, 2 or 3 TCO (values are expressed as mean $\pm$ standard deviation, n = 2).

Coupling ratio mAb:TCO-NHS	TCO/mAb	Bevacizumab	Trastuzumab
		average conjugate and distribution TCO/mAb	
1:30	Ø	**0.65 $\pm$ 0.36**	**1.20 $\pm$ 1.13**
	0	67.64 $\pm$ 17.79 %	40.11 $\pm$ 56.72 %
	1	-	-
	2	32.36 $\pm$17.79 %	59.89 $\pm$ 56.72 %
1:40	Ø	**1.76 $\pm$ 0.13**	**2.15 $\pm$ 0.41**
	0	-	-
	1	45.57 $\pm$ 8.39 %	19.82 $\pm$ 28.03 %
	2	32.41 $\pm$ 4.10 %	45.39 $\pm$ 14.87 %
	3	22.02 $\pm$ 4.29 %	34.79 $\pm$ 13.15 %
1:50	Ø	**2.45 $\pm$ 0.76**	**2.04 $\pm$ 0.20**
	0	-	-
	1	19.80 $\pm$ 28.00 %	31.14 $\pm$ 11.96 %
	2	15.85 $\pm$ 20.31 %	33.30 $\pm$ 4.37 %
	3	64.35 $\pm$ 48.30 %	35.56 $\pm$ 7.59 %

Even though MALDI/TOF MS is a common method to evaluate antibody-drug-conjugates, in our hands the results were not optimal. Looking at the values the expected trends can mostly be adumbrated (moiety/mAb increases with higher molar ratios in the coupling reaction whereas non/low-conjugated mAb decreases). Yet, the high standard deviation reveals that the results might be questionable, probably due to the low mass of the attached moiety, which makes the fitting process difficult. Comparing the two different mAbs with each other, Bevacizumab presents more reasonable values and overall higher conjugation yields than Trastuzumab.

Finally, the second mass analytical method UPLC/ESI-TOF MS was performed. It has supposedly higher mass accuracy and resolution than MALDI (18).

3.3.4 Analysis with UPLC/ESI-TOF MS
LCMS is a tandem of liquid chromatography (LC) and mass spectrometry (MS) with very high sensitivity and selectivity, using LC to separate species in a heterogenic mixture combined with MS for mass analysis. Analyzing antibodies leads to a wide range of different charged molecules (other than in MALDI where only the single and double charged mAb-species emerge), which again results in a spectrum showing numerous signals of highly charged species (Figure 16, left). Even though the resolution for LCMS is higher than for MALDI, a complete separation between the obtained mAb-derivatives after random conjugation is challenging or even impossible. Looking at a LCMS spectrum of, for example, DFO conjugated mAb, each peak of a charged species does show a signal split into numerous ones. Each "shoulder" represents another derivative (Figure 16, right).
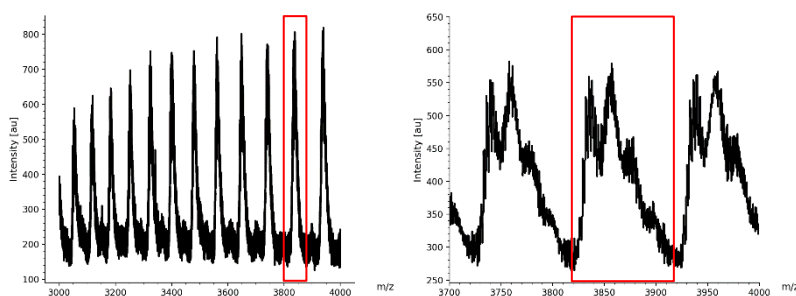
Figure 16: Left: section of an LCMS spectrum of native Bevacizumab with charged species between +49 and +38; right: section of a denoised LCMS spectrum of Bevacizumab conjugated with 5 eq. *p*-NCS-Bz-DFO between species charged with +40 and +38. Framed in red, the exemplary chosen respectively mAb species for mathematical fittings with charge +39.

To analyze the spectra of the different conjugates one signal of charge was chosen to apply mathematical fittings. First, to improve the spectra, a denoising algorithm was performed. Doing so, the spectrum of the native mAb presents not the, at first expected, Gaussian shape signal but a signal with many sub-signals, like a flame. This appearance is most likely due to glycan variations (21). Interestingly, this phenomenon is also visible in the LCMS of the conjugated mAbs, however, only in the respectively first shoulder of each signal/charge which corresponds to the percentage of the heterogenic mixture that doesn't show conjugation, hence, is still native mAb (Figure 17).
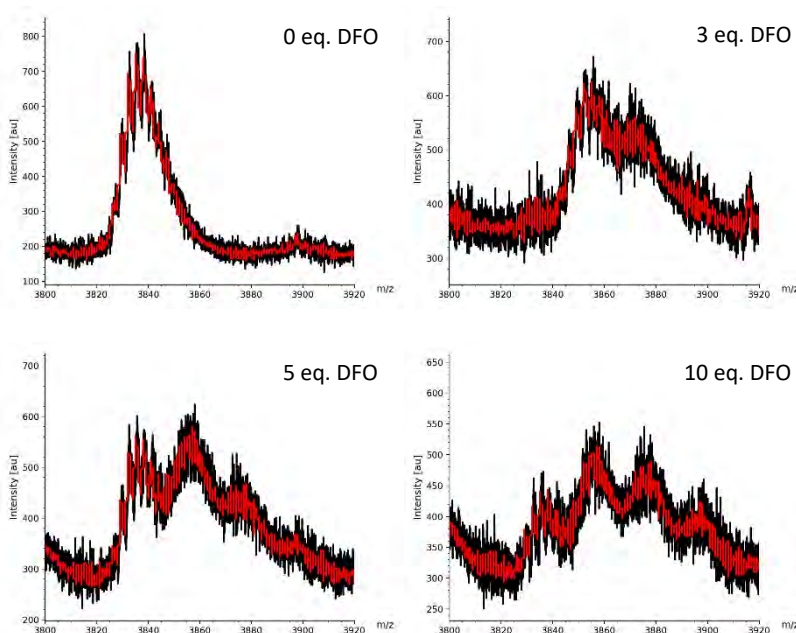
Figure 17: Raw LCMS data (black) of Bevacizumab conjugated with 0, 3, 5 or 10 eq. *p*-NCS-Bz-DFO, improved with a denoising algorithm (red).

Next, to fit the data, bigaussian lineshapes were used (as for this work we weren't interested in the glycans we handled the signal of the native mAb as Gaussian distribution) to identify the distribution of the different conjugates obtained after random conjugation of either 3, 5 or 10 eq. *p*-NCS-Bz-DFO or 30, 40 or 50 eq. TCO-NHS to the two different antibodies Bevacizumab and Trastuzumab. Native mAb was used as reference to force the position of

the center. The fitted positions of the conjugates were calculated by the formula:

$$center_{new} = center_{native\ mAb} * \frac{150\ 000 + n*753}{150\ 000}$$ (Figure 18).
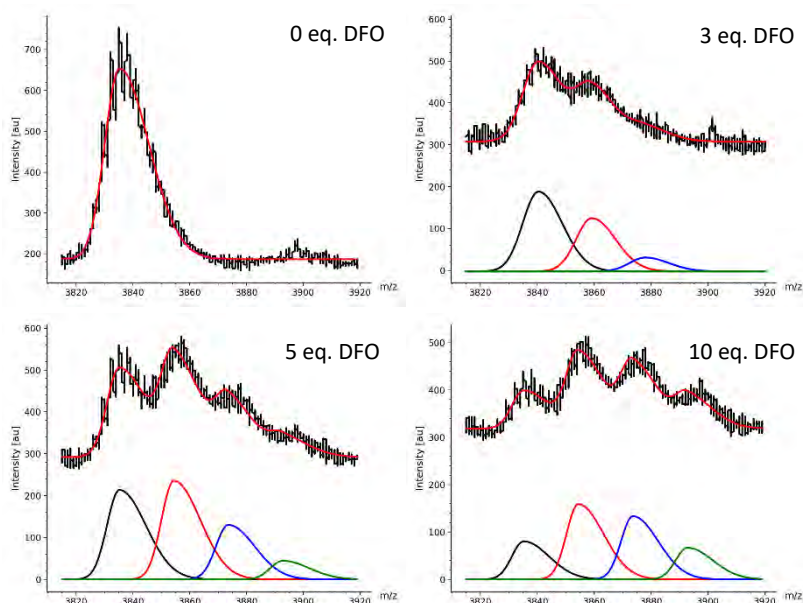

Figure 18: Mathematical fittings of exemplary LCMS spectra for DFO conjugations of Bevacizumab, using bigaussian lineshapes (top of the images: denoised data in black, fitted lineshape in red), obtaining mAb derivatives (bottom of the images) with 0 (black), 1 (red), 2 (blue) or 3 (green) DFO.

As mentioned above, the analysis of the obtained mAb derivatives is quite challenging due to the small size of the ligands compared to the mAb. This is even more obvious looking at TCO, which only contains $1/5^{th}$ of the mass compared to DFO. Hence, LCMS spectra show no separation or shoulders, only a broadening of the signal can be observed (Figure 19). The fittings were also performed with bigaussian lineshapes.
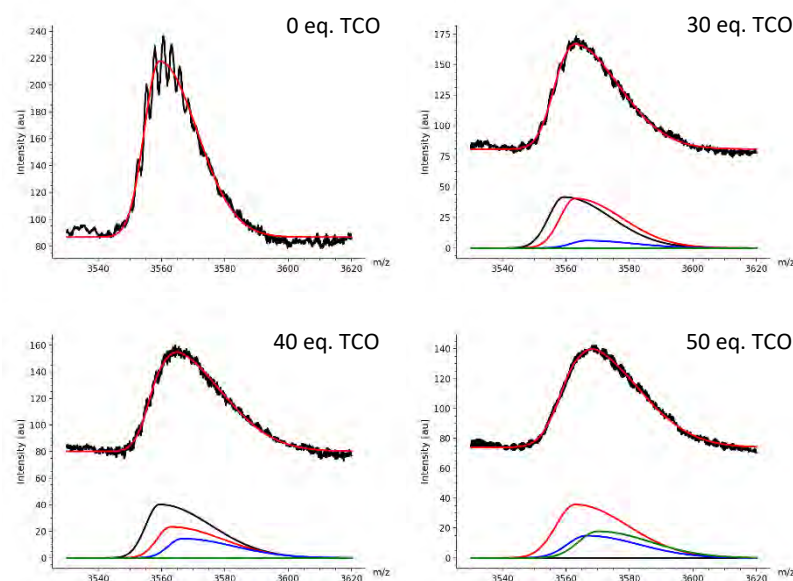

Figure 19: Mathematical fittings of exemplary LCMS spectra for TCO conjugations of Bevacizumab, using bigaussian lineshapes (top of the images: denoised data in black, fitted lineshape in red), obtaining mAb derivatives (bottom of the images) with 0 (black), 1 (red), 2 (blue) or 3 (green) TCO.

The following two tables (Table 8 and Table 9) show the results of the fittings; represented are the values of the average obtained conjugate (moiety/mAb) as well as the determined percentage of each species in the obtained mixture of conjugates.

Table 8: Results of conjugation efficacy (average DFO/mAb) by LCMS analysis for Bevacizumab and Trastuzumab. In bold the average conjugate, below the percentage of mAb with 0, 1, 2 or 3 DFO (values are expressed as mean ± standard deviation, n = 2).

Coupling ratio mAb:*p*-NCS-Bz-DFO	DFO/mAb	Bevacizumab	Trastuzumab
		average conjugate and distribution DFO/mAb	
1:3	Ø	**0.63 ± 0.11**	**1.02 ± 0.01**
	0	51.13 ± 4.54 %	34.81 ± 1.55 %
	1	35.87 ± 0.48 %	35.74 ± 2.07 %
	2	11.75 ± 3.25 %	21.62 ± 0.11 %
	3	1.26 ± 1.78 %	7.84 ± 0.42 %
1:5	Ø	**1.02 ± 0.01**	**1.21 ± 0.05**
	0	33.00 ± 1.61 %	27.14 ± 1.62 %
	1	38.42 ± 0.92 %	35.60 ± 1.21 %
	2	22.14 ± 1.77 %	26.47 ± 2.68 %
	3	6.43 ± 1.08 %	10.78 ± 0.15 %
1:10	Ø	**1.48 ± 0.08**	**1.65 ± 0.15**
	0	17.06 ± 1.78 %	15.83 ± 5.47 %
	1	34.10 ± 2.85 %	26.30 ± 1.74 %
	2	32.15 ± 2.55 %	35.10 ± 5.05 %
	3	16.69 ± 2.07 %	22.77 ± 2.17 %

The results of the LCMS analysis for DFO conjugations (Table 8) show very nicely the expected trends that could merely be seen with MALDI. The amount of chelator coupled to mAb increases with higher equivalents of DFO during the reaction, from 0.6 and 1.0 DFO per mAb with 3 equivalents to 1.5 and 1.7 DFO/mAb after the reaction with 10 eq. *p*-NCS-Bz-DFO (Bevacizumab and Trastuzumab, respectively). Also, looking at the distribution of species in each conjugate mixture, the amount of non-modified mAb decreases, whereas the amount of higher conjugated mAbs increases with higher equivalents of DFO (e.g. from 1.3 % to 16.7 % for Bevacizumab with 3 DFO). Comparing the two different mAbs with each other Bevacizumab presents overall slightly lower conjugation yields than Trastuzumab.

Looking at the TCO conjugations (Table 9) much higher standard deviations can be witnessed, which can be explained by the, as above mentioned, smaller size of the ligand. Having such big errors does make it difficult to talk about trends or discuss the results; the obtained values should be questioned and the value of the results raised by increasing n.

Table 9: Results of conjugation efficacy (average TCO/mAb) by LCMS analysis for Bevacizumab and Trastuzumab. In bold the average conjugate, below the percentage of mAb with 0, 1, 2 or 3 TCO (values are expressed as mean ± standard deviation, n = 2, *n = 1).

Coupling ratio mAb:TCO-NHS	TCO/mAb	Bevacizumab	Trastuzumab
		average conjugate and distribution TCO/mAb	
1:30	Ø	**0.57 ± 0.04**	**0.58 ± 0.55**
	0	53.74 ± 9.22 %	60.56 ± 28.51 %
	1	35.55 ± 14.61 %	20.52 ± 1.76 %
	2	10.70 ± 5.39 %	18.91 ± 26.75 %
1:40	Ø	**0.66 ± 0.01**	**1.22 ± 0.81**
	0	57.61 ± 8.64 %	44.25 ± 39.47 %
	1	25.80 ± 5.82 %	13.49 ± 19.08 %
	2	9.30 ± 13.15 %	18.76 ± 0.53 %
	3	7.30 ± 10.32 %	23.50 ± 20.91 %
1:50	Ø	**1.74***	**0.95 ± 0.75**
	0	-	51.21 ± 35.72 %
	1	52.25 %	17.68 ± 17.77 %
	2	21.73 %	16.26 ± 3.04 %
	3	26.02 %	14.85 ± 21.00 %

3.3.5 Comparison between the different methods

If we look at the results obtained after conjugations with the chelator DFO (Table 10), correlations can be seen between all three methods for both antibodies. However, MALDI deviates the furthest, especially for Trastuzumab, in the average value of DFO/mAb compared to the other two methods. The most trustworthy method to analyze DFO conjugates, confirmed with the lowest standard deviation, is the LCMS method. One question that we wanted to answer by using different analysis methods was if the number of ligands per mAb is smaller when using direct methods compared to mass analytic, which would reveal that some of the ligands, bound to the mAb, are not actually available due to interactions with the mAb. Leaving the ratios obtained by MALDI aside due to its questionable results (explained above), we can see slightly higher ratio for DFO conjugations for Trastuzumab with the LCMS method compared to the direct method. However, for Bevacizumab an opposite trend is visible. Taking into account that the standard deviation for the direct method is relatively high, no clear answer can be given. Yet, an increase in n could lead to more significant results.

Table 10: comparison of DFO conjugation efficacy between different analytical methods for Bevacizumab (top) and Trastuzumab (bottom) (values are expressed as mean ± standard deviation, n = 2).

Bevacizumab	direct	LCMS	MALDI
Coupling ratio mAb:*p*-NCS-Bz-DFO	Resulting average conjugate DFO/mAb		
1:3	0.87 ± 0.32	0.63 ± 0.11	0.50 ± 0.27
1:5	1.26 ± 0.33	1.02 ± 0.01	0.78 ± 0.09
1:10	1.47 ± 0.30	1.48 ± 0.08	0.95 ± 0.59

Trastuzumab	direct	LCMS	MALDI
Coupling ratio mAb:*p*-NCS-Bz-DFO	Resulting average conjugate DFO/mAb		
1:3	0.13 ± 0.01	1.02 ± 0.01	0.25 ± 0.36
1:5	0.70 ± 0.35	1.21 ± 0.05	0.28 ± 0.31
1:10	1.31 ± 0.20	1.65 ± 0.15	0.49 ± 0.13

Looking at the ligand/mAb ratios after conjugation with the pre-targeting ligand TCO (Table 11) correlations are more difficult to observe. The trend, to obtain higher conjugated antibodies with increased equivalents of ligand during the conjugation reaction, is visible in all methods for Bevacizumab, yet, for Trastuzumab only for the direct method. But high standard deviations make the results by MALDI and LCMS questionable. The most trustworthy method to analyze TCO conjugates, confirmed with the lowest standard deviation, is the direct method. As explained earlier, the small molecular mass of TCO compared to the mAb makes mass analysis challenging. Yet again, an increase in n could lead to more significant results.

Table 11: comparison of TCO conjugation efficacy between different analytical methods for Bevacizumab (top) and Trastuzumab (bottom) (values are expressed as mean ± standard deviation, n(direct) ≥ 2, n(mass) = 2).

Bevacizumab	direct	LCMS	MALDI
Coupling ratio mAb:TCO-NHS	Resulting average conjugate TCO/mAb		
1:30	1.0 ± 0.1	0.57 ± 0.04	0.65 ± 0.36
1:40	1.3 ± 0.1	0.66 ± 0.01	1.76 ± 0.13
1:50	1.9 ± 0.4	1.74	2.45 ± 0.76
Trastuzumab	direct	LCMS	MALDI
Coupling ratio mAb:TCO-NHS	Resulting average conjugate TCO/mAb		
1:30	1.6 ± 0.1	0.58 ± 0.55	1.20 ± 1.13
1:40	2.0 ± 0.5	1.22 ± 0.81	2.15 ± 0.41
1:50	2.1 ± 0.1	0.95 ± 0.75	2.04 ± 0.20

3.4 Summary and conclusion

This chapter describes the analysis of two different monoclonal antibodies (Bevacizumab and Trastuzumab), randomly conjugated with two different ligands (*trans*-cyclooctene and a desferrioxamine derivative) by three different methods (one direct titration and two mass analyses: MALDI and LCMS). The direct method enables the determination of the average number of available ligands per mAb via titration, whereas the mass analyses reveal the average of the total number of attached moieties and furthermore allow the determination of the distribution of conjugates in the obtain heterogenic mixture.

The direct method of the TCO conjugation, a titration with a tetrazine-fluorophore, shows reliable and reproducible results. The low yield of the conjugation (several tenfold molar equivalents to the mAb are necessary) can be explained by fast hydrolysis of the TCO-NHS

ester. For the DFO conjugation much lower reaction ratios are sufficient as the coupling is performed via isothiocyanate. The direct method for DFO, the titration with radioactive spiked zirconium oxalate, is somewhat more complex and susceptible, compared to the TCO titration, which is documented by higher standard deviations. However, the results show the expected trend and correlate with the LCMS analysis.

Even though, MALDI is a commonly used method to analyze antibody drug conjugates, in our hands the results were questionable; high standard deviations and major differences in results compared to both other methods were witnessed.

The analysis of mAb conjugates with such small ligands is clearly challenging. However, looking at the LCMS spectra, high mass accuracy and resolution can be observed after DFO conjugation. Yet, the analysis of TCO conjugations, with TCO being still 5 times smaller compared to DFO, shows much higher standard deviations, hence less accuracy.

Overall, the two different antibodies showed quite similar trends and values. However, Trastuzumab reveals slightly higher conjugation yields.

3.5 Experimental part

3.5.1 Reagents

All reagents were obtained from Sigma-Aldrich unless otherwise stated. Deionized water (18 MΩ) was used in all reactions. *p*-NCS-Bz-DFO was obtained from CheMatech (cat. No. C121). Both antibodies (Bevacizumab and Trastuzumab) were purchased from Roche Farma, S.A. España. $[^{89}Zr]ZrC_2O_4$ (in 1 M oxalic acid) was produced in house by a (p, n) reaction of natural yttrium-89 and isolated with a hydroxamate column following standard protocol.

3.5.2 Instrumentation

UV-Vis spectra were measured with a Jasco V630BIO Spectrophotometer or with NanoDrop® ND-1000 V3.5.2

Gamma counts were measured using a Wallach Wizard, PerkinElmer (Waltham, MA, USA) gamma counter.

MALDI/TOF MS analyses were performed using a UltrafleXtreme III, Bruker Daltonics (frequency-tripled (355 nm) Nd:YAG laser) with positive ion mode / Linear mode m/z 30-180 kDa laser fluence 90% / Laser frequency 1000 Hz and Laser shots accumulated >5000. The samples were measured using the dried droplet method on a polished stainless-steel probe (Bruker Daltonics) using 1 μL sample mixed with 1 μL sDHB matrix (10 mg/mL super-DHB in 25 % acetonitrile and 75 % TFA (0.1 %) in water).

UPLC/ESI-TOF MS analyses were performed using an AQUITY UPLC separation module coupled to an LCT TOF Premier XE mass spectrometer (Waters, Manchester, UK). An Acquity BEH C4 column (150x2.1 mm, 1.7 μm) was used as stationary phase. The elution buffers were A (water and 0.1% TFA) and B (Acetonitrile and 0.1% TFA). The column was eluted with a gradient: t=0 min, 95% A, 5% B; t=2 min, 95% A, 5% B; t=35 min, 25% A, 75% B; t=40 min, 25% A, 75% B; t=41 min, 95%A, 5% B; t=45 min, 95%A, 5% B. Total run was 45 min, injection volume was 10 μL and the flow rate 200 μL/min with a column temperature of 70 °C. The detection was carried out in positive ion mode, monitoring the most abundant isotope peaks from the mass spectra (M+H$^+$).

3.5.3 Chemistry; TCO conjugation

Conjugation of TCO-NHS to mAb
The mAb was diluted in PBS (phosphate-buffered saline, pH 7.4) to a concentration of 1.5 – 3.0 mg/mL. The pH was adjusted to 8.6 – 8.9 with 0.1 M Na₂CO₃. TCO-NHS (*trans*-cyclooctene-NHS-ester, 20 mM in DMSO) was added in different ratios (0, 20, 30, 40, 50, 55, 100 and 200 molar eq. TCO-NHS per mAb). After incubation (60 min, RT) non-reacted TCO-NHS was removed by spin filtration (100 kDa, 12000 rpm) and the conjugated mAb washed three times with PBS. After recovering the mAb from the filter with PBS its concentration was determined by NanoDrop®.

TCO conjugation – direct analysis - photometric
An aliquot of the TCO-conjugated mAb (0.05 mg) was taken and 5 – 10 molar eq. 6-Methyl-Tetrazine-Sulfo-Cy3 (mTzCy3, 1 mg/mL in DMSO) added. After 5 min incubation at RT

the fluorophore-labeled mAb was purified by spin filtration (100 kDa, 12000 rpm) and washed four times with PBS. After recovering the mAb from the filter with PBS the concentrations of mAb and mTzCy3 were determined by NanoDrop®. The ratio between mTzCy3 (which correlates to the available TCO moieties) and mAb was calculated.

Determination of quantitative reaction between mAb-TCO and mTzCy3

The mAb was diluted in PBS (phosphate-buffered saline, pH 7.4) to a concentration of 1.0 mg/mL. The pH was adjusted to 8.7 – 9.0 with 0.1 M Na_2CO_3. 30 molar eq. TCO-NHS (*trans*-cyclooctene-NHS-ester, 20 mM in DMSO) were added and incubated for 90 min at room temperature. Non-reacted TCO-NHS was removed by spin filtration (100 kDa, 12000 rpm) and the conjugated mAb washed three times with PBS. After recovery from the filter the mAb-TCO was split into 6 fractions and 3 each were incubated with $1/6^{th}$ or $1/3^{rd}$ molar 6-Methyl-Tetrazine-Sulfo-Cy3 (mTzCy3, 1 mg/mL in DMSO) of the initial amount of TCO-NHS. After 60 min incubation at RT the fluorophore-labeled mAb was purified by spin filtration (100 kDa, 12000 rpm) and washed four times with PBS. After recovering the mAb from the filter with PBS the concentrations of mAb and mTzCy3 were determined by UV-VIS spectrophotometry. The ratios between mTzCy3 and mAb were calculated and compared to each other.

Kinetic study between mAb-TCO and mTzCy3

The mAb was diluted in PBS (phosphate-buffered saline, pH 7.4) to a concentration of 1.0 mg/mL. The pH was adjusted to 8.7 – 9.0 with 0.1 M Na_2CO_3. 50 molar eq. TCO-NHS (*trans*-cyclooctene-NHS-ester, 20 mM in DMSO) were added and incubated for 60 min at room temperature. Non-reacted TCO-NHS was removed by spin filtration (100 kDa, 12000 rpm) and the conjugated mAb washed three times with PBS. After recovery from the filter mAb-TCO was diluted to 2 mL with PBS and 5 eq. (in relative to the mAb) 6-Methyl-Tetrazine-Sulfo-Cy3 (mTzCy3, 1 mg/mL in DMSO) were added. The mAb-TCO sample was split into 7 fractions of 250 µL and each reaction quenched by spin filtration (100 kDa, 12000 rpm) after 1, 5, 10, 15, 20, 30 and 45 min incubation at room temperature. After further washings with PBS the mAb-TCO-mTzCy3 was recovered with PBS from the filter and the concentrations of mAb and mTzCy3 determined by UV-VIS spectrophotometry. The ratios between mTzCy3 and mAb were calculated and compared to each other.

3.5.4 Chemistry; DFO conjugation

Conjugation of Df-Bz-NCS to mAb

The mAb was diluted in PBS to a concentration of 1.5 – 3.0 mg/mL. The pH was adjusted to 8.6 – 9.1 with 0.1 M Na_2CO_3. *p*-NCS-Bz-DFO (5 mM in DMSO) was added in different ratios (0, 3, 5 and 10 molar eq. per mAb). After incubation (45 min, 37 °C) non-reacted *p*-NCS-Bz-DFO was removed by spin filtration (100 kDa, 12000 rpm) and the conjugated mAb washed three times with PBS. After recovering the mAb from the filter with PBS its concentration was determined by NanoDrop®.

Radiolabeling of mAb with ^{89}Zr

Radiolabeling of mAb-DFO with ^{89}Zr was performed by incubation with $[^{89}Zr]ZrC_2O_4$ in a 1 M oxalic acid solution. Therefore 50 µl of 1 M oxalic acid containing ^{89}Zr (0.6 mCi = 22.2 MBq) were neutralized with 2 M sodium carbonate, 450 ug mAb was added and the

volume adjusted to 0.5 mL with 0.5 M HEPES buffer. After 1 h incubation at room temperature the mAb was purified by sephadex G-25 size exclusion column (NAP5® GE Healthcare) and PBS. Incubation and purification were monitored by iTLC (mobile phase: 20 mM citric acid + 60 mM EDTA 9:1 acetonitrile; Rf(mAb) = 0, Rf(^{89}Zr-EDTA) = 0.6). The radiochemical yield was 68 %.

Production of ^{90}Zr-oxalate solution

To produce Zirconium oxalate out of $ZrCl_4$ a hydroxamate functionalized resin was prepared and activated to work as a column. Therefore 100 mg of the resin was suspended in 4 mL saline and transferred into an Alltec® tube (volume 1 mL) with frit. The resin was washed with 20 mL acetonitrile, 30 mL saline and 12 mL 2 M HCl and pushed dry with air. 4 mg Zirconium chloride was dissolved in 4 M HCl and a trace of ^{89}Zr (0.1 - 0.2 μCi = 3700 – 7400 Bq) was added. The volume was adjusted to 15 mL with 4 M HCl and transferred to the hydroxamate column. For washings 4 times 2.5 mL 2 M HCl were used followed by 2 times 3 mL MQ-water. Finally, the column was eluted with 6 times 0.5 mL 1 M oxalic acid. All fractions were measured in a gamma counter (Wallach Wizard, PerkinElmer, Waltham, MA, USA) and the concentration of each calculated. The samples were stored to decay before used.

DFO conjugation – direct analysis - radiometric

The procedure to analyze DFO conjugated mAb was based on Meares et al. (20). Solutions of spiked zirconium oxalate in four different concentrations (0, 1, 2, 3 eq. Zr^{4+} per mAb with 0.1 - 0.2 μCi = 3700 - 7400 Bq each) were prepared. The pH was neutralized with 2 M Na_2CO_3, stabilized by HEPES buffer (0.5 M) and the antibody (0.45 mg each) added (final volume 500 μL). After one hour incubation at RT the four solutions were purified by sephadex G-25 size exclusion column (PD 10® GE Healthcare). The collected zirconium-labeled mAbs were measured in a gamma counter, the yield of the mAb with zero eq. Zirconium normalized to 100 % and the average ratio of *p*-NCS-Bz-DFO per mAb respectively calculated.

3.6 References

1. *Strategies and challenges for the next generation of antibody–drug conjugates.* **Alain Beck, Liliane Goetsch, Charles Dumontet and Nathalie Corvaïa.** s.l. : Macmillan Publishers Limited, 2017, NATURE REVIEWS, Vol. 16, p. 315.

2. *Antibody-Drug Conjugates: A Comprehensive Review.* **Puregmaa Khongorzul, Cai Jia Ling, Farhan Ullah Khan, Awais Ullah Ihsan, Juan Zhang.** s.l. : American Association for Cancer Research, 2019.

3. *Site-specific chelator-antibody conjugation for PET and SPECT imaging with radiometals.* **Mauricio Morais, Michelle T. Ma.** s.l. : Elsevier Ltd., 2018, Vol. 30, pp. 91-104.

4. *Fluorescent-labeled antibodies: Balancing functionality and degree of labeling.* **Shaleen Vira, Elena Mekhedov, Glen Humphrey, Paul S. Blank.** s.l. : Elsevier Inc., 2010, Anal. Biochem, Vol. 402, pp. 146–150.

5. *Assessment of near-infrared fluorophores to study the biodistribution and tumor targeting of an IL13 receptor a2 antibody by fluorescence molecular tomography.* **Parul Gupta, Jo-Ann Wentland, Mauricio Leal, Dangshe Ma, Rachel Roach, Antonio Esparza, Lindsay King, Mary E. Spilker, Cedo Bagi, Christopher T. Winkelmann and Anand Giddabasappa.** 34, 2017, Oncotarget, Vol. 8, pp. 57231-57245.

6. *68Ga chelating bioorthogonal tetrazine polymers for the multistep labeling of cancer biomarkers.* **Brandon Nichols, Zhengtao Qin, Jun Yang, David R. Vera and Neal K. Devaraj.** s.l. : The Royal Society of Chemistry, 2014, Chem. Commun, Vol. 50, pp. 5215--5217.

7. *Establishment of the In Vivo Efficacy of Pretargeted Radioimmunotherapy Utilizing Inverse Electron Demand Diels-Alder Click Chemistry.* **Jacob L. Houghton, Rosemery Membreno, Dalya Abdel-Atti, Kristen M. Cunanan, Sean Carlin,Wolfgang W. Scholz, Pat B. Zanzonico, Jason S. Lewis, and Brian M. Zeglis.** 1, s.l. : American Association for Cancer Research, 2017, Mol Cancer Ther, Vol. 16, p. 124.

8. *A bio-orthogonal functionalization strategy for site-specific coupling of antibodies on vesicle surfaces after self-assembly.* **Meiyu Gai, Johanna Simon, Ingo Lieberwirth, Volker Mailänder, Svenja Morsbach and Katharina Landfester.** s.l. : The Royal Society of Chemistry, 2020, Polym. Chem, Vol. 11, pp. 527–540.

9. *Enzyme-Mediated Methodology for the Site-Specific Radiolabeling of Antibodies Based on Catalyst-Free Click Chemistry.* **Brian M. Zeglis, Charles B. Davis, Robert Aggeler, Hee Chol Kang, Aimei Chen, Brian J. Agnew and Jason S. Lewis.** 2013 : 3 American Chemical Society, Bioconjugate Chem., Vol. 24, p. 1057−1067.

10. *Site-selective protein-modification chemistry for basic biology and drug development.* **Nikolaus Krall, Filipa P. da Cruz, Omar Boutureira and Gonçalo J. L. Bernardes.** s.l. : Macmillan Publishers Limited, 2016, NATURE CHEMISTRY, Vol. 8.

11. *Recent advances in the construction of antibody–drug conjugates.* **Vijay Chudasama, Antoine Maruani and Stephen Caddick.** s.l. : Macmillan Publishers Limited, 2016, NATURE CHEMISTRY, Vol. 8, pp. 114-119.

12. *Conjugation and radiolabeling of monoclonal antibodies with zirconium-89 for PET imaging using the bifunctional chelate p-isothiocyanatobenzyl-desferrioxamine.* **Maria J W D Vosjan, Lars R Perk, Gerard W**

M Visser, Marianne Budde, Paul Jurek, Garry E Kiefer & Guus A M S van Dongen. 4, s.l. : nature publishing group, 2010, nature protocols, Vol. 5, pp. 739-743.

13. *A practical guide to the construction of radiometallated bioconjugates for positron emission tomography.* **Lewis, Brian M. Zeglis and Jason S.** s.l. : The Royal Society of Chemistry, 2011, Dalton Trans, Vol. 40, pp. 6168–6195.

14. *Bioorthogonal chemistry amplifies nanoparticle binding and enhances the sensitivity of cell detection.* **Jered B. Haun, Neal K. Devaraj, Scott A. Hilderbrand, Hakho Lee and Ralph Weisslede.** s.l. : Macmillan Publishers Limited, 2010, NATURE NANOTECHNOLOGY, Vol. 5, p. 660.

15. *Impact of Drug Conjugation on Pharmacokinetics and Tissue Distribution of Anti-STEAP1 Antibody Drug Conjugates in Rats.* **C. A. Boswell, E. E. Mundo, C. Zhang, D. Bumbaca, N. R. Valle, K. R. Kozak, A. Fourie, J. Chuh, N. Koppada, O. Saad, H. Gill, B.-Q. Shen, B. Rubinfeld, J. Tibbitts, S. Kaur, F.-P. Theil, P. J. Fielder, L. A. Khawli and K. Lin.** s.l. : American Chemical Society, 2011, Bioconjugate Chemistry, Vol. 22, pp. 1994–2004.

16. *Monoclonal Antibodies: A Review.* **Surjit Singh, Nitish K. Tank, Pradeep Dwiwedi, Jaykaran Charan, Rimplejeet Kaur, Preeti Sidhu and Vinay K. Chugh.** s.l. : Bentham Science Publishers, 2018, Current Clinical Pharmacology, Vol. 13, pp. 85-99.

17. *Enhancing Reactivity for Bioorthogonal Pretargeting by Unmasking Antibody-Conjugated trans-Cyclooctenes.* **Maha K. Rahim, Rajesh Kota, and Jered B. Haun.** s.l. : American Chemical Society, 2015, Bioconjugate Chem, Vol. 26, p. 352−360.

18. *Analytical methods for physicochemical characterization of antibody drug conjugates.* **Aditya Wakankar, Yan Chen, Yatin Gokarn and Fredric S. Jacobson.** 2, s.l. : Landes Bioscience, 2011, mAbs, Vol. 3, pp. 161-172.

19. *Succinimidyl Ester Surface Chemistry: Implications of the Competition between Aminolysis and Hydrolysis on Covalent Protein Immobilization.* **China Y. Lim, Nicholas A. Owens, Ronald D. Wampler, Yixin Ying, Jennifer H. Granger, and Marc D. Porter.** s.l. : American Chemical Society, 2014, Langmuir, Vol. 30, p. 12868−12878.

20. *Conjugation of Antibodies with Bifunctional Chelating Agents: Isothiocyanate and Bromoacetamide Reagents, Methods of Analysis, and Subsequent Addition of Metal Ions.* **CLAUDE F. MEARES, MICHAEL J. MCCALL, DAYTON T. REARDAN, DAVID A. GOODWIN, CAROL I. DIAMANTI AND MAUREEN MCTIGUE.** s.l. : Academic Press, Inc., 1984, ANALYTICAL BIOCHEMISTRY, Vol. 142, pp. 68-78.

21. *Calicheamicin Derivatives Conjugated to Monoclonal Antibodies: Determination of Loading Values and Distributions by Infrared and UV Matrix-Assisted Laser Desorption/Ionization Mass Spectrometry and Electrospray Ionization Mass Spectrometry.* **Marshall M. Siegel, Keiko Tabei, Arthur Kunz, Irwin J. Hollander, Philip R. Hamann, and Duncan H. Bell.** 14, s.l. : American Chemical Society, 1997, Analytical Chemistry, Vol. 69, pp. 2716-2726.

Chapter 4: Pre-targeting gold nanoparticles

4.1 Introduction

This chapter describes the process towards the *in vivo* evaluation of pre-targeting in the application of boron neutron capture therapy (BNCT). As boron delivery agent, small spherical gold nanoparticles (AuNPs) were loaded with boron clusters and functionalized with tetrazine to enable the click reaction with a *trans*-cyclooctene (TCO) functionalized monoclonal antibody (mAb) for the pre-targeting approach. The process starts with the functionalization of a tumor targeting antibody and the subsequent evaluation of its bio-activity. Afterwards the boron delivery agent had to be synthesized, multifunctionalized and characterized for its physical properties as well as its bio-compatibility. After verifying that the two components, the mAb-TCO and the tetrazine-AuNPs are able to undergo the click reaction with each other, the pre-targeting strategy could be evaluated *in vitro* and *in vivo*.

4.1.1 The antibody

For this project a tumor targeting antibody was necessary. Trastuzumab is a well-known humanized antibody, approved by both the Food and Drug Administration (FDA) and the European Medicinal Agency (EMA), and has a high target specificity and binding affinity to human epidermal growth factor (HER2) receptors. Those receptors are overexpressed on the cell membrane of some breast and gastric tumors, and even though some HER2(+) tumor cell lines can build resistance against Trastuzumab as drug, the HER2 expression does not decrease (1). Furthermore, several articles are already published using Trastuzumab successfully as pre-targeting component (2; 3; 4). However, it is important to keep in mind that many mAbs, once bound to their target, tend to internalize (transfer into the cytoplasm). That property is known for Trastuzumab and may give issues in the pre-targeting strategy as the antibody needs to stay available on the cell membrane long enough for the second pre-targeting component (in this case the AuNPs) to reach the tumor and click to the antibody. Thus, the TCO functionalized Trastuzumab not only needs to be evaluated for its preserved binding affinity to HER2 but also for its behavior towards internalization (Figure 1).
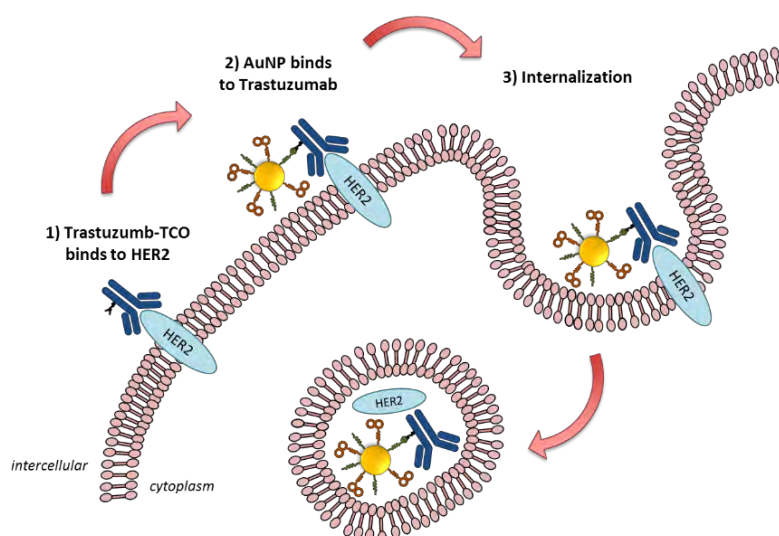

Figure 1: Illustration of the antibody's pathway in pre-targeting on cell level. The functionalized antibody (Trastuzumab-TCO) needs to be evaluated for its binding affinity to its target (HER2) as well as for its behavior towards internalization.

4.1.2 Small AuNPs as boron delivery agents

AuNPs are very versatile; they can vary in chemical and physical properties as well as in shape and size. The increase of popularity over the last decade is also due to their ability of a high surface loading, low toxicity, their optical properties and rather easy modifications of their chemical properties by surface functionalization. After the evaluation and biodistribution studies of different sized and shaped AuNPs, previously conducted in our group (11) (and ongoing PhD of Krishna Reddy Pulagam), we chose small (core size 3-5 nm), spherical particles. The biodistribution of smaller particles shows an increased accumulation and penetration into tumor tissue through the EPR effect and a shift of the elimination can be observed towards smaller particles from liver and spleen to kidneys and bladder which means faster clearance (5). Their high surface area-to-volume ratio allows a high amount of cargo, such as PEG to stabilize the particles and increase their bio-compatibility next to a high loading of the boron cluster COSAN (Cobalt *bis*[dicarbollide], Figure 2, right) to enable the delivery of a sufficient amount of Boron-10 into tumor tissue for the application in BNCT. Finally, functionalization with a tetrazine moiety was necessary to enable pre-targeting (Figure 2, left).
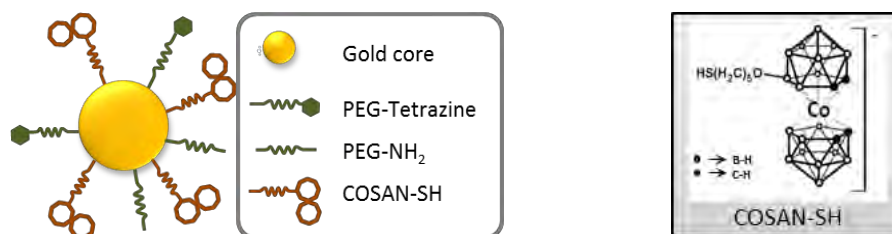
Figure 2: Left: Schematic figure of a small, spherical AuNP, stabilized with PEG and functionalized with tetrazine and COSAN, right: the structural details of the boron cluster COSAN.

4.1.3 Internalization of nanomaterials

Internalization plays a key role in this work. The TCO-conjugated antibody may not internalize too fast to stay available on the cell membrane for the AuNP (the second component of the pre-targeting strategy) to attach. On the other hand, a subsequent internalization of the mAb-AuNP complex would be appreciated as the efficacy and selectivity increases for BNCT agents in case of localization in the cytoplasm, closer to the cell nucleus.

The internalization of nanomaterial depends on many cofactors, such as particle size and shape, charge and surface properties as well as the type of cell line. For example, positively charged particles have increased nonspecific internalization, whereas negatively charged have longer blood circulation time. The main mechanism for cell uptake is the endocytic pathway, forming endosomes which convert from early (characterized by lower pH of around 6-6.5) to late endosomes and finally into lysosome (Figure 3) (5). The aggressive endosomal or lysosomal environment (low pH and hydrolytic enzymes) leads to degradation and subsequently to the release of nutrients and particle fractions whereas receptors and other cellular structures are recycled to the cell membrane. In tumor cells higher such activity can be observed (6).
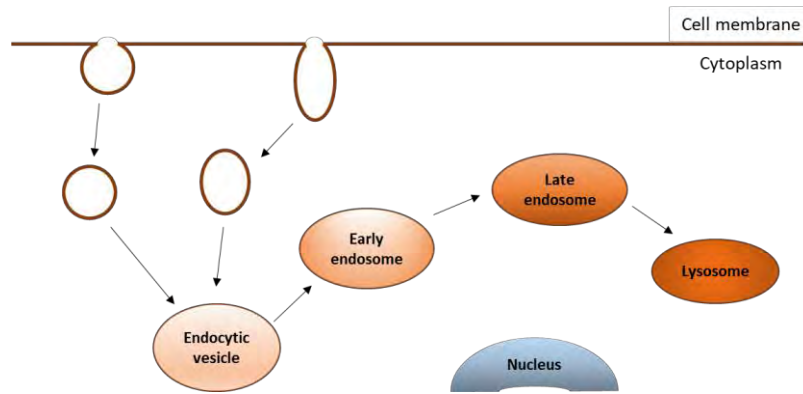
Figure 3: Schematic representation of the endocytic pathway.

Endocytosis can be further classified in different subsections. The most important ones are clathrin-mediated, caveolae-mediated and clathrin/caveolae-independent endocytosis (Figure 4). The majority of receptor-mediated internalization of nanoparticles occurs through the clathrin-mediated endocytosis. The caveolae-mediated endocytosis on the other hand is found in a variety of cellular processes such as cholesterol homeostasis, signal transduction and the endocytosis of proteins forming flask-shaped infoldings (60-80 nm), so called caveolae, which then convert into caveosomes. The major difference to endosomes is their neutral pH, resulting in lower aggressiveness. Also, negative surface charges have been found to induce cell uptake predominantly via caveolae (6). Furthermore, it is shown that the caveolin-1 protein is involved in the receptor endocytosis of HER2, which is localized in caveolae and target for Trastuzumab. Hence, HER2 degradation occurs through the caveolae-mediated endocytosis (7).
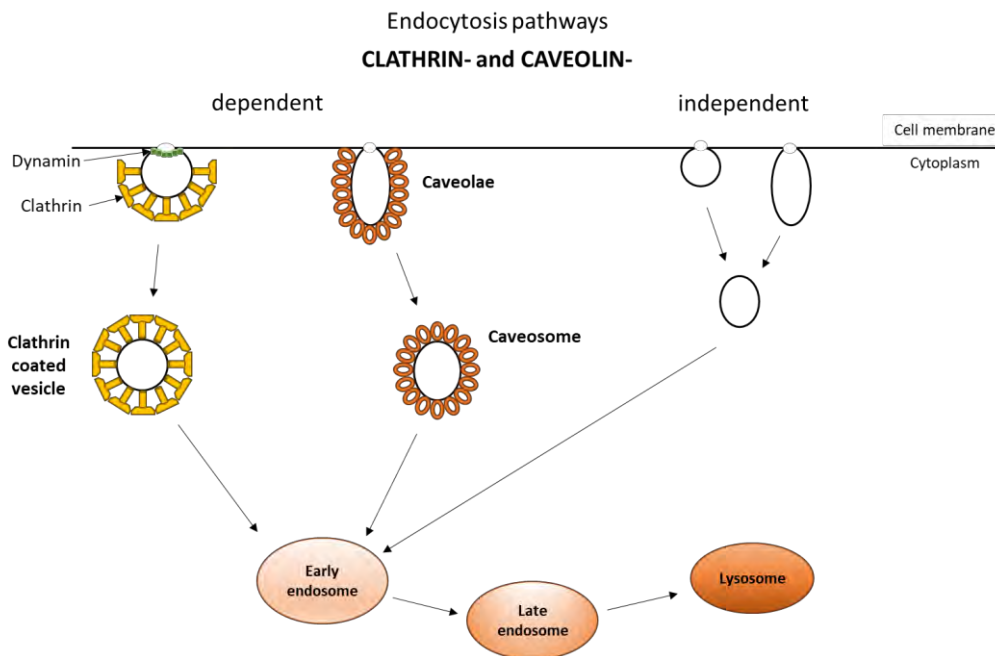
Figure 4: Illustration of internalization pathways, such as clathrin- and caveolin-dependent and independent endocytosis.

4.2 Objectives

The specific objectives of this work were:

1. To establish a BT-474 breast cancer xenograft mouse model.
2. To functionalize the mAb Trastuzumab with TCO.
3. To evaluate cell binding capacity, *in vivo* biodistribution and its internalization (both *in vitro* and *in vivo*) of Trastuzumab-TCO.
4. To synthesize, characterize and radiolabel AuNPs functionalized with boron-rich molecules and tetrazine moieties.
5. To evaluate the pre-targeting strategy for AuNPs (*in vitro* and *in vivo*).

4.3 Results and discussion

4.3.1 Establishment of a BT-474 cancer xenograft mouse model

In order to evaluate the behaviour of the conjugated mAb, the functionalized AuNP and the approach of pre-targeting *in vivo*, a mouse model with human cancer xenografts had to be generated. Using the antibody Trastuzumab focused the choice to HER2 overexpressed tumors. We established a breast cancer mouse model with the BT-474 cell line on female NOD.CB17-Prkdcscid/J mice. With that aim, 5-6 weeks old mice were operated to implant a 17β-estradiol pellet subcutaneously at their neck, needed to enable the tumor to grow. 24 hours after pellet implantation, $10x10^6$ BT-474 tumor cells per animal (in sterile PBS:Matrigel 1:1) were subcutaneously inoculated at the flank of the mouse. Prior to each inoculation a Lonza Mycoplasma test was carried out to ensure that the cells weren't contaminated. The sizes of the tumors were measured every 2-3 days with a digital caliper and volumes calculated ($V = \frac{\text{short diameter}^2 * \text{long diameter}}{2}$). At the time the tumour reached 200-300 mm³ (around 2 weeks after inoculation, Figure 5) *in vivo* studies could be performed. The defined human endpoints were: (i) weight loss greater than 20 % in one week, (ii) one or more of the following clinical signs: abdominal distension, dyspnoea, cachexia or stooping, (iii) the absence of response to stimuli and lethargy, (iv) a tumor larger than 1500 mm³ in volume and (v) ulcerated or necrotic tumors or wounds / aggressions severe infected.
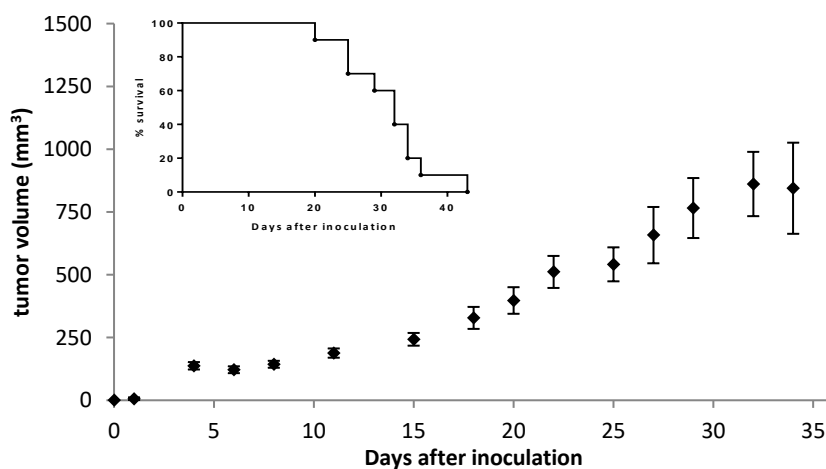

Figure 5: Graphical representation of tumor growth of BT-474 breast cancer xenografts on NOD/SCID mice (values are expressed as mean ± standard error mean, n = 10). Inset: percentage of survival.

4.3.2 Functionalization of Trastuzumab with TCO

For the pre-targeting stratgey the antibody Trastuzumab needed to be functionalized with a TCO ligand to enable the *in vivo* click reaction to a tetrazine component. Therefore the commercial available TCO-NHS was used and randomly conjugated to freely available amines of lysine residues in the antibody (Figure 6).
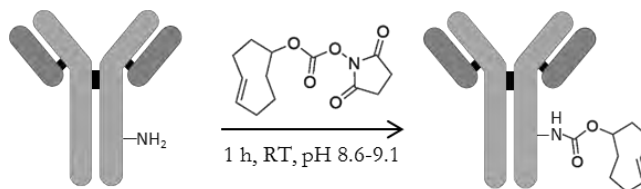

Figure 6: Illustration of the TCO-NHS conjugation to Trastuzumab.

TCO-NHS was used in 50-55 eq. excess to the antibody and incubated for 60 min at room temperature with a pH between 8.6 and 9.1 and a mAb concentration of 3 mg/mL (see 4.5 Experimental part for details). Those conditions led to an average conjugate of about two TCO per mAb (the determination of achieved TCO moieties per antibody is explained in details in Chapter 3 of this thesis).

4.3.3 Evaluation of Trastuzumab-TCO by cell binding assays

To ensure that the modification of the antibody by TCO conjugation did not compromise its binding ability to the target, binding assays were perfomed. Breast cancer cells (BT-474 cell line) were used as target which overexpress the cell membrane receptor HER2. One way to determine the binding is a radiometric method using an assay developed by Lindmo in 1984 (9). The modified and radiolabelled mAb is incubated with cell suspensions in different concentrations.

To radioabel the mAb-TCO, conjugation with a DFO-chelator (*p*-NCS-Bz-DFO) was required (Figure 7). The dual conjugation was done in a one pot synthesis at 37 °C for 45 min. After purification the antibody was radiolabeled by incubating with ^{89}Zr-oxalate at room temperature for one hour, followed by purification with a sephadex size exclusion column into PBS. The labeling was monitored by radio-TLC (radio thin-layer chromatography) using iTLC-SG chromatography paper (Agilent Technologies) and 20 mM citric acid + 60 mM EDTA/acetonitrile solution (9/1 v/v) as the stationary and mobile phases, respectively (Figure 8, for details see 4.5 Experimental part). After incubation unbound antibody was removed and the immunoreactive fraction plotted (Figure 9). The assay demonstrates that the modified mAb was not significantly compromised with preserved binding yields up to 90 %.
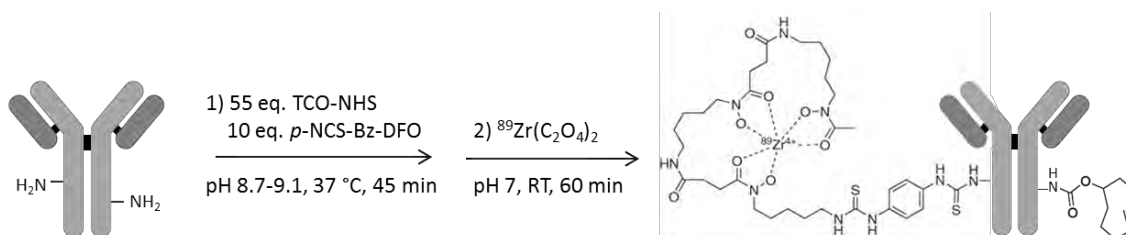

Figure 7: Schematic representation of TCO- and DFO-conjugation followed by ^{89}Zr-radiolabeling to obtain TCO-Trastuzumab-DFO-^{89}Zr.
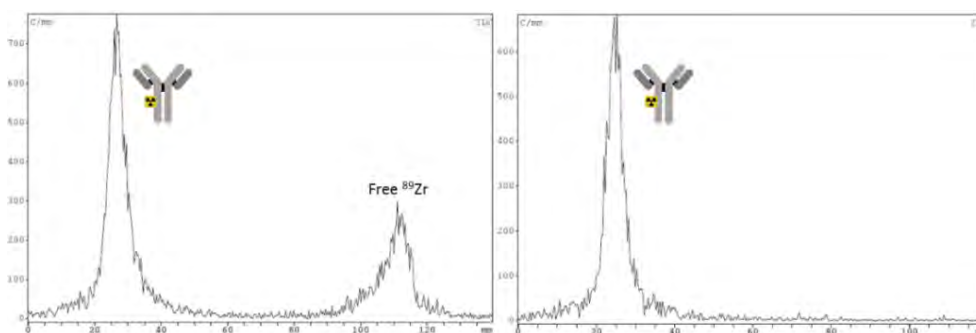
Figure 8: Chromatograms of radio-TLCs monitoring the radiolabeling of Trastuzumab with ^{89}Zr. Left: reaction mixture (72 % labeled), right: after purification with size exclusion column.
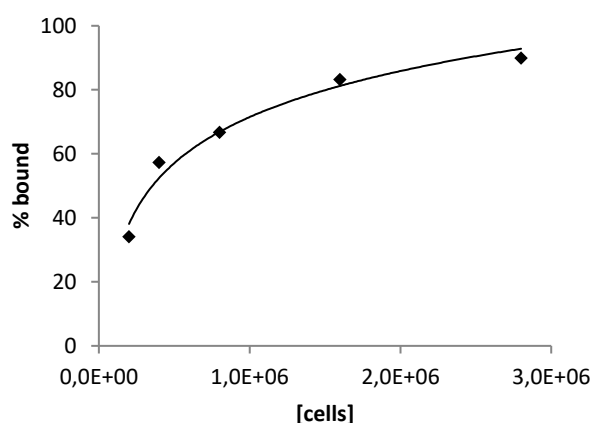

Figure 9: Lindmo cell binding plot of [^{89}Zr]-Trastuzumab on BT-474 cells.

To confirm the obtained results by the Lindmo assay, flow cytometry based on fluorescence-activated cell sorting (FACS) was performed. Therefore the TCO conjugated Trastuzumab was fluorophore-labelled with mTzCy3 (6-Methyl-Tetrazine-Sulfo-Cy3) via the inverse-electron-demand Diels Alder click reaction between TCO and tetrazine. The studies were first performed with different concentrations of mAb (0.01 - 0.1 mg/mL) during 30 min incubation (Figure 10 C) followed by a study with different incubation time points (5 – 30 min), using the concentration that showed the best labeling results (Figure 10 D). The experiments showed that with a concentration of 0.1 mg/mL and an incubation time of only 5 min over 80 % of the cells were labeled with Trastuzumab-TCO-mTzCy3. These results confirm that there is no significant decrease in the binding affinity of the modified mAb towards it's target.
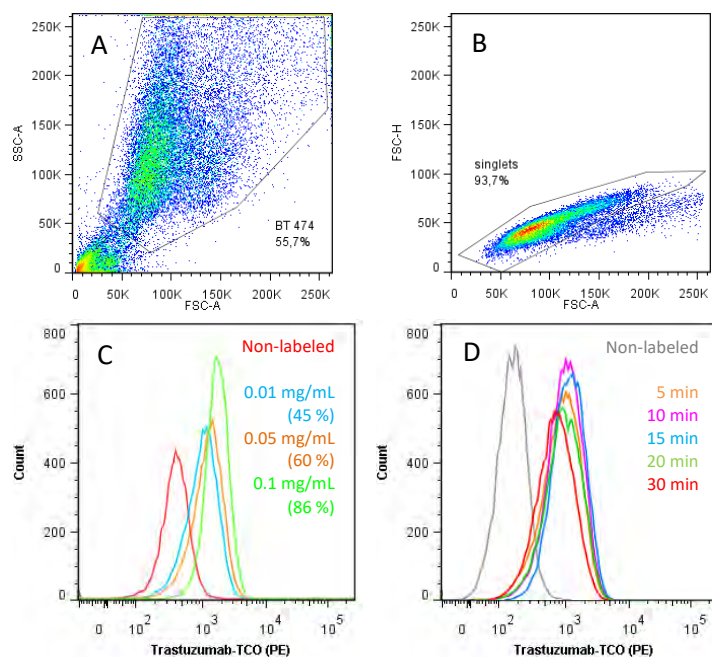
Figure 10: FACS studies, to monitor cell binding capability of TCO conjugated Trastuzumab; A) and B) density dot plots: A) gating for live, non-labeled BT-474 cells, B) gating for singlets allowing discrimination of doublets; C) and D) histogram of fluorescent BT-474 population with control (non-labeled): C) different concentrations of Trastuzumab (30 min incubation), D) different incubation times of Trastuzumab (0.1 mg/mL).

4.3.4 Evaluation of Trastuzumab-TCO by biodistribution studies

After illustrating that the binding capacity of the TCO conjugated Trastuzumab is preserved, biodistribution studies in BT-474 breast cancer xenograft mice were perfomed. On one hand to proof tumor uptake *in vivo*, but also to determine the time point for the injection of the second component of the pre-targeting approach. To do so, the time when the mAb concentration in tumor is high, but low in blood and other tissue, needed to be found (Figure 11).
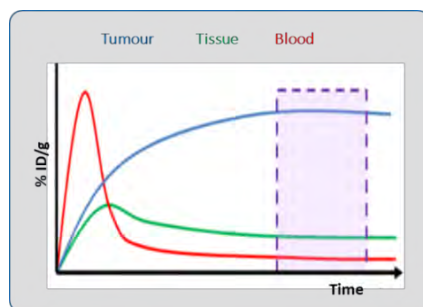

Figure 11: Fictitious time activity curves representing the concentration of drug in the tumor (blue line), blood (red line) and healthy tissue (green line) after intravenous administration. The time window in which the concentration in the tumor is high and the concentrations in blood and healthy tissue are low is shown.

In order to perform trackable *in vivo* studies Trastuzumab was, as above, not only conjugated with TCO but also radiolabeled with ^{89}Zr. Doses of about 100 μg TCO-Trastuzumab-DFO-^{89}Zr were injected intravenously into breast cancer xenograft bearing mice (n = 3). PET-CT scans were performed approximately 1 h, 8 h, 24 h, 48 h and 72 h post-injection using an eXplore Vista-CT small animal PET-CT system (GE Healthcare, USA) system (Figure 12).
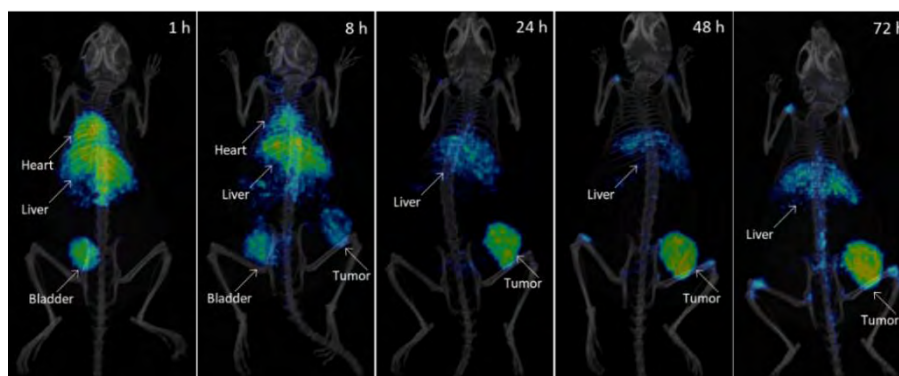
57

Figure 12: Representative coronal PET images (maximum intensity projections) obtained at different time points after intravenous administration of [89Zr]-DFO-Trastuzumab-TCO. PET images have been co-registered with CT images (maximum intensity projections) for localization of the radioactive signal. Positions of the heart, liver, bladder and tumor are indicated.
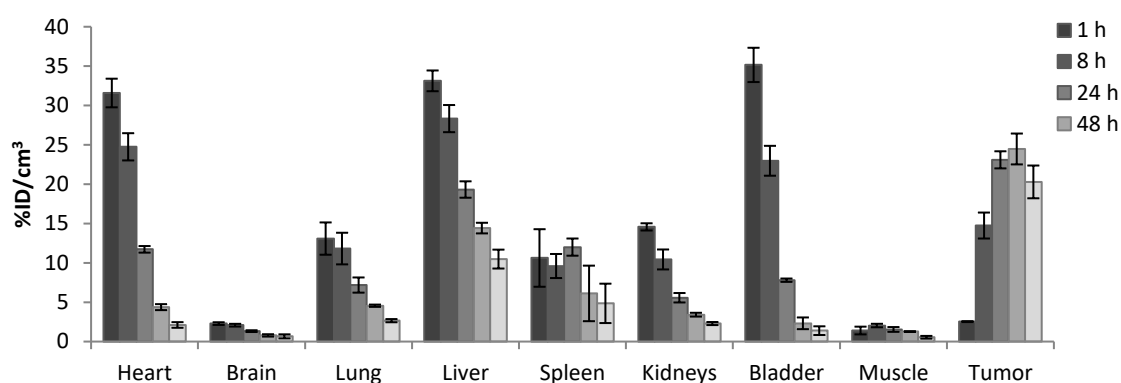

Figure 13: PET quantification of organ/tissue uptake at 1 h, 8 h, 24 h, 48 h and 72 h post-injection (values are expressed as mean ± standard error mean, n = 3) to represent the biodistribution of [89Zr]-DFO-Trastuzumab-TCO.

The PET images, confirmed by PET quantification (Figure 13), show increasing tumor uptake with its maximum at 48 h (24.5 % ID/cm^3). If after 8 h there is still high uptake in organs like heart and liver, at 24 h post-injection the background signal is drastically reduced and the tumor is clearly visible. At later time points, typical for ^{89}Zr images, using DFO as chelator, the bones, like knees, shoulder and backbone, show uptake of ^{89}Zr due to impaired stability of the radio-complex *in vivo* (10). The results were confirmed by *ex vivo* experiments after the last PET scan at 72 h post injection, extracting the organs and analysing via gamma counter (Wallach Wizard, PerkinElmer) (Figure 14).
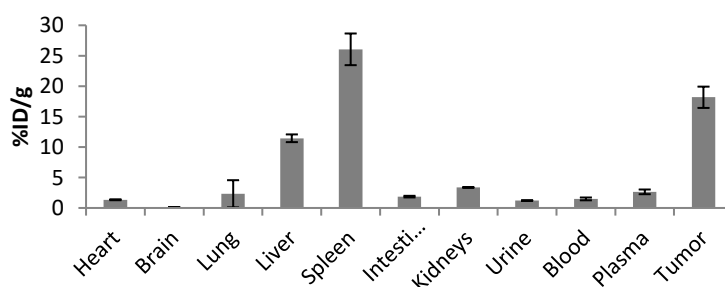

Figure 14: Concentration of radioactivity in different organs/tissues, as determined by gamma counting, at t = 72 hours after administration of [89Zr]-DFO-Trastuzumab-TCO (values are expressed as mean ± standard error mean, n = 3).

4.3.5 Trastuzumab-TCO internalization studies *in vitro* and *ex vivo*

For the pre-targeting strategy the first injected TCO-functionalized mAb needs to stay available long enough, that is, on the cell membrane, for the second injection, the tetrazine functionalized component, to reach the tumor and "click" to the antibody. However, many mAbs, once bound to their target, tend to internalize from the cell membrane into the cell cytoplasm. Hence, to obtain insight of the behaviour of Trastuzumab, internalization studies were performed. First, *in vitro* monitoring of TCO-Trastuzumab fluorophore-labeled with mTzCy3 (6-Methyl-Tetrazine-Sulfo-Cy3) via the click reaction to TCO was carried out using BT-474 cells and fluorescence microscopy (Figure 15). Images were acquired using a confocal microscope (Zeiss LSM 880) and analyzed by the ZEN-ZEISS software.
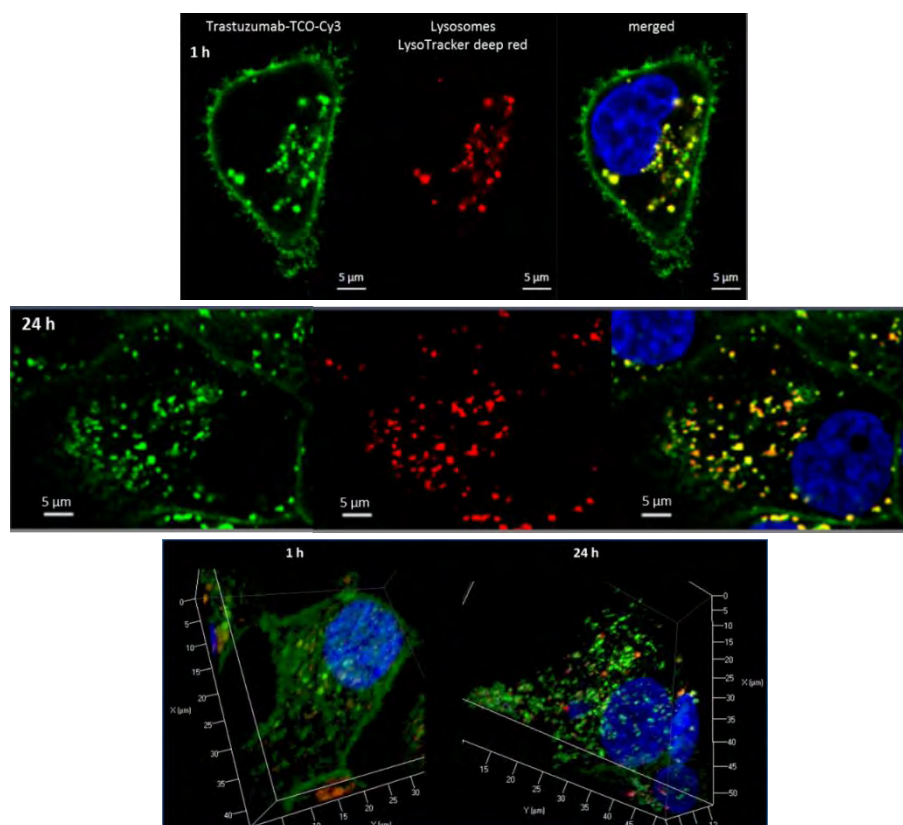

Figure 15: Representative images by confocal fluorescence microscopy of BT-474 cells incubated with Trastuzumab-TCO-Cy3 (green) over time. Nucleus stained with Hoechst33342 (blue), lysosomes with Lysotracker-deep-red (red). Merged signal of mAb and lysosome in yellow. Top and middle: Image taken after 1 h and 24 h incubation time. Bottom: 3D images (Z-stack) after 1 h and 24 h incuabtion time.

Looking at early time points, the cell membrane is clearly visible, revealing that Trastuzumab bound to the HER2 cell membrane receptors. However, after one hour incubation at 37 °C some Cy3 fluorescence is already found in the cytoplasm. It correlates with the red stained lysosomes (yellow signal in the merged image) leading to the conclusion that a fraction of Trastuzumab-HER2 complexes already internalized. Still, compared to the 24 h incubation time point a huge difference can be seen. Over time most mAb internalized resulting in an image with spread Cy3 signal over the cytoplasm, correlating with the Lysotracker-deep-red signal. The cell membrane is hardly detectable anymore.

Yet, the goal is the evaluation of the pre-targeting strategy *in vivo*. The antibody, other than *in vitro*, first needs to reach the tumor and attach to the membrane before internalization can occur. Hence, to find the right time point for the injection of the second pre-targeting component internalization studies with radiolabeled Trastuzumab were performed *in vivo*. To do so, we took advantage of the possibility of using two different labeling strategies, either using ^{89}Zr- or ^{131}I. After internalizing into the cell plasma, Iodine is cleaved off and released from the cell, whereas Zirconium remains there. Hence, for the experiment, one batch of Trastuzumab was conjugated with *p*-NCS-Bz-DFO and, after purification, radiolabeled by incubation with ^{89}Zr$(C_2O_4)_2$ as described above. Another batch of Trastuzumab was radiolabeled with ^{131}I ($t_{1/2}$ = 8.02 days, beta minus decay) using the Iodogen-coated method. In brief, a vial was coated with Iodogen, a solution of Trastuzumab in sodium phosphate buffer added and incubated for 4 min with [^{131}I]NaI (for radiolabeling details see 4.5 Experimental part). After purification by sephadex G-25 size exclusion column (PD10® GE Healthcare) the different labeled Trastuzumab (^{131}I and ^{89}Zr) were mixed in a 1:1 ratio of their activity (Figure 16, left). Four mice were injected intravenously and *ex vivo* studies were executed 24 h (n = 2) and 48 h (n = 2) post injection. The activity of the extracted tumors was measured in a gamma counter (Wallach Wizard, PerkinElmer). As the gamma spectra of the two nuclides are varying enough (represented with a high resolution gamma spectrum in Figure 16, right) signal separation can be achieved. Hence the respective tumor uptake of radiolabeled antibody from each species can be obtained (Figure 17).
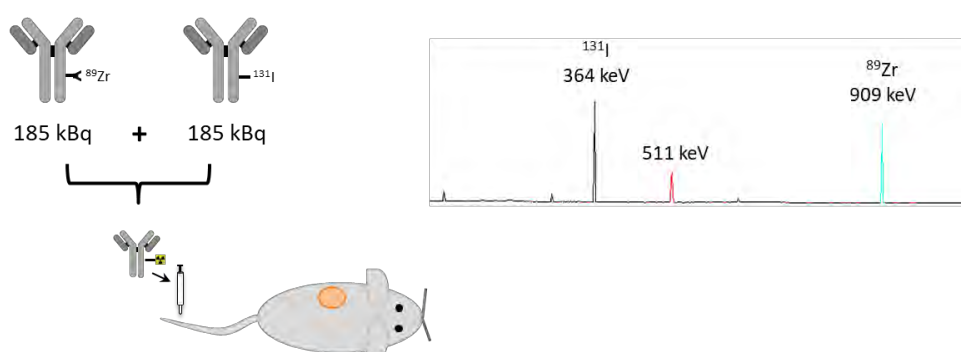

Figure 16: Left: Illustration of *ex vivo* internalizing studies. A 1:1 mix of mAb, labeled with either Iodine-131 or Zirconium-89, is injected intravenously to a mouse. After defined time points *ex vivo* studies were performed and tumor uptake measured via gamma counter. Right: gamma spectra of the mixed radionuclides ^{131}I and ^{89}Zr.
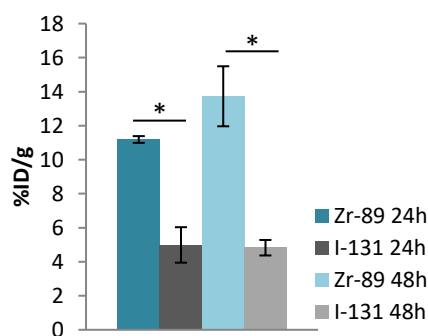

Figure 17: Tumor uptake determined by gamma counting after *ex vivo* studies at 24 h and 48 h after administration of ^{89}Zr-labeled (blue) and ^{131}I-labeled (grey) mAb to evaluate the internalization of Trastuzumab *in vivo* (values are expressed as mean ± standard deviation, n = 2).

The determined uptake of Trastuzumab in tumor is significantly different if determined with Iodine-131 or Zirconium-89. [89Zr]Trastuzumab reaches 11.2 and 13.7 %ID/g respectively at 24 h and 48 h post injection. [131I]Trastuzumab instead shows only uptake of 5.0 and 4.8 %ID/g, decreasing in-between the time points (Figure 17). This outcome does not only confirm the internalization of Trastuzumab but also the increase of internalized fraction over time. By setting the uptake of [89Zr]Trastuzumab as 100 % and the uptake of [131I]Trastuzumab as the fraction which is not yet internalized (that is 131I not cleaved off and released from the cell) the percentage of internalized fraction increases from 55 % at 24 h to 65 % at 48 h post-injection. This calculation naturally is only estimation, as, among others, we don't take into account the time needed after internalization for cleavage and release of 131I from the cell; however, it gives insight of the internalization rate of Trastuzumab. Importantly, it also confirms that a fraction of the antibody remains on the cell membrane and hence pre-targeting is viable.

Looking at the two experiments, the biodistribution (Figure 13) and internalization of Trastuzumab (Figure 15 and Figure 17), the time point for the injection of the second component in the pre-targeting strategy was set to 24 h after the mAb injection, balancing between tumor uptake, sufficient clearance from blood and healthy tissue and internalization of the antibody.

With the completed evaluation of TCO conjugated Trastuzumab we moved to the second component of the pre-targeting approach, the boron delivery agent. Therefore, we synthesized and characterized heavily boronated gold nanoparticles (AuNPs), functionalized with a tetrazine derivative as counterpart for the *in vivo* click reaction with TCO of the mAb.

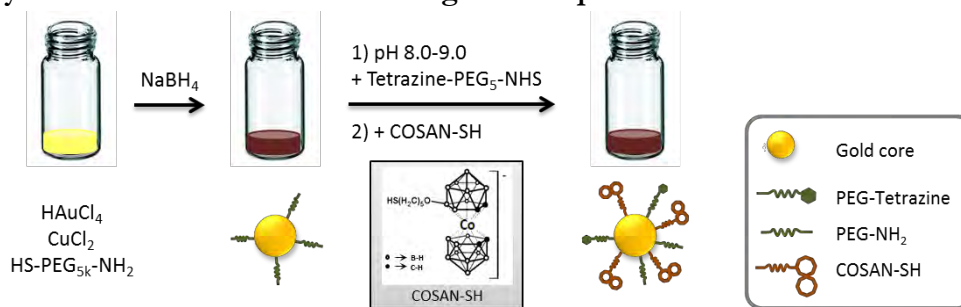### 4.3.6 Synthesis and characterization of gold nanoparticles

Figure 18: Schematic representation of synthesis and functionalization of AuNPs.

After the evaluation and biodistribution studies of different sized and shaped AuNPs, previously conducted in our group (11) (and ongoing PhD of Krishna Reddy Pulagam), the particles chosen for the pre-targeting approach were small (core size 3-5 nm), spherical particles, synthesized in aqueous medium (12). For the final experiment, the *in vivo* studies of pre-targeted AuNPs, radiolabeled particles were required. The approach was to synthesize copper-64 ($t_{1/2}$ = 12.7 h) alloyed particles to obtain core labeled AuNPs, hence, for the characterization of the AuNPs copper alloyed particles were synthesized (Figure 18). Therefore, a solution of Chloroauric acid (HAuCl$_4$) and CuCl$_2$ in water was reduced with sodium borohydride (NaBH$_4$) and stabilized with thiolated amino-polyethylene glycol (HS-PEG$_{5000}$-NH$_2$). A color change could be observed during the addition of NaBH$_4$ from the

light yellow of HAuCl$_4$ to a dark red, typical for AuNPs. After the particle settled for 2 h at room temperature, purification was performed by spin filtration (30 kDa) with PBS washings. To functionalize the particles with tetrazine for the pre-targeting approach, a NHS ester of such was used able to bind to free amine groups of the PEG-amine. Therefore, the pH of the AuNP suspension was adjusted to 8-9 with 0.1 M NaOH and Tetetrazine-PEG$_5$-NHS added. After 1 h incubation at room temperature the particles were purified by spin filtration and the last step launched. To functionalize in the matter of BNCT with high Boron-10 loadings, COSAN, a boron cluster, was attached. Therefore, COSAN was previously thiolated at the position of a BH group, which has a high electron density and can easily be functionalized. COSAN was reacted with tetrahydropyran to form intermediate [1], followed by ring opening with potassium thioacetate into intermediate [2]. To obtain the final compound, COSAN-SH, basic hydrolysis with sodium methoxide (NaOMe) was performed (Figure 19) (11). The coupling of such to the gold core of the AuNPs via thiol linkage occurred during one hour incubation at room temperature. Spin filtration was executed for purification, the AuNPs recovered in PBS and analyzed for their UV-VIS absorbance, shape, size, charge and composition.
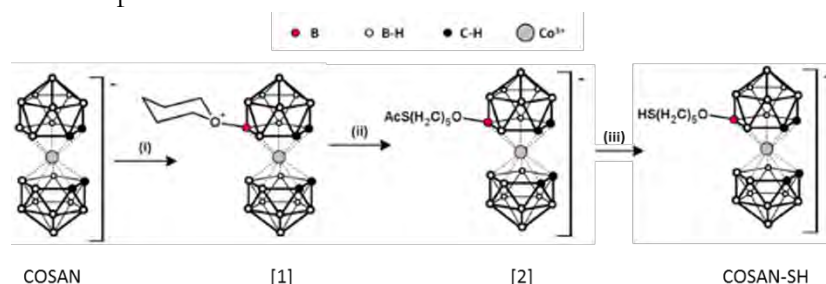

Figure 19: Synthesis of functionalized COSAN-SH; (i) Tetrahydropyran, dimethylsulphate, H$_2$SO$_4$; (ii) Potassium thioacetate; (iii) NaOMe, MeOH.

UV-Vis absorbance is an easy and fast method and can be used to monitor each step of the synthesis and functionalization of the particles. If the core of the AuNPs is formed correctly the typical plasmon, dependent on shape and size of AuNPs, will be visible. For the particles in hand the light absorbance by the plasmon is not very intense, this is due to their small size, but still clearly visible between 430 and 630 nm. The functionalization steps can be monitored due to the maximum absorbance of tetrazine at around 270 nm, and of COSAN at around 315 nm (Figure 20).
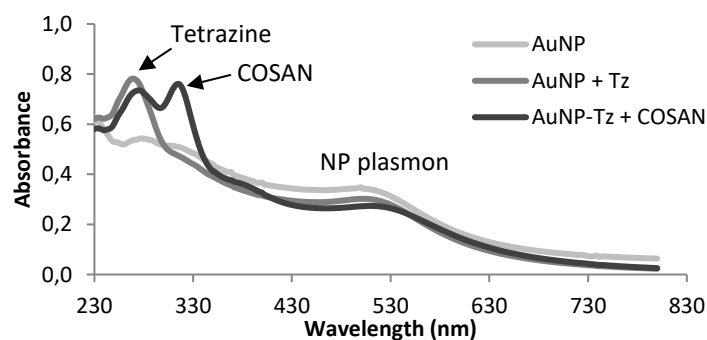

Figure 20: UV-VIS spectra of the PEG-amine stabilized AuNP core (light grey), functionalized with tetrazine (dark grey, max absorbance at 270 nm) and functionalized with tetrazine and COSAN (black, max absorbance at 315 nm).

Another analysis method to see if the synthesis and functionalization of the AuNPs was successful is by transmission electron microscopy (TEM). An image of the non-functionalized particles shows the shape and size, as well as if the distribution is homogeneous. Furthermore, using a negative staining on the functionalized particles confirms the presence of the organic layer (due to COSAN and PEG_5-Tetrazine) around the cold core in bright grey (Figure 21).
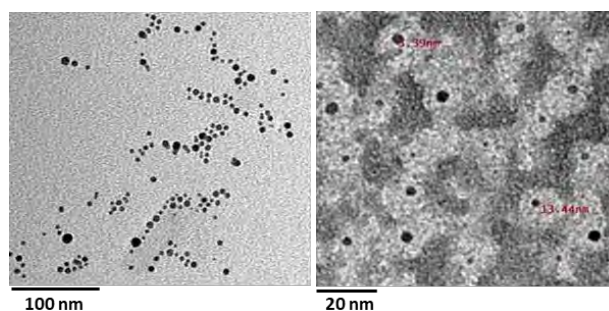

100 nm   20 nm

Figure 21: Representative TEM images to visualize shape and size of AuNPs; Left: PEG-amine stabilized AuNP, right: tetrazine- and COSAN-functionalized AuNP (with negative staining), showing in bright grey an organic layer around the metal core.

The TEM analysis showed a rather homogeneous distribution of spherical particles with a core diameter of 3-5 nm and an increase of the particle size due to the functionalization to 12-15 nm.

To determine the hydrodynamic diameter of the particles dynamic light scattering (DLS) was performed (Figure 22). It describes the size distribution by volume and showed a clear difference between the non-functionalized particles and the COSAN- and tetrazine-functionalized ones. The size increased from 27.27 ± 3.99 d.nm to 39.61 ± 0.74 d.nm.
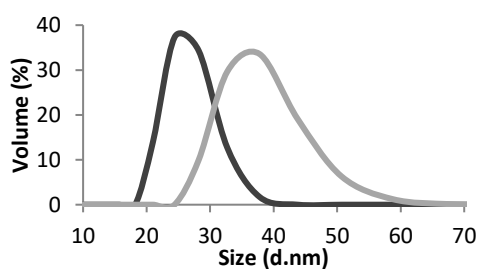

Figure 22: Size distribution ranges as determined by DLS (volume distribution) for small, spherical AuNP; Black: non-functionalized, PEG-amine stabilized AuNPs, grey: tetrazine- and COSAN-functionalized AuNPs.

The particles are stabilized with PEG-amine, leaving free amine groups on the surface of the AuNPs. Measuring the zeta potential (ζ-potential) leads therefore to a positive value (7.87 ± 9.36 mV). However, after coupling tetrazine, which reduces the amount of free amine groups, and after attaching COSAN, a single negatively charged molecule, brings the zeta potential of the functionalized AuNPs to a negative value (-33.60 ± 3.82 mV) (Figure 23).
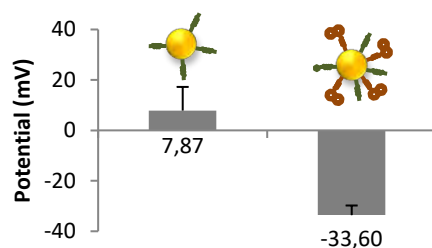
Figure 23: Zeta-potential values measured for non-functionalized, PEG-amine stabilized and tetrazine- and COSAN-functionalized AuNPs.

Finally, the composition of the AuNPs was investigated by ICP-MS analysis (Inductively Coupled Plasma Mass Spectrometry), determining the concentrations of gold, boron and cobalt. In order to assure that stable COSAN is present on the surface of the particles, a molar ratio of boron to cobalt of 18:1 should be determined (see schematic structure of COSAN in Figure 24). With an obtained ratio of 18.2 the stability of COSAN attached to the AuNPs was confirmed. Furthermore, the boron loading of the particles was identified by determining the amount of boron to be 195 µg per mg gold, showing high boron loadings of the particles.
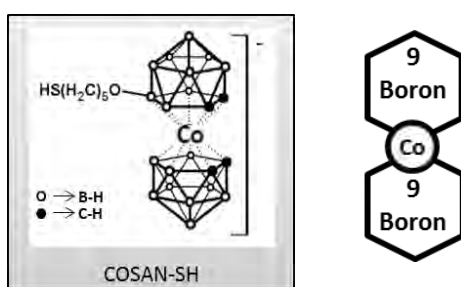

Figure 24: Schematic structures of COSAN, showing the ratio of boron to cobalt with 18:1.

To evaluate bio-compatibility of the multifunctionalized AuNPs, cytotoxicity studies on BT-474 breast cancer cells were performed. The cells were treated with 5, 10, 20, 60, 80 and 120 µM (gold concentration) of AuNPs for up to 72 h. Analysis by standard MTT assay showed, with overall cell survivals over 90 %, no induced cell death due to the particles in BT-474 cells, indicating negligible cytotoxicity (Figure 25).
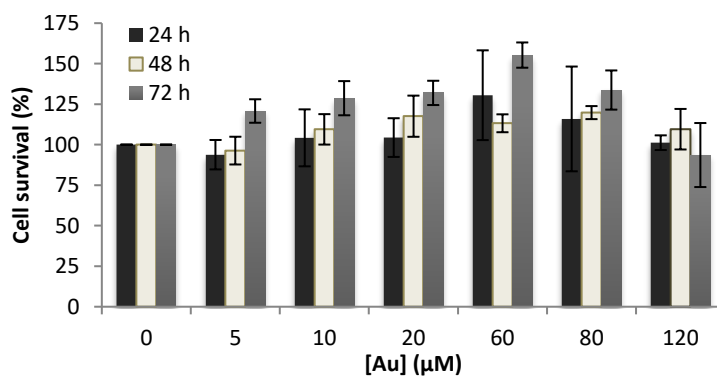

Figure 25: Cell viability in the presence of multifunctionalized AuNPs for 24 h, 48 h and 72 h on BT-474 breast cancer cell line; cells were incubated with increasing concentrations of AuNPs and cell viability was determined by MTT assay (values are expressed as mean ± standard error mean, n = 6).

For further studies on the BT-474 cell population fluorescence microscope experiments were performed. For most drug delivery agents in cancer therapy the ideal situation is internalization of such into the cancer cell cytoplasm before releasing the drug. It leads to higher efficacy and selectivity. This also includes the case of BNCT and its boron delivery agents. The neutron capture and the subsequent release of alpha particles and lithium ions has highest efficacy with boron close to the cell nucleus, due to the short path length of the emitted particles. In the case of pre-targeting the ideal situation would be for the AuNPs (the boron delivery agent) to "click" to the mAb, followed by internalization of the mAb-AuNP complex. To evaluate the internalization of the multifunctionalized AuNPs as such, a fluorophore-label was attached with TCO-Cy3, undergoing the click reaction with tetrazine and incubated overnight with BT-474 cells. To visualize co-localization between the AuNPs and the lysosomes, the location where internalized particles will be found, the lysosomes were stained with Lysotracker-deep-red. Images were taken using a live cell Axio Observer fluorescence microscope (Zeiss) and analyzed by the ZEN-ZEISS software, showing a clear co-localization between the AuNPs and the Lysosomes and therefore internalization of such after overnight incubation (Figure 26). As mentioned, cell uptake is a desired property for boron delivery agents, as for the pre-targeting strategy a co-internalization of the antibody-AuNP complex is favored. Yet, it can be expected, that the click reaction between the mAb and the AuNP is faster than the cell uptake of the particles alone, hence no restrictions were expected for pre-targeting due to the ability of the particles to internalize. Additionally, the internalization of the AuNPs without interacting with the antibody should neither result in decreased efficacy, and can be considered as a parallel uptake mechanism that contributes to accumulation of the boron atoms in the interior of the cells.
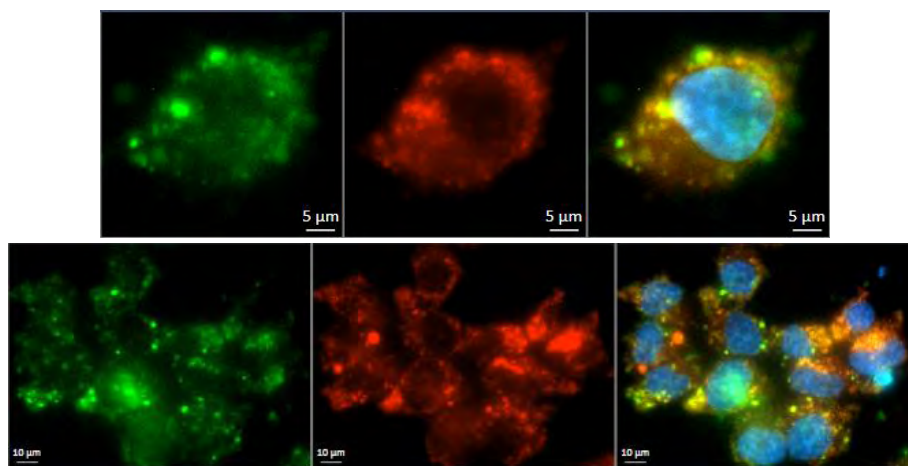

Figure 26: Representative images by live cell fluorescence microscopy of multifunctionalized AuNPs after overnight incubation. In green: AuNPs, fluorophore-labeled with TCO-Cy3, in red: Lysosomes, stained with Lysotracker-deep-red, in blue: nucleus, stained with Hoechst33342. Merged signals of AuNPs colocalizing with lysosomes appear in yellow.

After the successful synthesis and functionalization of the AuNPs, including a complete characterization and with confirmed bio-compatibility, we could move to the evaluation of pre-targeting. To do so, at first, proof was needed for the click reaction to occur between the TCO functionalized Trastuzumab and the tetrazine functionalized AuNPs. Therefore, an agarose gel electrophoresis with a mixture of the two pre-targeting components and

respective controls was executed. The AuNPs derivatives were visible on the gel due to their red color. To visualize the mAb species after the electrophoresis a staining of the gel with coomassie blue was performed. As control each component was applied sole to the gel (Figure 27, line 1+2: Trastuzumab without and with TCO, line 6+7: AuNPs with and without tetrazine). Furthermore, a mix between either non-functionalized Trastuzumab and multifunctionalized AuNPs (Figure 27, line 3) or functionalized Trastuzumab and AuNPs without tetrazine functionalization (Figure 27, line 5) was applied; separations could be obtained. When applying the mixture of Trastuzumab-TCO and fully functionalized AuNPs (Figure 27, line 4) a merged signal appears showing combined signal of red AuNPs and blue antibody, confirming that the click reaction took place.
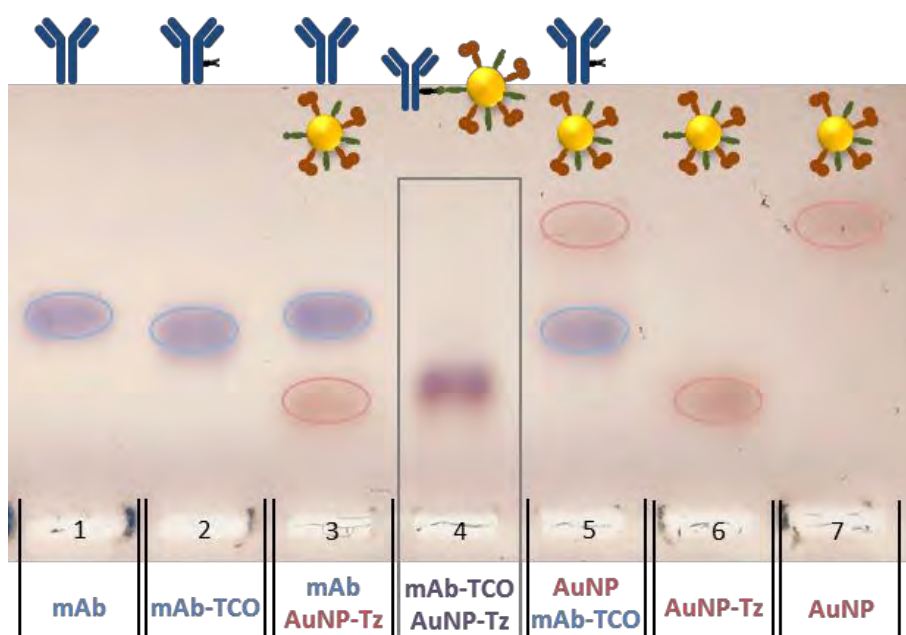

Figure 27: Agarose gel electrophoresis, stained with coomassie blue, to demonstrate occurance of click reaction between Trastuzumab-TCO (mAb-TCO) and multifunctionalized AuNPs (AuNP-Tz) (line 4). Including controls with non-functionalized Trastuzumab (mAb) and AuNPs without tetrazine functionalization (AuNP).

4.3.7 Radiolabelling of gold nanoparticles

To be able to track the AuNPs *in vivo*, a positron emitting radionuclide was inserted. The possibility to synthesize copper alloyed AuNPs allows the incorporation of the radionuclide copper-64 in the core (12). The synthesis of the radiolabeled particles was carried out following the procedure described above; however, $CuCl_2$ was spiked with radioactive $[^{64}Cu]CuCl_2$. This radionuclide is produced as a solution in 0.1 M HCl. Therefore, before tackling the preparation of the NPs, this solution was neutralized by adding an equivalent volume of a 0.1 M NaOH solution. To purify the AuNPs after the labeling by spin filtration, a 1 mM EDTA (Ethylenediaminetetraacetic acid) solution was used to remove all loosely bound ^{64}Cu. The labeling was monitored by radio-TLC using iTLC-SG chromatography paper (Agilent Technologies) and 20 mM citric acid + 60 mM EDTA solution as the stationary and mobile phases, respectively. The functionalization of the particles was performed as described above.

The radiochemical yield was low with only 5-10 %. However, competitive stability tests showed after 46 h at 37 °C in a 1 mM EDTA solution 98 % of ^{64}Cu were still bound to the AuNPs determined by iTLC (Figure 28).
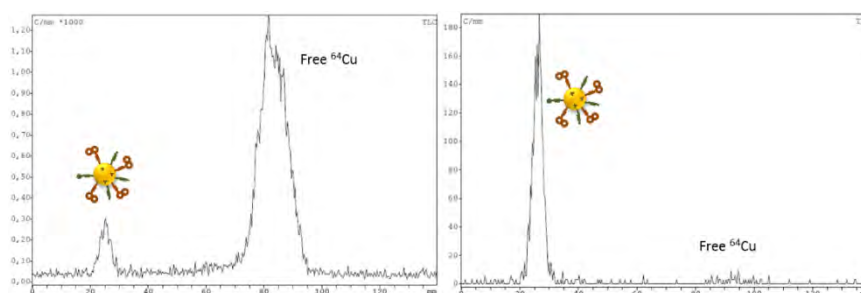

Figure 28: Chromatograms of radio-TLCs monitoring the radiolabeling of AuNPs with ^{64}Cu. Left: reaction mixture (7.4 % labeled), right: after purification with spin filtration, followed by verification of stability by incubation for 46 h in 1 mM EDTA solution at 37 °C (98 % labeled).

4.3.8 Pre-targeting gold nanoparticles *in vitro*

In vitro experiments were conducted to evaluate the pre-targeting strategy between TCO-Trastuzumab and multifunctionalized AuNPs. Therefore, the AuNPs were fluorophore-labeled with Cy3-NHS ester which binds to the PEG-amines of the particles. BT-474 cells were seeded in an ibidi μ-slide 8-well-plate (30 000 cells/well) and incubated overnight to adhere. Three different experimental groups were chosen and studied in parallel to enable comparison.

(i)   Pre-targeting: Trastuzumab-TCO + fully functionalized, Cy3-fluorophore labeled AuNPs

(ii)   Control 1: Trastuzumab non-functionalized + fully functionalized, Cy3-fluorophore labeled AuNPs

(iii)   Control 2: fully functionalized, Cy3-fluorophore labeled AuNPs

BT-474 cells were primarily stained with Hoechst33342 and Lysotracker-deep-red to visualize the nucleus and the lysosomes. The mAb for group (i) and (ii) was incubated for 30 min at 37 °C. The media with unbound mAb was removed, the Cy3-fluorophore labeled AuNPs added to all groups and incubated for 10 or 30 min (Figure 29 for experimental set-up). Images were taken using a live cell Axio Observer (Zeiss) fluorescence microscope. However, when analyzing the images with the ZEN-ZEISS software no difference could be witnessed between the three different experimental groups (Figure 30).
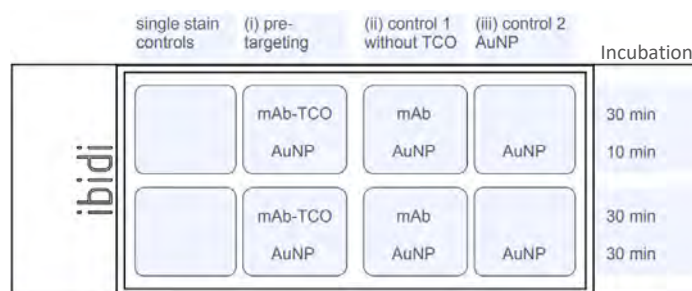

Figure 29: Ibidi 8-well-plate with experimental set-up for the evaluation of pre-targeting AuNPs on BT-474 cells by fluorescence microscopy.
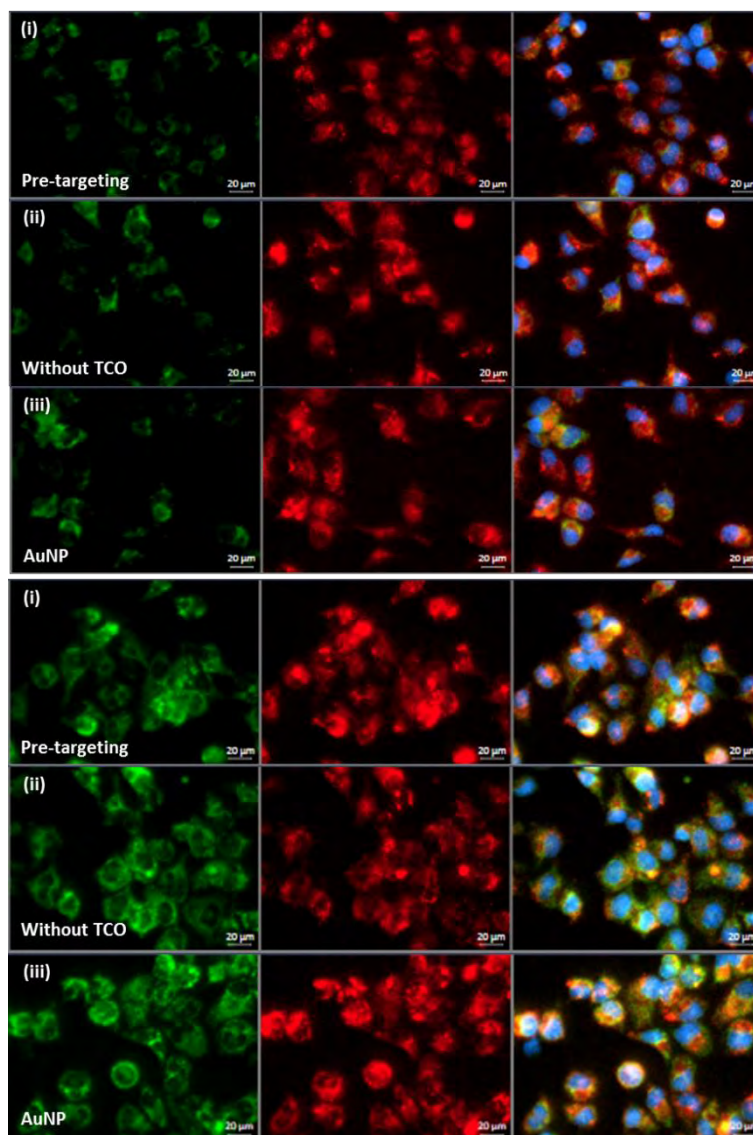
Figure 30: Representative images by fluorescence microscopy evaluating pre-targeting AuNPs on BT-474 cells. As control incubation of AuNP alone (iii) and with non-functionalized Trastzumab (ii) were performed. After 30 min incubation of mAb incubation of AuNPs followed for either 10 min (top) or 30 min (bottom). Nucleus stained with Hoechst33342 (blue), AuNPs with Cy3-NHS (green), lysosomes with Lysotracker-deep-red (red). Merged signal of AuNPs and lysosome in yellow.

The images of the different experimental groups showed very similar cell uptake of the fluorophore labeled AuNPs but with an increased signal after 30 min incubation compared to the 10 min incubation. We expected significant differences in the pre-targeting experiment after 10 min incubation of the AuNPs. If the TCO functionalized Trastuzumab was available on the cell membrane and if the click reaction occurred, an intense signal on the cell membrane should have been visible, which should decrease with longer incubation time due to internalization of the receptor-mAb-AuNP complex (2). However, after 10 min incubation of the AuNPs the fluorophore signal was low in all three cases and spread over the cell, co-localizing with the lysosomes, suggesting that internalization of the AuNP took already place. About the outcome of the experiments can be speculated; most likely Trastuzumab internalized too fast and wasn't available anymore for the click reaction with the AuNPs. A possibility to get more insight could be to execute the incubation of the mAb

at room temperature or at 4 °C to reduce internalization. Yet, the fast cell uptake in all three groups was not expected after the internalization studies done before. Yet, recalling the *ex vivo* internalization studies of Trastuzumab (see paragraph 4.3.5 Trastuzumab-TCO internalization studies *in vitro* and *ex vivo*) which confirms the presence of a fraction of Trastuzumab on the cell membrane even after 48 h, we expected a different outcome for the pre-targeting evaluation *in vivo*.

4.3.9 Pre-targeting gold nanoparticles *in vivo*

As the last step in the evaluation of our pre-targeting approach for multifunctionalized AuNPs as boron delivery agent in the application of BNCT, *in vivo* studies were performed. With that aim, three groups were formed out of female, BT-474 breast cancer xenograft bearing NOD/SCID mice. For all experiments fully functionalized and ^{64}Cu-radiolabeled AuNP were used (approximately 190 μg gold with 30-50 μCi (1-2 MBq) per mouse). In case of the pre-targeting group (G1, n = 4) 100 μg Trastuzumab-TCO per mouse was injected intravenously 24 h before the AuNPs. As control group (G2, n = 3) Trastuzumab without TCO conjugation was injected intravenously 24 h before the AuNPs. The last group, also used as control, received only AuNPs (G3, n = 4) (Figure 31).
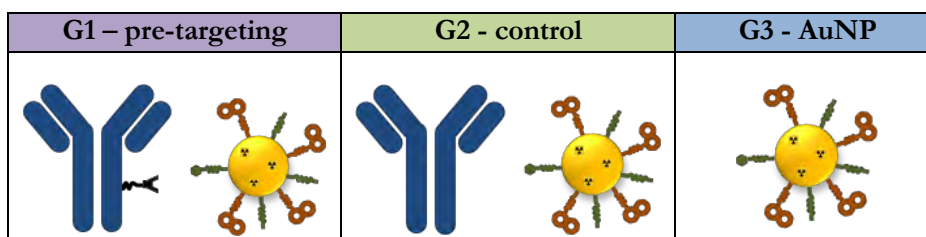

Figure 31: Experimental set up with three experimental groups for *in vivo* evaluation of pre-targeting multifunctionalized AuNPs. G1, the pre-targeting group, was injected with Trastuzumab-TCO followed by multifunctionalized AuNPs after 24 h. The control group G2 was injected with non-functionalized Trastuzumab followed by multifunctionalized AuNPs after 24 h. The third group (G3) received only multifunctionalized AuNPs.

PET-CT scans were performed approximately 1 h, 6 h, 24 h and 48 h post injection using the β- and X-cube micro system of Molecubes. All experiments were confirmed by *ex vivo* studies after the last PET scan. We first analyzed the third group, using PMOD software, to evaluate the biodistribution and tumor uptake of the AuNPs alone. The particles show a rather typical distribution for spherical gold nanoparticles (Figure 32 and Figure 34 top), however with higher liver and spleen uptake to what was expected for particles of such small size (core size 3-5 nm) (maximum at 6 h post injection with 31.4 ± 17.3 %ID/cm^3, respectively at 24 h with 13.5 ± 10.6 %ID/cm^3). Yet, in organs such as heart, lung and kidneys a steady decrease can be observed over time reaching around 5 %ID/cm^3 24 h post injection. The uptake in muscle, commonly used as reference for "healthy tissue", stays below 1 %ID/cm^3 over time.
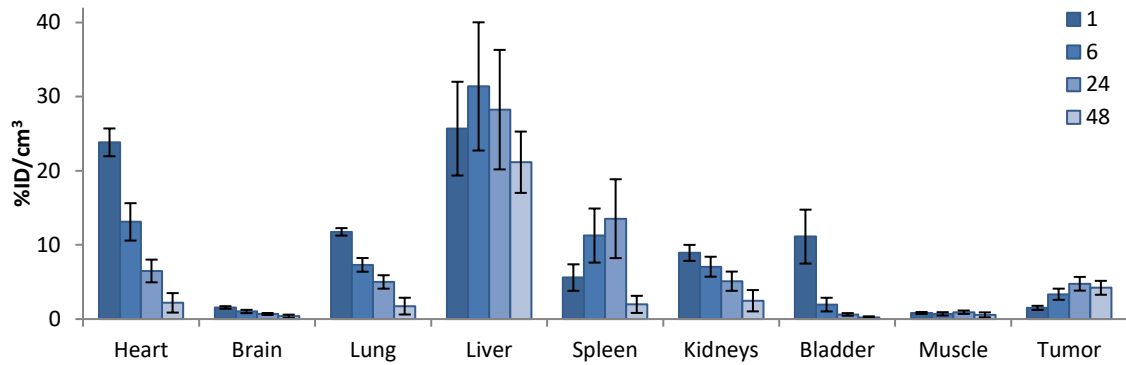
Figure 32: Accumulation of multifunctionalized [^{64}Cu]AuNP in different organs at different time points after intravenous administration, analyzed by PET imaging (values are expressed as mean ± standard error mean, n = 4).

A closer look to the tumor uptake revealed its maximum at 24 h post-injection with 4.8 ± 1.9 %ID/cm^3 followed by a slow clearance (Figure 33 and Figure 34, bottom). This result gives reason to believe that these nanoparticles follow the passive targeting by the EPR effect.
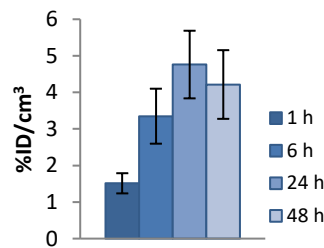
Figure 33: Tumor uptake of multifunctionalized [^{64}Cu]AuNP at different time points after intravenous administration, analyzed by PET imaging (values are expressed as mean ± standard error mean, n = 4).
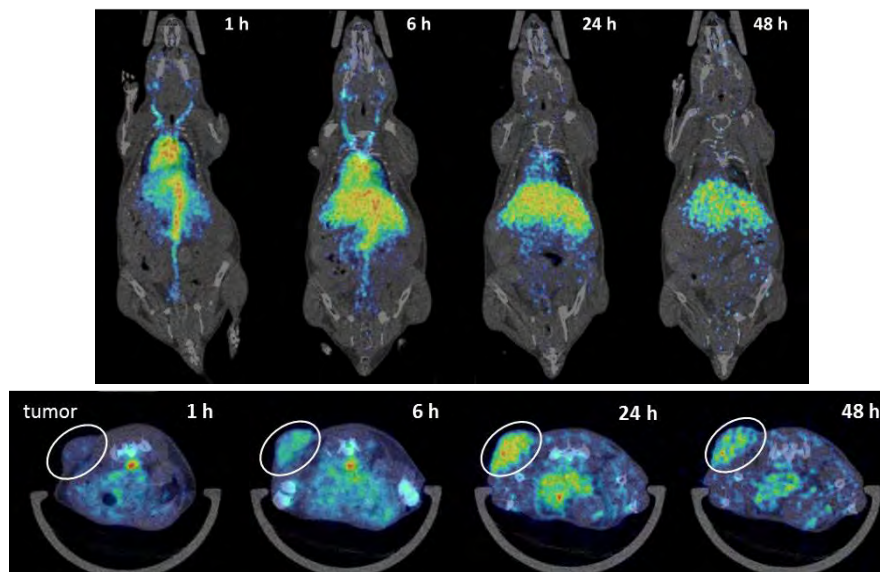
Figure 34: Representative PET images obtained at different time points after intravenous administration of [^{64}Cu]AuNPs. Top: coronal PET images (maximum intensity projections), bottom: representative axial PET images (average of 10 slices), positions of the tumor indicated. All images have been co-registered with representative CT slices for localization of the radioactive signal.

The control group G3, with solely AuNPs, showed slow elimination of the particles from the tumor at t > 24 hours, hence, we anticipated that the pre-targeting strategy may increase tumor accumulation by improving retention. Yet, a faster clearance from major organs and blood would be desirable for optimal pre-targeting results.

The analysis of the control (G2) and the pre-targeting (G1) group showed very similar biodistribution to the AuNP-group (G3). Analyzing the tumor uptake, a different pattern was expected for the pre-targeting group with a prolonged stay of the particles in tumor tissue, however, no significant difference could be observed between each group at any time point (Figure 35, left). After the 48 h PET-CT scan *ex vivo* studies were performed, confirming the obtained results from PET quantification by extracting the organs and analysing via gamma counter (Wallach Wizard, PerkinElmer) (Figure 35, right).
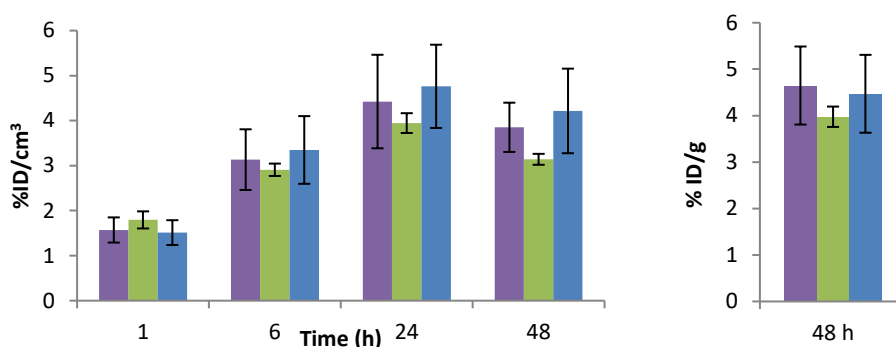
Figure 35: Tumor uptake of [^{64}Cu]AuNP in different experimental groups (purple: pre-targeting, green: control with non-TCO-functionalized mAb, blue: solely AuNP). Left: analyzed by PET imaging at different time points after intravenous administration. Right: analyzed by gamma counting 48 h after administration. (Values are expressed as mean ± standard error mean, G1 and G3: n = 4, G2: n = 3).

Furthermore ICP-MS analyses were performed after the radioactivity of the extracted organs was decayed. Liver, spleen and tumor were digested to determine their content of gold and boron. To not falsify the results of the boron determination no glass was used in any step during the process. Organs were digested in aqua regia overnight at 70 °C. The samples were filtered through cotton and diluted with 2 % HNO_3 to enable ICP-MS analysis. Good correlation between the ICP-MS and *ex vivo* data was achieved which leads to the conclusion that the functionalized AuNPs are stabile *in vivo* (Figure 36).

Figure 36: Amount of gold and boron in tumor at 48 hours after intravenous administration of pre-targeted [^{64}Cu]AuNP, as determined by gamma counting (dark purple) and ICP-MS (light purple). Values for gamma counting are obtained by multiplying the %ID/cm^3 (values from Figure 35) by the relative load of boron and gold in the nanosystems. (Values are expressed as mean ± standard error mean, n = 2).

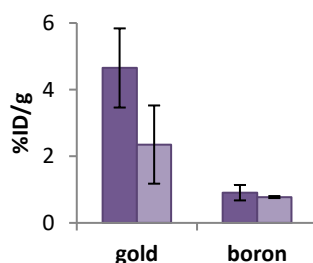## 4.4 Summary and conclusion

This chapter described the process towards the *in vivo* evaluation of pre-targeting in the application of BNCT. We sucessfully functionalized the tumor targeting antibody Trastuzumab for the pre-targeting approach obtaining a conjugate with an avergae of two TCO per mAb. Bio-acitivity of such didn't show significant impairment due to the modification acertained by cell binding assays. To enable *in vivo* studies, a BT-474 breast cancer xenograft mouse model on NOD/SCID mice was established and biodistribution studies of the functionalized Trastuzumab executed. Highest tumor uptake was reached at 48 h after intravenously injection with close to 25 %ID/cm^3. Cell internalizing studies by fluorescence microscopy of the TCO conjugated and Cy3-flourophore labeled mAb revealed cell uptake already within the first hour at 37 °C, reaching substantially complete uptake within 24 h. Also *in vivo* studies were performed to determine Trastuzumab internalization using a mixture of ^{89}Zr- and ^{131}I-radiolabelled Trastuzumab, showing significant difference between tumor uptake of each species. Hence, partial internalization of Trastuzumab *in vivo* was confirmed. Looking at the two experiments, the biodistribution and internalization of Trastuzumab, the time point for the injection of the second component in the pre-targeting strategy was set to 24 h after mAb injection, balancing between tumor uptake, sufficient clearance from blood and healthy tissue and internalization of the antibody.

As boron delivery agent small spherical gold nanoparticles (AuNPs) were loaded with the boron cluster COSAN and functionalized with tetrazine to enable the click reaction with TCO-Trastuzumab for the pre-targeting approach. The AuNPs were successfully synthesized, multifunctionalized and characterized for its physical properties (UV-VIS, TEM, DLS, Z-potential, ICP-MS) as well as its bio-compatibility (cytotoxicity, cell internalization). Incorporation of the positron emitter ^{64}Cu was executed by synthesizing a copper alloyed gold core, enabling *in vivo* tracking of the AuNPs.

Finally, it was verified by agarose gel electrophoresis that the two components, the Trastuzumab-TCO and the tetrazine-AuNPs, are able to undergo the click reaction with each other and the pre-targeting approach could be evaluated. Therefore *in vitro* and *in vivo* studies were performed, using fluorescence microscopy on BT-474 cells and PET-CT analysis on a BT-474 breast cancer xenograft mouse model, respectively. For both experimental set-ups control groups were generated by using non-functionalized Trastuzumab as well as AuNPs alone. However, no significant differences could be observed *in vitro* or *in vivo* between the three groups. Cell and tumor uptake respectively were similar for all cases.

For the work of this PhD thesis the aim was to use nanoparticles with fast clearance to prevent toxicity to non-tumor tissue but present the possibility to carry a high amount of boron next to the functionalization with tetrazine to enable pre-targeting. Looking at the biodistribution of the AuNPs in hand the high liver uptake and rather slow clearance from other organs such as kidneys and lung as well as the tumor showed that these particles do not possess the desired properties for pre-targeting. Yet, high boron loading was achieved and tumor uptake due to the EPR effect could be witnessed. Hence, investigation in the particles as boron delivery agents should be continued; however, pre-targeting could not bring the desired improvement.

4.5 Experimental part

4.5.1 Reagents

All reagents were obtained from Sigma-Aldrich unless otherwise stated. Milli-Q water (resistivity 18.2 MΩ·cm at 25 °C) was used in all experiments. *p*-NCS-Bz-DFO was obtained from CheMatech, Cy3-NHS was purchased from BroadPharm, mTzCy3 from Jena Biosciense and Cy3-TCO from AAT Bioquest. The antibody Trastuzumab was purchased from Roche Farma, S.A. España. $[^{89}Zr]ZrC_2O_4$ (in 1 M oxalic acid) was produced in house with an IBA Cyclone 18/9 cyclotron using a (p, n) reaction on natural yttrium-89 and isolated with a hydroxamate column following standard protocol. $[^{64}Cu]CuCl_2$ (in 0.1 M HCl) was produced in house with an IBA Cyclone 18/9 cyclotron using a (p, n) reaction on a gold disk, electroplated with enriched nickel-64 and isolated with an ion exchange column following standard protocol. $[^{131}I]INa$ (in 0.1 M NaOH) was purchased from PerkinElmer. A stock of BT-474 cells was kindly donated from biodonostia (San Sebastián, Spain). Animals were purchased from Charles River Laboratories France.

4.5.2 Instrumentation

UV-Vis spectra were measured in a Jasco V630BIO Spectrophotometer or in NanoDrop® ND-1000 V3.5.2

Flow cytometry based on fluorescence-activated cell sorting (FACS) studies were performed using a BD FACS Canto II Flow Cytometer and analyzed by FlowJo V7.6.5.

Cell observer microscopy experiments were carried out using a Zeiss Axio Observer Fluorescence microscope using Ibidi clear bottomed μ-slide 8-well microscopy plates and analyzed by ZEN2012-ZEISS.

Confocal cell microscopy experiments were carried out using a Zeiss 880 Confocal Fluorescence microscope using Ibidi clear bottomed μ-slide 8-well microscopy plates and analyzed by ZEN2012-ZEISS.

Transmission electron microscopy (TEM) was performed using a JEOL JEM-1400 plus microscope (Jeol, Tokyo, Japan) working at 120 kV. The carbon film of copper grids (CF400-Cu) was treated under air plasma in a glow discharge system (K100X, Emitech, Kent, UK, 40 mA during 2 min) just before sample preparation. For TEM examinations, a single drop (1μL) of the NPs solution was placed onto a copper grid coated with a carbon film (Electron Microscopy Sciences, Hatfieled, PA, USA). After 1 min, the drop was removed with filter paper and the sample was incubated with 3 μL of uranyl acetate 0.5% (3 min).

ICP-MS measurements were performed on a Thermo iCAP Q ICP-MS (Thermo Fisher ScientificGmbH, Bremen, Germany). An ASX-560 autosampler was coupled to the ICP-MS (CETAC Tech, Omaha, NE, USA).

DLS and ζ-potential measurements were performed using a Malvern Zetasizer Nano ZS system (Malvern Instruments, Malvern, UK). The particle size measurement settings were: 3 measurements/14 runs/10s in scattered mode at 173° angle. Measurements were conducted at T = 25 °C and neutral pH.

Gamma counts were measured using a Wallach Wizard, PerkinElmer (Waltham, MA, USA) gamma counter.

Radio-thin layer chromatography (radio-TLC) was performed using iTLC-SG chromatography paper (Agilent Technologies, CA, USA) and 20 mM citric acid + 60 mM EDTA/acetonitrile solution (9/1 v/v) as the stationary and mobile phases, respectively. TLC plates were analyzed using a TLC-reader (MiniGITA, Raytest).

PET experiments were performed using an eXploreVista-CT small animal PET-CT system (GE Healthcare) or the β- and X-cube micro system of Molecubes. Anesthesia was induced with 3-5 % isoflurane and maintained by 1.5-2 % of isoflurane in 100% O_2.

4.5.3 Tumor growth

Cells
BT-474 cells were cultured in DMEM medium (100X, 10378-016 Gibco; 10 % fetal bovine serum, 1 % penicillin-streptomycin) at 37 °C with 5% CO_2 in a humid atmosphere. Cells were confirmed to be free of mycoplasma contamination.

Animals
All animal experiments were performed in accordance with the Spanish policy for animal protection (RD53/2013), which meets the requirements of the European Union directive 2010/63/UE regarding the protection of animals used in experimental procedures. All experimental procedures were approved by the Ethical Committee of CIC biomaGUNE and authorized by the local authorities. All animals were housed in ventilated cages and fed on a standard diet *ad libitum*. The studies were performed on female NOD.CB17-Prkdcscid/J mice.

Tumor growth
To grow BT-474 cell line breast cancer xenografts on female NOD.CB17-Prkdcscid/J mice 5-6 weeks old mice were operated to implant a 17β-estradiol pellet (belma technologies) subcutaneously at their neck. The next day $10*10^6$ BT-474 tumor cells were inoculated per animal subcutaneously at the flank of the mouse. Prior to each inoculation a Lonza Mycoplasma test was carried out to ensure that the cells weren't contaminated, finally cells were diluted in sterile PBS:Matrigel (1:1). The sizes of the tumors were measured every 2-3 days with a digital calliper and volumes calculated ($V = \frac{\text{short diameter}^2 * \text{long diameter}}{2}$). At the time the tumour reached 200-300 mm^3 (around 2 weeks after inoculation *in vivo* studies could be performed. The defined human endpoints were: (i) weight loss greater than 20 % in one week, (ii) one or more of the following clinical signs: abdominal distension, dyspnoea, cachexia or stooping, (iii) the absence of response to stimuli and lethargy, (iv) a tumor larger than 1.5 cm in average diameter and (v) ulcerated or necrotic tumors or wounds / aggressions severe infected.

4.5.4 Chemistry and Radiochemistry - Trastuzumab

Conjugation of TCO-NHS to Trastuzumab

The mAb was diluted in PBS (phosphate-buffered saline, pH 7.4) to a concentration of 3.0 mg/mL. The pH was adjusted to 8.6 – 9.1 with 0.1 M Na_2CO_3. 50-55 moles eq. TCO-NHS (20 mM in DMSO) was added. After incubation (60 min, RT) non-reacted TCO-NHS was removed by spin filtration (100 kDa, 12000 rpm) and the conjugated mAb washed three times with PBS. After recovering the mAb from the filter with PBS its concentration was determined by NanoDrop®.

Conjugation of TCO-NHS and Df-Bz-NCS to Trastuzumab

The mAb was diluted in PBS to a concentration of 1.5 – 3.0 mg/mL. The pH was adjusted to 8.6 – 9.1 with 0.1 M Na_2CO_3. TCO-NHS (20 mM in DMSO, 55 eq.) and *p*-NCS-Bz-DFO (5 mM in DMSO, 5 eq.) was added. After incubation (45 min at 37 °C) purification was performed by spin filtration (100 kDa, 12000 rpm) and the conjugated mAb washed three times with PBS. After recovering the mAb from the filter with PBS its concentration was determined by NanoDrop®.

Conjugation of Df-Bz-NCS to Trastuzumab

The mAb was diluted in PBS to a concentration of 1.5 – 3.0 mg/mL. The pH was adjusted to 8.6 – 9.1 with 0.1 M Na_2CO_3. *p*-NCS-Bz-DFO (5 mM in DMSO, 5 eq.) was added and incubated for 45 min at 37 °C. Purification was performed by spin filtration (100 kDa, 12000 rpm) and the conjugated mAb washed three times with PBS. After recovering the mAb from the filter with PBS its concentration was determined by NanoDrop®.

Radiolabeling of Trastuzumab with ^{89}Zr

Radiolabeling of the DFO conjugated mAb with ^{89}Zr was performed by incubation with $[^{89}Zr]ZrC_2O_4$ in a 1 M oxalic acid solution. Therefore 50 µl of 1 M oxalic acid containing ^{89}Zr (0.6 mCi = 22.2 MBq) were neutralized with 2 M sodium carbonate, 450 ug mAb was added and the volume adjusted to 0.5 mL with 0.5 M HEPES buffer. After 1 h incubation at room temperature the mAb was purified by sephadex G-25 size exclusion column (NAP5® GE Healthcare) and PBS. The incubation and purification was monitored by iTLC (mobile phase: 20 mM citric acid + 60 mM EDTA 9:1 acetonitrile). Radiochemical yield of the purified ^{89}Zr-Trastuzumab was 64.2 ± 21.6 % (n = 5).

Radiolabeling of Trastuzumab with ^{131}I

An Eppendorf tube was coated with 75 µg Iodogen (1,3,4,6-tetrachloro-3α,6α-diphenyl glycoluril). 50 µL 0,5 M sodium phosphate buffer, 427 µL 0,1 M sodium phosphate buffer and 19 µL (0,4 mg) Trastuzumab (21 mg/mL) were added. Finally 4 µL of $[^{131}I]INa$ (200 µCi = 7.4 MBq in 0.1 M NaOH). After 4 min incubation at room temperature the reaction was quenched with 100 µL VitaminC solution (25 mg/mL milliQ water, pH = 5). Labeling was monitored by iTLC (mobile phase: 20 mM citric acid + 60 mM EDTA). The radiolabeled mAb was purified using sephadex G-25 size exclusion column (PD10® GE Healthcare) and VitaminC solution (5 mg/mL saline, pH ≈ 5). Radiochemical yield of the purified ^{131}I-Trastuzumab was 72.4 %. Lindmo assay was performed to assure bioactivity of the mAb was not impaired.

Fluorophore-labeling of Trastuzumab-TCO with mTzCy3

To a solution of Trastuzumab-TCO in PBS (1.5 - 3.0 mg/mL) 5 eq. mTzCy3 (6-Methyl-Tetrazine-Sulfo-Cy3, 1 mg/mL in DMSO) was added and incubated for 5 min at room temperature. The fluorophore-labeled mAb was purified by spin filtration (100 kDa, 12000 rpm) and washed four times with PBS. After recovering the mAb with PBS from the filter the concentrations of mAb and mTzCy3 were determined by NanoDrop®.

4.5.5 Chemistry and Radiochemistry - AuNP

Synthesis of AuNPs

For the synthesis of AuNPs the protocol of Yongfeng Zhao et al. was used as base (12). In a 10 mL glass vial 0.9 mL MQ water were mixed with 10 μL HAuCl$_4$ (100 mM in MQ, 0.4 mg, 1 eq), 10 μL CuCl$_2$ (10 mM in MQ, 0.1 mg, 1 eq) and 25 μL NH$_2$-PEG$_{5k}$-SH (10 mM in MQ, 2.5 mg, 0.25 eq). Under vigorous stirring 100 μL NaBH$_4$ (40 mM in MQ, 0.2 mg, 4 eq; freshly prepared) were added drop wise. After 2 min the stirring was stopped and the particles were allowed to settle for 2 h at room temperature. Purification was performed by spin filtration (30 kDa, 12 000 rpm) including 3 washings with PBS (phosphate buffered saline, pH 7.4) and the particles were recovered from the filter in 400 μL PBS. 13 μL COSAN-SH (20 mM in EtOH, 0.1 mg, 0.25 eq) were added and incubated for 1 h at room temperature. After purification via spin filter as described above the pH of the AuNP suspension was adjusted to 8 - 9 with 0.1 M NaOH and 25 μL Tz-PEG$_5$-NHS (20 mM in DMSO, 0.3 mg, 0.5 eq) were added. After 1 h incubation at room temperature the particles were purified by spin filtration and recovered in 400 μL PBS. The AuNPs were analyzed by UV-Vis, DLS, Z-potential, ICP-MS and TEM.

Fluorophore-labeling of AuNP with TCO-Cy3

The multifunctionalized AuNPs (450 μL in PBS, 0.2 mg/mL) were incubated with 3 μL TCO-Cy3 (10 mM in DMSO) for 5 min at room temperature. The particles were purified by spin filtration (30 kDa) and recovered in PBS. The labeling was confirmed by UV-VIS spectra.

Fluorophore-labeling of AuNP with Cy3-NHS

The multifunctionalized AuNPs (450 μL in PBS, 0,2 mg/mL) were adjusted in pH to 8.6-8.9 and 5 μL Cy3-NHS (1 mg/mL in DMSO) were added. After 1 h incubation at room temperature particles were purified by spin filtration (30 kDa) and recovered in PBS. The labeling was confirmed by UV-VIS spectra.

Agarose (1.5 %) gel electrophoresis

A 1.5 % agarose gel was prepared following standard protocol. In brief 1.5 g agarose were suspended in 100 mL Tris-Borate-EDTA (TBE) buffer and heated until it almost reached its boiling point. The solution was poured in a gel chamber, the comb placed and let settle to polymerize. Samples were prepared in 20 μL aqueous batches, including 5 μL loading buffer. 10 μL were loaded on the gel and run for approximately 1 h at 100 V. To visualize the antibody on the gel it was incubated 1 hour in coomassie blue, followed by 2 days in destaining solution to reduce the background staining.

Radiosynthesis of AuNPs

For the synthesis of ^{64}Cu labeled AuNPs the protocol of Yongfeng Zhao et al. was used as base (12). In a 10 mL glass vial 0.9 mL MQ water were mixed with 10 μL HAuCl$_4$ (100 mM in MQ, 0.4 mg, 1 eq), ^{64}CuCl$_2$ (in 0.1 M HCl, 2.5 mCi = 92.5 MBq), neutralized with NaOH (0.1 M) and 25 μL NH$_2$-PEG$_{5k}$-SH (10 mM in MQ, 2.5 mg, 0.25 eq). Under vigorous stirring 100 μL NaBH$_4$ (40 mM in MQ, 0.2 mg, 4 eq; freshly prepared) were added drop wise. After 2 min the stirring was stopped and the particles were allowed to settle for 2 h at room temperature. Purification was performed by spin filtration (30 kDa, 12 000 rpm) including 3 washings with 1 mM EDTA and the particles were recovered from the filter in 400 μL PBS. The radiolabeling and purification was monitored by iTLC (mobile phase: 20 mM citric acid + 60 mM EDTA, Rf(AuNP) = 0, Rf(^{64}Cu-EDTA) = 0.5). 13 μL COSAN-SH (20 mM in EtOH, 0.1 mg, 0.25 eq) were added and incubated for 1 h at room temperature. After purification via spin filter as described above the pH of the AuNP suspension was adjusted to 7.8 – 8.8 with 0.1 M NaOH and 25 μL Tz-PEG$_5$-NHS (20 mM in DMSO, 0.3 mg, 0.5 eq) were added. After 1 h incubation at room temperature the particles were purified by spin filtration and recovered in 400 μL PBS. The radiochemical yield was 6.5 %.

4.5.6 *in vitro* studies

Lindmo assay

The assay was perfomed using the protocol of Lindmo as base (9). The binding assay for Trastuzumab was set up using one concentration of mAb (10-15 ng/mL) and different dilutions of 0.5 mL BT-474 cells in PBS/1%BSA (2.8 - 0.2*10^6 cells/mL) in triplicates. The lowest concentration was prepared twice, the second set serving as non-specific binding (NSB) control (containing 2 μL of 5 mg/mL non-labelled mAb). To each cell dilution 0.5 mL of modified and radiolabelled Trastuzumab was added and incubated in a head over head rotator at 4 °C over night. The cell suspensions were centrifuged, 500 uL of the supernatant seperated and all samples (pellets and supernatans) meassured in a gamma-counter. The activity meassured from the supernatants was substratced from the pellet activity and the immunoreactive fraction calculated.

FACS study with Trastuzumab-TCO-mTzCy3

BT-474 cells were seeded in a 24-well-plate (500 000 cells/well) and incubate overnight to adhere (37 °C, 5% CO$_2$). The media was removed and 0.5 mL fresh media added to the control wells of non-labeled and viability. To the other wells 0.5 mL of Cy3-fluorophore-labled Trastuzumab (0.1, 0.05 or 0.01 mg/mL) were added. The incubation (5, 10, 15, 20 and 30 min) at room temperature was stopped by removing the media and detach cells with trypsin. The suspensions were transferred into FACS tubes, centrifuged, the supernatant removed and resuspend in 0.5 mL PBS. 0.1 mL viability (Zombie) control was added to all samples (except non-labeled control) and incubated for 13-30 min at room temperature. The samples were washed with FACS-buffer (10 mM PBS/1%BSA) via centrifuge and resuspend in 0.2 mL for FACS measurements.

In vitro internalizing studies of Trastuzumab-TCO-mTzCy3

BT-474 cells were seeded in a poly-L-Lysine treated 'Ibidi' μ-slide 8-well-plate (30 000 cells/well in 0.3 mL) and incubate overnight to adhere (37 °C, 5% CO$_2$, humid

atmosphere). The media was removed and 0.1 mL Hoechst 33342 (1 μg/mL) added to stain the nucleus. After 10 min incubation (37 °C, 5% CO_2, humid atmosphere) 0.1 mL Lysotracker-deep-red (1 μg/mL) was added to stain the lysosomes. After 20 min incubation (37 °C, 5% CO_2, humid atmosphere) media was removed and 0.3 mL of Cy3-labeled Trastuzumab (10 μg/mL in media) added. After 1 h incubation (37 °C, 5% CO_2, humid atmosphere) the media was removed and replaced with fresh media. The images were taken at different time points with a fluorescence confocal microscope (Zeiss LSM 880). Controls of single staining for each fluorophore were included. Images were analyzed by ZEN-ZEISS software.

Cytotoxicity studies of AuNPs

To determine cell viability, BT-474 human breast cancer cells were incubated with multifunctionalized AuNPs over 24 h, 48 h and 72 h. Cells were seeded ($3×10^4$ cells/well, 100 μL/well, 96-well plate), allowed to adhere overnight in complete media and maintained in a humid atmosphere at 37 °C and 5 % CO_2. Then, media was removed and cells were left untreated (control) or incubated with the AuNP-containing formulations, diluted accordingly in media. The experiments were performed in triplicates. After the desired time, cell supernatant was removed and 100 μL/well of MTT reagent (Roche), diluted in the corresponding media to the final concentration of 0.25 mg/mL, was added. After 1 hour incubation at 37 °C and 5 % CO_2, the excess reagent was removed and formazan crystals were solubilized by adding 200 μL of DMSO per well. The optical density of each well was measured in a TECAN Genios Pro 96/384 microplate reader at 550 nm. Data was represented as the percentage of cell survival compared to control wells.

In vitro internalizing studies of AuNP-Tz-TCOCy3

BT-474 cells (ps. 17) were seeded in a poly-L-Lysine treated 'Ibidi' μ-slide 8-well-plate (30 000 cells/well in 0.3 mL) and incubate overnight to adhere (37 °C, 5% CO_2, humid atmosphere). The media was removed and 0.1 mL Hoechst 33342 (1 μg/mL in media) added to stain the nucleus. After 10 min incubation (37 °C, 5% CO_2, humid atmosphere) 0.1 mL Lysotracker-deep-red (1 μg/mL in media) was added to stain the lysosomes. After 20 min incubation (37 °C, 5% CO_2, humid atmosphere) media was removed and 0.3 mL of Cy3-labeled AuNP (20 μg/mL in medium) added. After 2 h incubation (37 °C, 5% CO_2, humid atmosphere) the media was removed and replaced with fresh media. The images were taken with a Cell Axio Observer Fluorescence Microscope. Controls of single staining for each fluorophore were included. Images were analyzed by ZEN-ZEISS software.

In vitro pre-targeting studies of Trastuzumab-TCO and Cy3-AuNP-Tz

BT-474 cells (ps. 17) were seeded in a poly-L-Lysine treated 'Ibidi' μ-slide 8-well-plate (30 000 cells/well in 0.3 mL) and incubate overnight to adhere (37 °C, 5% CO_2, humid atmosphere). The media was removed and 0.1 mL Hoechst 33342 (1 μg/mL in media) added to stain the nucleus. After 10 min incubation (37 °C, 5% CO_2, humid atmosphere) 0.1 mL Lysotracker-deep-red (1 μg/mL in media) was added to stain the lysosomes. After 20 min incubation (37 °C, 5% CO_2, humid atmosphere) media was removed and 0.1 mL Trastuzumab-TCO (1.0 μM) added. After 30 min incubation (37 °C, 5% CO_2, humid atmosphere) the media was removed and 0.3 mL of Cy3-labeled AuNP (20 μg/mL in medium) added. Incubation was done for 10 min or 30 min (37 °C, 5% CO_2, humid

atmosphere), the media removed and replaced with fresh media. The images were taken with a Cell Axio Observer Fluorescence Microscope. Controls of single staining for each fluorophore were included. Images were analyzed by ZEN-ZEISS software.

4.5.7 *in vivo* studies

Ex vivo studies to explore Trastuzumab internalization in vivo

Trastuzumab was labeled in two batches, one with ^{89}Zr, the other one with ^{131}I. A mixture out of the two was created to obtain a 1:1 ratio of their activity (e.g. per mouse 5 µCi = 0.185 MBq each). Four mice were selected out of female, BT-474 breast cancer xenograft bearing NOD/SCID mice and injected intravenously, each with about 100 µg Trastuzumab. Ex vivo studies were performed 24 h (n = 2) and 48 h (n = 2) post injection. Extracted organs were measured in a gamma counter (Wallach Wizard, PerkinElmer, Waltham, MA, USA) using a dual method enabling separate determination of ^{89}Zr and ^{131}I counts. The percentage of injected dose per gram (%ID/g) was calculated for the tumor uptake at both time points and for each radionuclide.

In vivo PET imaging studies

<u>Biodistribution of Trastuzumab</u>: Three animals were selected out of female, BT-474 breast cancer xenograft bearing NOD/SCID mice. In those experiments aimed at determining the biodistribution of the mAb, [^{89}Zr]Trastuzumab (100 µg, 100 µL, 2.4-2.6 MBq) was injected via tail vein. Imaging studies were conducted using positron emission tomography (PET) in combination with computerized tomography (CT), using an eXplore Vista-CT small animal PET-CT system (GE Healthcare). Static whole-body images (2 beds) were acquired at 1, 8, 24, 48 and 72 h after administration. PET images were analysed using PMOD image analysis software (PMOD Technologies Ltd, Zürich, Switzerland).

<u>Pre-targeting evaluation</u>: Three groups of animals (G1 and G3: n = 4, G2: n = 3) were selected out of female, BT-474 breast cancer xenograft bearing NOD/SCID mice. Approximately 100 µg per mouse of TCO functionalized Trastuzumab (~2 TCO/mAb) were injected intravenously via tail vein for the pre-targeting group. The same amount respectively of non-functionalized Trastuzumab for the control group. 24 h post injection the multifunctionalized and ^{64}Cu-radiolabeled AuNPs (200 µg gold in 100 µL PBS with 30-50 µCi (1.1-1.9 MBq) per mouse) were injected intravenously. The same amount was injected to the third group which did not receive Trastuzumab beforehand. Imaging studies were conducted using positron emission tomography (PET) in combination with computerized tomography (CT), using the β- and X-cube micro system of Molecubes. Static whole-body images (1 bed) were acquired in a 511 keV ± 30 % energetic window at 1 h, 6 h, 24 h and 48 h post injection (acquisition time 20 min for 1 h and 6 h, 45 min for 24 h and 60 min for 48 h). PET images were analyzed using PMOD image analysis software (PMOD Technologies Ltd, Zürich, Switzerland).

Digestion of organs for ICP-MS analysis

ICP-MS analysis was performed for gold, boron and cobalt. The organs/tissue liver, spleen and tumor were digested from one animal per group. No glass could be used in any way during the process, as it would lead to falsify the results of the boron determination. Organs

were dissolved in aqua regia overnight at 70 °C. To each sample 0.5 mL H_2O_2 was added, the samples filtered through cotton and the volume adjusted to 15 mL with 2 % HNO_3.

4.6 References

1. *Trastuzumab Emtansine (T-DM1): A Novel Agent for Targeting HER2 Breast Cancer.* **Howard A. Burris III, Jay Tibbitts, Scott N. Holden, Mark X. Sliwkowski, Gail D. Lewis Phillips.** 5, s.l. : Elsevier Inc, 2011, Clinical Breast Cancer, Vol. 11, pp. 275-82.

2. *Bioorthogonal two-component drug delivery in HER2(+) breast cancer mouse models.* **Sudath Hapuarachchige, Yoshinori Kato & Dmitri Artemov.** 2016, Scientific Reports, Vol. 6.

3. *Bioorthogonal chemistry amplifies nanoparticle binding and enhances the sensitivity of cell detection.* **Jered B. Haun, Neal K. Devaraj, Scott A. Hilderbrand, Hakho Lee and Ralph Weissleder.** s.l. : Macmillan Publishers Limited., 2010, NATURE NANOTECHNOLOGY, Vol. 5, p. 660.

4. *In Vivo Pretargeted Imaging of HER2 and TAG-72 Expression Using the HaloTag Enzyme.* **James C. Knight, Michael Mosley, H. Tetsuo Uyeda, Mei Cong, Frank Fan, Stephen Faulkner and Bart Cornelissen.** s.l. : American Chemical Society, 2017, Mol. Pharmaceutics, Vol. 14, p. 2307−2313.

5. *The new era of nanotechnology, an alternative to change cancer treatment.* **Ancuta Jurj, Cornelia Braicu, Laura-Ancuta Pop, Ciprian Tomuleasa, Claudia Diana Gherman, Ioana Berindan-Neagoe.** s.l. : Dovepress, 2017, Drug Design, Development and Therapy, Vol. 11, pp. 2871–2890.

6. *Insight into nanoparticle cellular uptake and intracellular targeting.* **Basit Yameen, Won Il Choi, Cristian Vilos, Archana Swami, Jinjun Shi, Omid C. Farokhzad.** s.l. : Elsevier B.V., 2014, Journal of Controlled Release, Vol. 190, pp. 485–499.

7. *Caveolin-1 mediates cellular distribution of HER2 and affects trastuzumab binding and therapeutic efficacy.* **Patrícia M.R. Pereira, Sai Kiran Sharma, Lukas M. Carter, Kimberly J. Edwards, Jacob Pourat, Ashwin Ragupathi, Yelena Y. Janjigian, Jeremy C. Durack & Jason S. Lewis.** s.l. : Springer Nature, 2018, NATURE COMMUNICATIONS, Vol. 9, p. 5137.

8. *Molecular mechanism and physiological functions of clathrin-mediated endocytosis.* **Boucrot, Harvey T. McMahon and Emmanuel.** s.l. : Macmillan Publishers Limited, 2011, NATURE REVIEWS | MOLECULAR CELL BIOLOGY, Vol. 12, p. 517.

9. *Determination of the Immunoreactive Fraction of Radiolabeled Monoclonal Antibodies by Linear Extrapolation to Binding at Infinite Antigen Excess .* **T. Lindmo, E. Boven, F. Cuttitta, J. Fedorko and P.A. Bunn, Jr.** s.l. : Elsevier Science Publishers B.V. , 1984, Journal of lmmunological Methods, Vol. 72, pp. 77-89 .

10. *Comparison of the octadentate bifunctional chelator DFO*-pPhe-NCS and the clinically used hexadentate bifunctional chelator DFO-pPhe-NCS for 89Zr-immuno-PET.* **Danielle J. Vugts, Chris Klaver, Claudia Sewing, Alex J. Poot, Kevin Adamzek, Seraina Huegli, Cristina Mari, Gerard W. M. Visser, Ibai E. Valverde, Gilles Gasser, Thomas L. Mindt & Guus A. M. S. van Dongen.** s.l. : Springer, 2017, Eur J Nucl Med Mol Imaging, Vol. 44, pp. 286–295.

11. *Gold Nanoparticles as Boron Carriers for Boron Neutron Capture Therapy: Synthesis, Radiolabelling and In Vivo Evaluation.* **Krishna R. Pulagam, Kiran B. Gona, Vanessa Gómez-Vallejo, Jan Meijer,**

Carolin Zilberfain, Irina Estrela-Lopis, Zuriñe Baz, Unai Cossío and Jordi Llop. 2019, Molecules, Vol. 24, p. 3609.

12. *Facile synthesis, pharmacokinetic and systemic clearance evaluation, and positron emission tomography cancer imaging of ^{64}Cu–Au alloy nanoclusters.* **Yongfeng Zhao, Deborah Sultan, Lisa Detering, Hannah Luehmann and Yongjian Liu.** s.l. : The Royal Society of Chemistry, 2014, Nanoscale, Vol. 6, pp. 13501–13509.

Chapter 5: Pre-targeting boron carbon dots

5.1 Introduction

Carbon dots (CDs) are used in a broad field of applications such as sensing for metals, chemicals and biologicals, improvement of solar cells and biological approaches like bio imaging and drug delivery (1; 2). Having a closer look to boron doped carbon dots (B-CDs) and their use in biological approaches, metal- and chemo-sensing combined with bioimaging are the most common applications. Existing B-CDs are developed to detect among others blood sugar (3), H_2O_2 (4), dopamine (5) and a variety of metals, like Cr(VI) (5), Hg(II) (6), Al(III) (7), Cu(II) and Fe(III) (8).

The presence of boron atoms in B-CDs, together with the high biocompatibility, low cytotoxicity and rather fast and inexpensive synthesis, suggests their potential application as boron-10 delivery agents in the context of Boron Nature Capture Therapy (BNCT). Yet, to the best of our knowledge, B-CDs have never before been investigated for BNCT.

In this work we prepared and characterized boron doped carbon dots, functionalized with a tetrazine moiety to enable pre-targeting. To evaluate the approach *in vivo*, the same tumor-mouse-model was used as in Chapter 4 for the pre-targeting of AuNPs. Hence, as targeting counterpart TCO-functionalized Trastuzumab was used. To enable Positron Emission Tomography (PET) imaging of B-CDs, these were radiolabeled with the positron emitter fluorine-18, and PET studies were carried out to determine tumor accumulation of the B-CDs (see Figure 1 for schematic representation of the work included in this chapter).
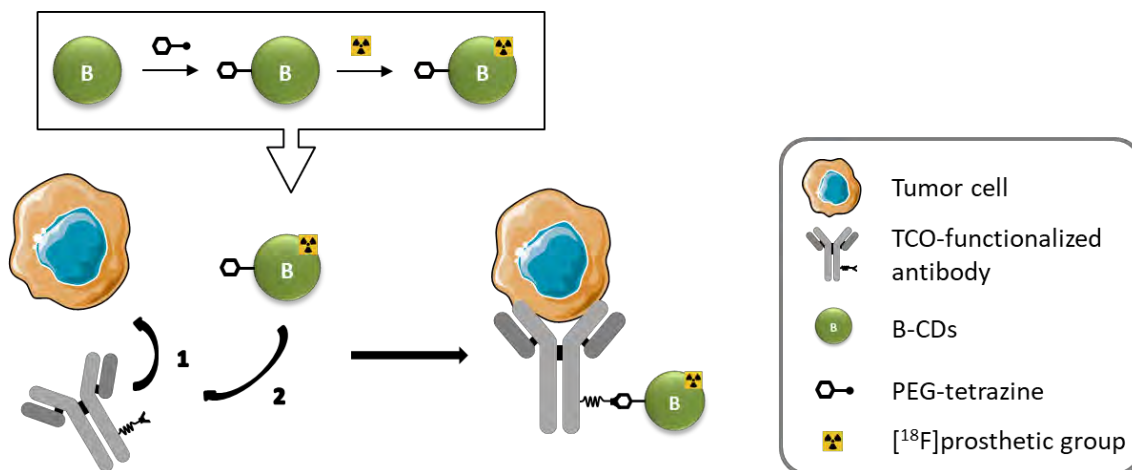

Figure 1: Schematic representation of the pre-targeting strategy using tetrazine functionalized and ^{18}F-radiolabeled B-CDs.

5.2 Objectives

The specific objectives of this work were:

1. To synthesize and characterize tetrazine-functionalized boron carbon dots (B-CDs)
2. To develop a radiolabeling strategy for the incorporation of the positron emitter fluorine-18 to tetrazine-functionalized B-CDs (B-CDs-Tz).
3. To evaluate the capacity of B-CDs-Tz to accumulate in the tumor, using a mouse tumor model of breast cancer and a pre-targeting strategy.

5.3 Results and discussion

5.3.1 Synthesis, functionalization and characterization of B-CDs

The strategy of pre-targeting relies in the fact that the second component, administered after the administration of the functionalized antibody, presents a fast clearance. In imaging experiments, this minimizes background signal and radiation dose on healthy organs. In therapy, a fast clearance guarantees fast elimination of the drug, thus minimizing off-target side effects. Noteworthy, circulation time should be sufficient to enable the click reaction to occur in the site of action, in our case the tumor.

We decided to synthesize small-sized, hydrophilic, boron doped carbon dots. With that aim, a microwave vessel was loaded with citric acid (1 eq.), ethylenediamine (10 eq.), sodium tetraborate (borax, 3 eq.) and water. The synthesis was carried out in 5 min under microwave heating at 220 °C, 200 W and 370 PSI (Figure 2). Purification was performed by sephadex size exclusion column (NAP5® GE Healthcare), and the collected fractions were lyophilized to obtain a beige solid (Figure 3, left) which was analyzed in terms of chemical composition, size, shape and fluorescence properties.
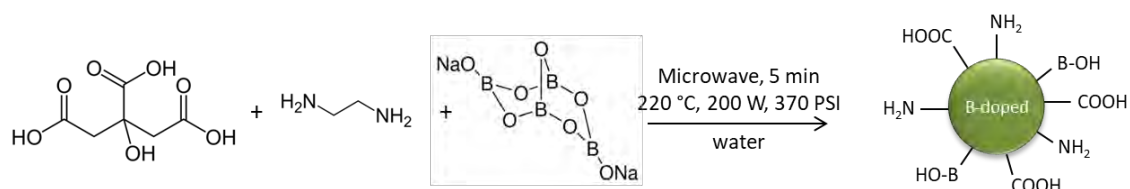

Figure 2: Schematic representation of the synthesis of hydrophilic B-CDs under microwave heating.

A typical characteristic, which can be used as first indication of a successful synthesis of B-CDs, is their intense fluorescence (Figure 3, right).
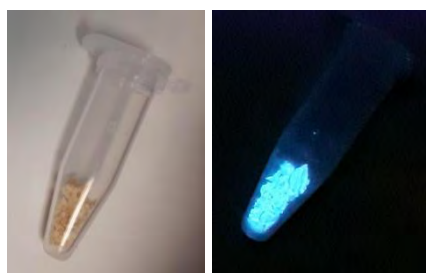

Figure 3: B-CDs after synthesis and lyophilization (left), under UV light (365 nm, right).

To determine if the obtained particles were homogeneous and to analyze their shape and size, Atomic Force Microscopy (AFM) analysis was performed. Images show spherical particles with a size distribution in diameter between 3 and 10 nm with an average of 6.7 ± 1.8 nm (Figure 4).
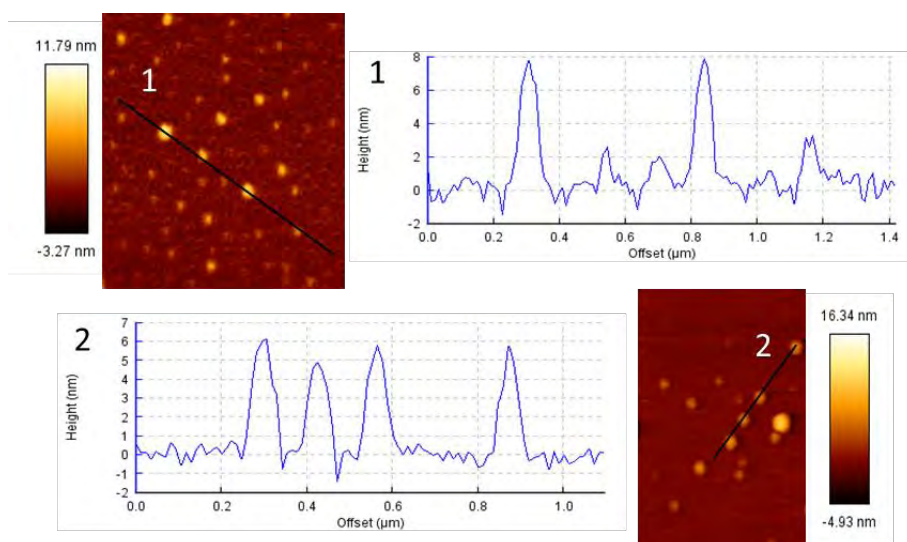
Figure 4: Representative AFM images to visualize shape and size of B-CDs with height profiles corresponding to lines shown in the images.

One critical aspect in BNCT is the amount of boron of the compound, which should be as high as possible to guarantee therapeutic efficacy. To analyze the content of the B-CDs, X-ray Photoelectron Spectroscopy (XPS) analysis was performed and the relative atomic percentage of the B-CDs was determined (Table 1). Carbon had with 44 at% the highest representation, followed by oxygen with 33 at%. The content of boron was 13 at%.

Table 1: Relative elemental composition of B-CDs in relative atomic percentage (at%).

C (at. %)	O (at. %)	N (at. %)	B (at. %)
44.0	33.1	9.9	13.0

Furthermore, XPS analysis of the B-CDs showed five peaks in the C-1s spectrum at 284.8, 286.0, 287.9, 288.8 and 282.8 eV which are attributed to the bonds of CC/CH, CO/CN, C=O, OC=C and CB, respectively. In the B-1s spectrum a peak at 192.1 eV, corresponding to BCO_2/BO bonds, and peaks at 188.1 and 189.8 eV, corresponding to BC and BN bonds, respectively, could be detected (Figure 5) (9; 10; 11). These results confirmed the presence of boron in the B-CDs.
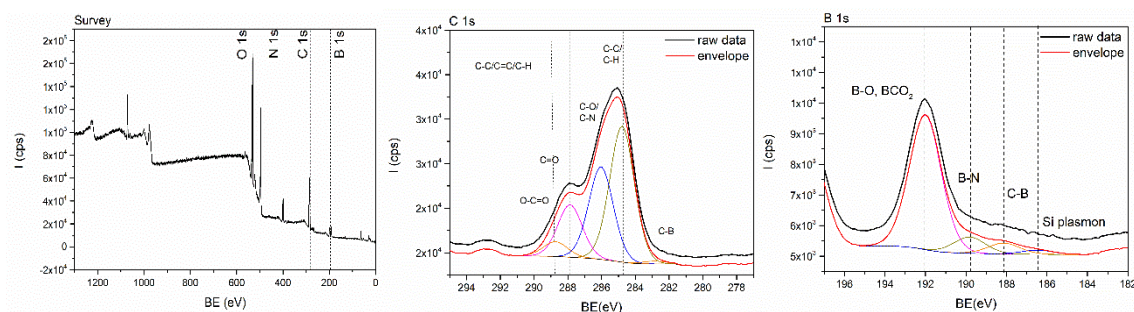

Figure 5: XPS high-resolution spectra of the survey, C-1s and B-1s of B-CDs.

Pre-targeting strategies require the presence of a moiety capable to undergo bioorthogonal reactions on both components. In our case, because the antibody (Trastuzumab) was functionalized with a TCO moiety (see chapter 4), we tackled the incorporation of a tetrazine moiety on the newly developed B-CDs. With that aim, a NHS ester of tetrazine (tetrazine-PEG$_5$-NHS) was used, allowing a coupling reaction to free existing amine groups on the B-CDs (Figure 6). The polyethylene glycol (PEG) linkage was chosen to increase the bio-compatibility, and to increase the size of the particles aiming at prolonging the blood circulation time (2).
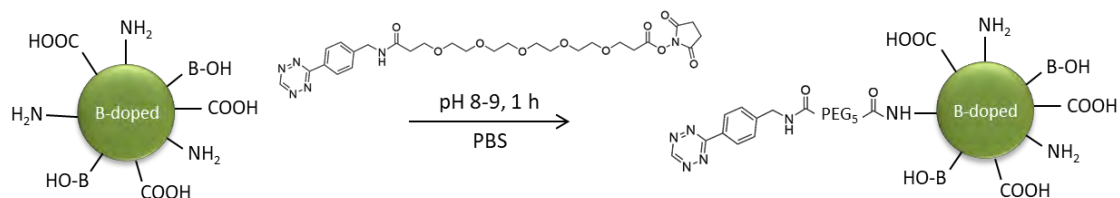

Figure 6: Schematic representation of the functionalization of B-CDs with tetrazine, enabling the pre-targeting approach.

To achieve functionalization, a solution of B-CDs in PBS (phosphate buffered saline, pH 7.4) was prepared. The obtained pH was around 9 and Tz-PEG$_5$-NHS was added without further adjustment of the pH. After incubation for a minimum of 1h, purification was performed by sephadex size exclusion column (NAP5® G-25 GE Healthcare) and the collected fractions lyophilized. However, the purification of the tetrazine functionalized B-CDs was challenging. The purification by NAP5® column was limited to very few fractions as the majority of the dots co-eluted with the excess of unbound Tz-PEG$_5$-NHS, as determined by high-performance liquid chromatography (HPLC, see below). A yield of only around 10 % pure B-CDs-Tz could be achieved.

An alternative method commonly used in the synthesis of CDs is dialysis. However, by using Float-a-Lyzer®G2 (MWCO: 500-1000 Da) only incomplete purification after 3 days in MQ water could be achieved. In view of these results, we settled with the low yield but high purity obtained after NAP5® column.

As mentioned above, to monitor the purification of tetrazine functionalized B-CDs (B-CDs-Tz) after the tetrazine coupling, HPLC was performed. Therefore, a size exclusion column (TSKgel SuperOligo PW, 150x6 mm, 3 μm) was used as stationary phase and eluted with 0.1 M ammonium formate (AMF, pH = 6) as the mobile phase (UV detection at 280 nm). Injection of naked B-CDs resulted in a broad signal including several peaks, with a main signal between 4.8 and 7 min (Figure 7 A). The little defined signal can be explained by the disparity of the B-CDs, containing different sized particles as shown by AFM. Moving to the functionalized B-CDs-Tz the main signal shifted towards 10 to 12 min. This result is quite surprising, as one may expect that attachment of the tetrazine moieties results in an increase in the particle size. This unexpected result could be explained because the attachment of the tetrazine moieties on the surface of the B-CDs not only induces a change in size (which is not expected to be very significant), but also a modification in the hydrophobicity of the particles. Hence, the longer retention of the functionalized B-CDs in the column could be explained by stronger interactions with the stationary phase, which result in a counter-

intuitive elution profile. Noteworthy, the presence of peaks with retention times in the range 5-9 min suggest that a fraction of the B-CDs remain non-functionalized (Figure 7 B), or present a low degree of functionalization.
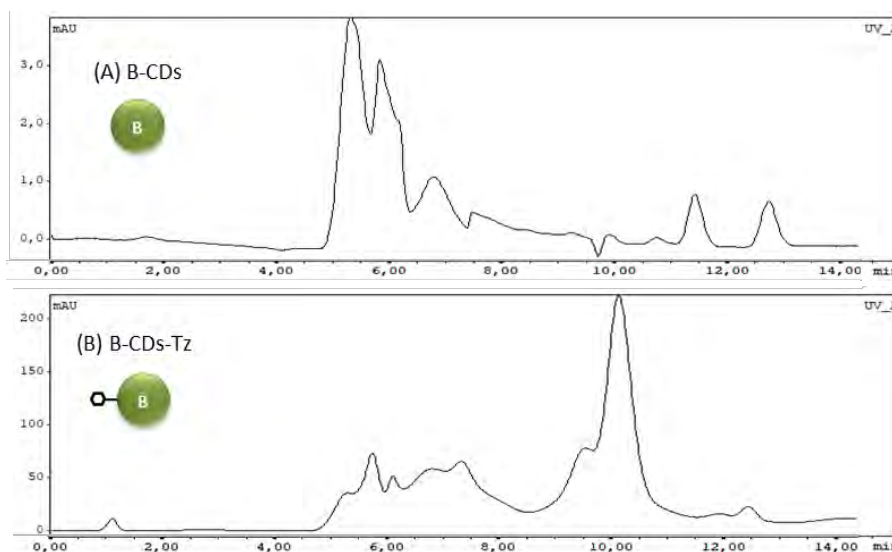

Figure 7: HPLC chromatograms representing naked B-CDs (A) and B-CDs-Tz after functionalization and purification (B).

The characterization of the fluorescent properties of the B-CDs was next tackled. The fluorescence spectra at various excitations were obtained for both B-CDs and B-CDs-Tz. The highest fluorescence intensity for the naked B-CDs was achieved with the excitation wavelength of 350 nm, while for B-CDs-Tz was achieved at 360 nm. Even though the shift for optimal excitation is small, an immense reduction of fluorescence to about $1/10^{th}$ could be observed as a result of the functionalization (Figure 8).
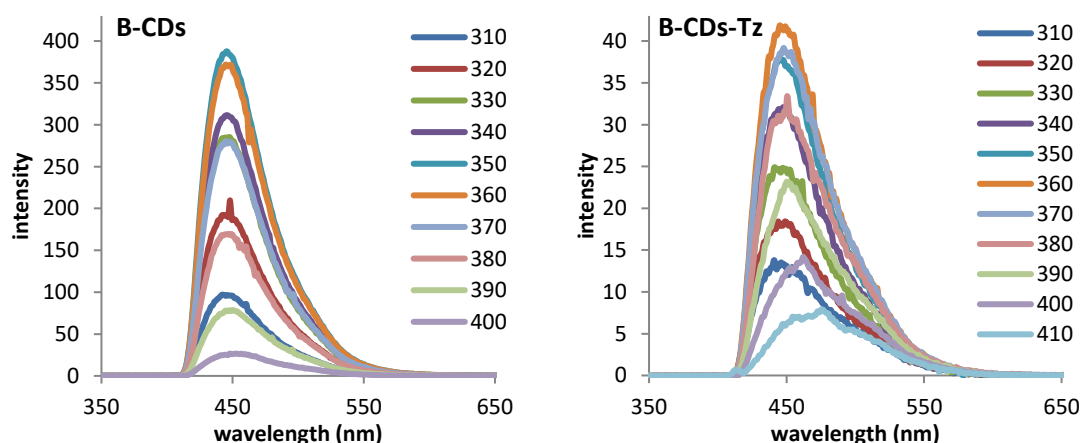

Figure 8: Emission spectra at different excitation wavelengths (310-410 nm) of B-CDs (left) and B-CDs-Tz (right).

To further analyze the impact of tetrazine functionalization on fluorescence properties, agarose gel electrophoresis was performed and analyzed using the Gel Doc™ EZ Imager (BIO-RAD) in UV mode. The reduced fluorescence after tetrazine attachment could be observed (Figure 9). Furthermore, when coupling a fluorophore (Cy3-TCO) via click

reaction to tetrazine, an increase in fluorescence proved the availability of tetrazine on the surface of B-CDs-Tz and its capacity to react with TCO moieties (Figure 9). The drawn-out distribution of the dots on the gel represents the variety of size which was already visible after AFM analysis (Figure 4).
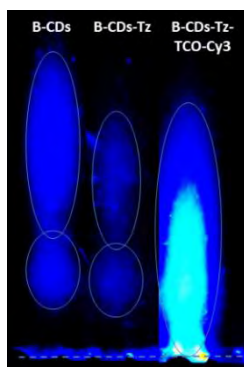

Figure 9: Agarose gel electrophoresis of B-CDs, B-CDs-Tz and B-CDs-Tz coupled to the fluorophore TCO-Cy3 and imaged using the Gel Doc™ imager in UV mode.

Finally, the bio-compatibility of the B-CDs-Tz was evaluated by cytotoxicity studies on BT-474 breast cancer cells. The cells were incubated with B-CDs-Tz of up to 160 µg/mL and to 72 h. Analysis by standard MTT assay showed, with cell survivals over 90 %, no induced cell death due to the particles in BT-474 cells, indicating negligible cytotoxicity (Figure 10).
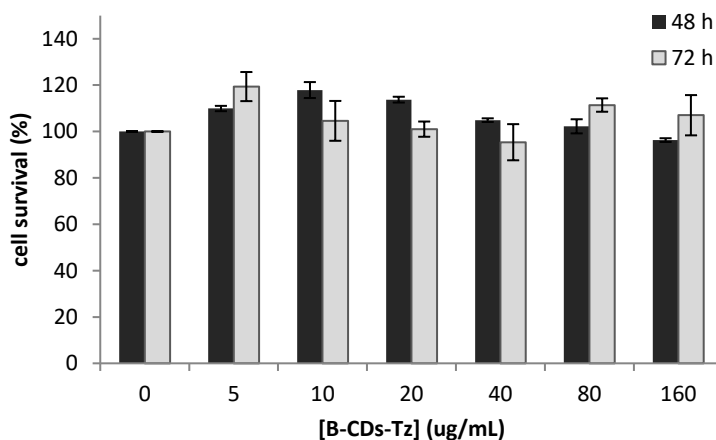

Figure 10: Cell viability in the presence of B-CDs-Tz for 48 h and 72 h on BT-474 breast cancer cell line; cells were incubated with increasing concentrations of the B-CDs-Tz and cell viability was determined by MTT assay (values are expressed as mean ± standard error mean, n = 3).

To evaluate the behavior of B-CDs-Tz with BT-474 breast cancer cells in terms of internalization, fluorescence microscopy studies were carried out. As the dots are fluorescence by themselves, a first trial was carried out without additional labeling. However, due to the reduced fluorophore-intensity after tetrazine attachment, the fluorescence wasn't sufficient for the studies. Hence, further trials were conducted by attaching Cy3-TCO via click reaction to tetrazine of the B-CDs-Tz. The cells themselves were stained for the nucleus and lysosomes with Hoechst33342 and Lysotracker-deep-red, respectively. Images were taken using a live cell Axio Observer fluorescence microscope (Zeiss) and analyzed by the

ZEN-ZEISS software. After 2 h incubation at 37 °C, co-localization between the dots and the lysosomes was observed, confirming internalization of B-CDs-Tz (Figure 11).
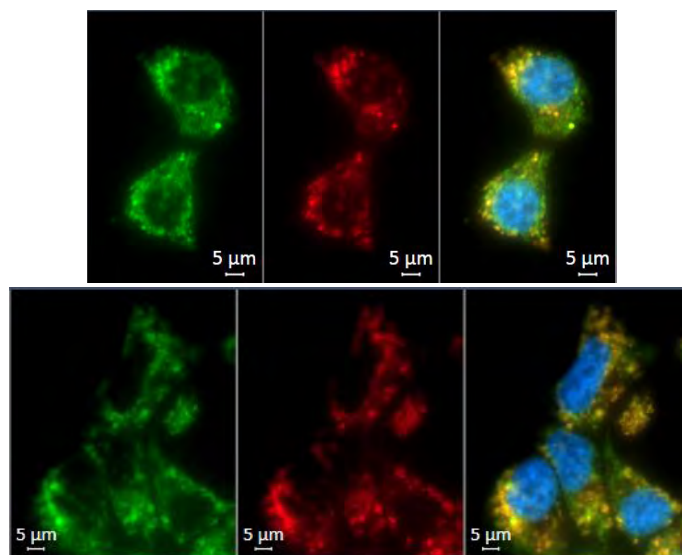

Figure 11: Representative images by live cell fluorescence microscopy of functionalized B-CDs-Tz after 2 h incubation. In green: B-CDs-Tz, fluorophore-labeled with TCO-Cy3; in red: Lysosomes, stained with Lysotracker-deep-red; in blue: nucleus, stained with Hoechst33342. Merged signals of B-CDs-Tz colocalizing with lysosomes appear in yellow.

Cell uptake is a desired property for boron delivery agents, as the efficacy and selectivity of the treatment improves in case of proximity of boron to the nucleus. For the pre-targeting strategy, a co-internalization of the antibody-dots complex is favored. Yet, it can be expected that the click reaction between the mAb-TCO and the B-CDs-Tz is faster than the cell uptake of the particles alone, hence no restrictions were expected for pre-targeting due to the ability of the dots to internalize. Additionally, internalization of the dots without interacting with the antibody should also not result in decreased efficacy, and can be considered as a parallel uptake mechanism that contributes to accumulation of the boron atoms in the interior of the cells.

To proof the occurrence of the click reaction between TCO-functionalized Trastuzumab and the B-CDs-Tz, HPLC analysis was performed. The same conditions as described above were used, with 0.1 M ammonium formate (pH = 6) as mobile phase on a size exclusion column (TSKgel SuperOligo PW, 150x6 mm, 3 μm). Chromatograms of mixtures in different ratios of the two pre-targeting components and respective controls were executed. As control, each component was injected alone (Figure 12, A-C: Trastuzumab without and with TCO and B-CDs-Tz). Furthermore a mix between non-functionalized Trastuzumab and B-CDs-Tz (Figure 12, D) was also injected as control; an almost separation could be achieved. When applying the mixture of Trastuzumab-TCO and B-CDs-Tz (Figure 12, E-G) a shift of the signal corresponding to the dots towards the mAb could be observed, this signal increasing with higher mAb-TCO/B-CDs-Tz ratios. These results confirm that the click reaction takes place. The fact that the signal of the B-CDs-Tz between 5 - 9 min is still visible with the high ratio of 50:1 (Figure 12, G), whereas the signal at min 9 - 12 disappeared, correlates with the assumption made above, that the dots eluted in this area are non-functionalized or only with low degrees (Figure 7).
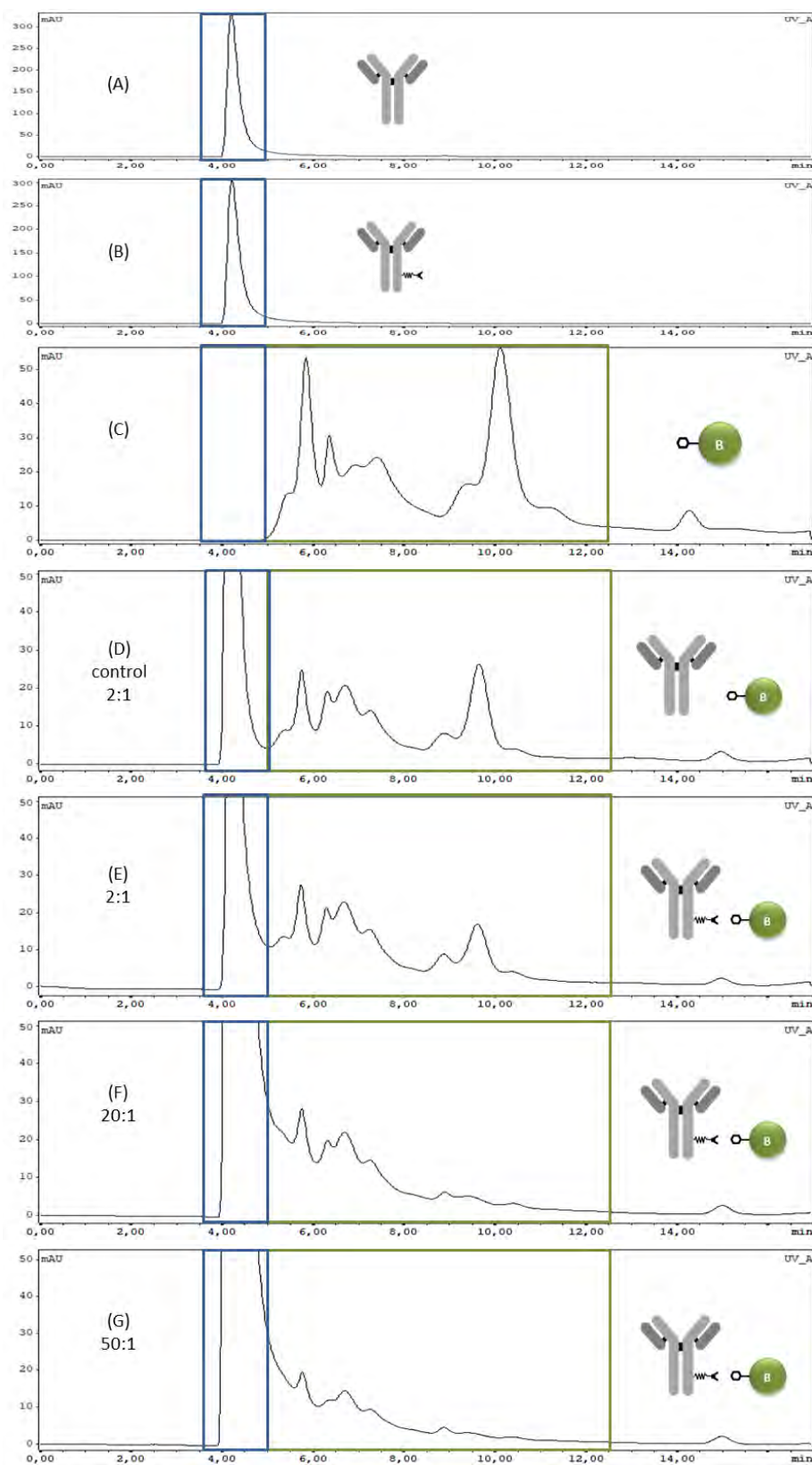
Figure 12: HPLC chromatograms to demonstrate occurance of click reaction between Trastuzumab-TCO and B-CDs-Tz including control chromatograms. (A) Trastuzumab, (B) Trastuzumab-TCO, (C) B-CDs-Tz, (D) control of non-functionalized Trastuzumab and B-CDs-Tz in a ratio of 2:1, (E-G) Trastuzumab-TCO and B-CDs-Tz in a ratio of (E) 2:1, (F) 20:1, (G) 50:1.

After the successful synthesis and functionalization of the B-CDs-Tz, including their characterization and confirmation of bio-compatibility and successful click reaction between the two pre-targeting components, we moved to the *in vivo* evaluation of pre-targeting. Hence, radiolabeling of the B-CDs-Tz with a positron emitting nuclide was necessary to be able to follow the dots after administration to mice by positron emission tomography (PET) imaging.
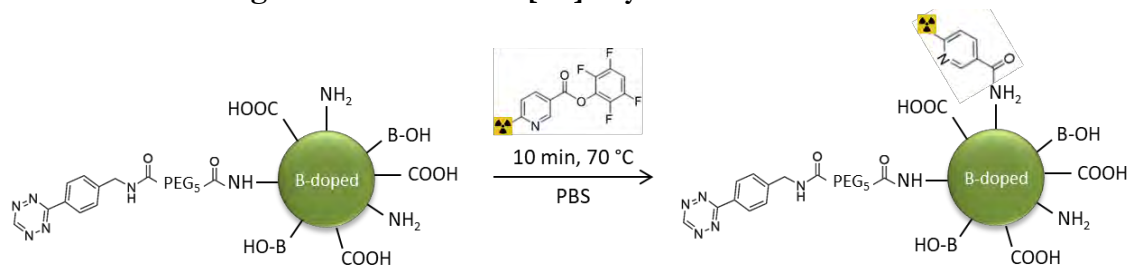
5.3.2 Radiolabeling of B-CDs-Tz with [^{18}F]FPyTFP

Figure 13: Schematic representation of radiolabeling B-CD-Tz with [^{18}F]FPyTFP.

To radiolabel the dots, the radionuclide fluorine-18 ($t_{1/2}$ = 109.77 min) was chosen, as relatively fast clearance was expected due to their small size. An easy and mild route to label biomolecules or nanoparticles with ^{18}F is by using a prosthetic group, which is a small molecule that incorporates the radionuclide and has a functional group for fast and easy coupling to the (usually) bigger component. With free available amine groups on the surface of the B-CDs-Tz and with an automatized system for its production in hand, the prosthetic group [^{18}F]FPyTFP (12) was chosen (see **Error! Reference source not found.** for synthesis of [^{18}F]FPyTFP precursor and Radiosynthesis of [^{18}F]FPyTFP). Therefore B-CDs-Tz were dissolved in PBS, the prosthetic group added and incubated for 10 min at 70 °C. The labeling was monitored by: (i) radio-TLC using silica gel coated aluminum sheets and methanol/dichloromethane 3:7 as the stationary and mobile phases, respectively (Figure 14); and (ii) by radio-HPLC using the size exclusion column (TSKgel SuperOligo PW, 150x6 mm, 3 μm) as stationary phase, and 80 % 0.1 M ammonium formate (AMF, pH = 6) and 20 % acetonitrile, to enable elution of the prosthetic group, as the mobile phase (UV detection at 365 nm) (Figure 15). Both methods confirmed quantitative labeling of the dots.
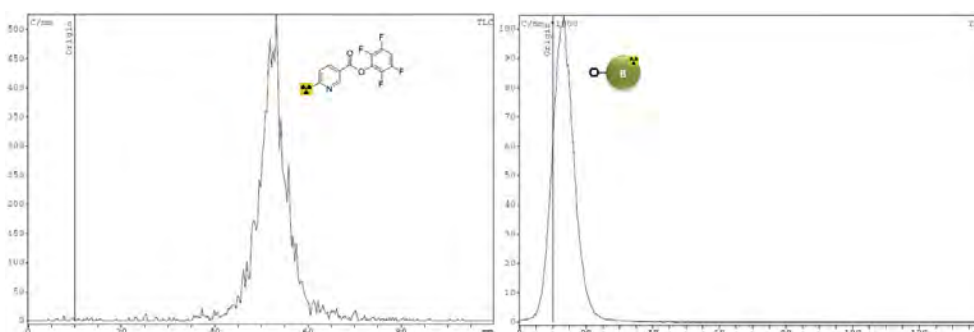

Figure 14: Chromatograms of radio-TLCs monitoring of the radiolabeling reaction of B-CDs-Tz with [^{18}F]FPyTFP. Left: [^{18}F]FPyTFP as control, right: [^{18}F]B-CDs-Tz after labeling was complete.
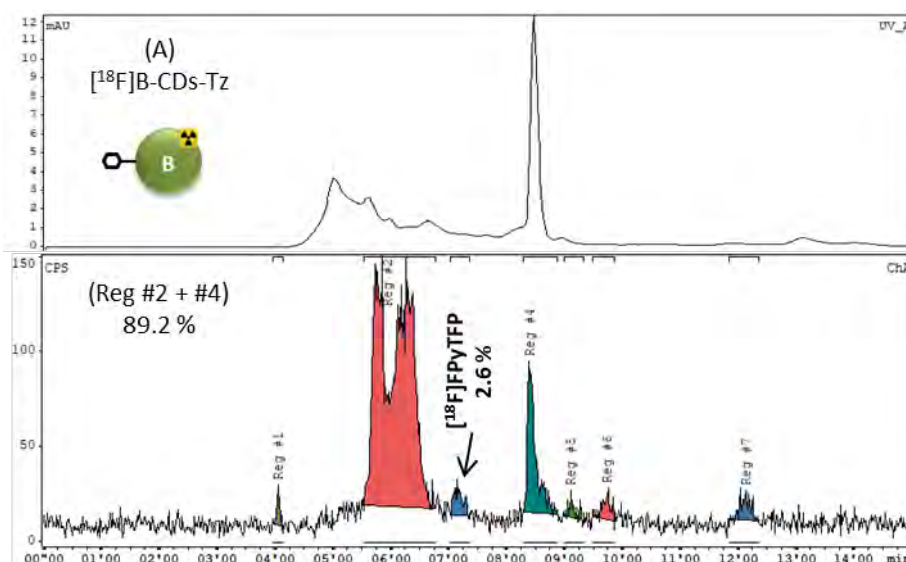
Figure 15: Radio-HPLC chromatogram of [18F]B-CDs-Tz. Top: UV detection, bottom: radiometric detection.

5.3.3 Pre-targeting B-CDs *in vivo*

For the evaluation of pre-targeting B-CDs *in vivo*, BT-474 breast cancer xenograft bearing NOD/SCID mice were used (for details about tumor growth see Chapter 4). Two experimental groups were evaluated; the pre-targeting group (G1), in which TCO-functionalized Trastuzumab was injected intravenously 24 h prior to the intravenous administration of [18F]B-CDs-Tz and a control group (G2) in which solely [18F]B-CDs-Tz were injected intravenously (Figure 16). Each group consisted of 3 animals. The amount of injected mAb per mouse was of 100 μg. For both groups 200-300 μCi (7.5 - 11.0 MBq) [18F]B-CDs-Tz were injected per mouse, corresponding to about 150-250 μg. Dynamic PET-CT scans were performed immediately after injection of the B-CDs for 45 min using an eXploreVista-CT small animal PET-CT system (GE Healthcare).
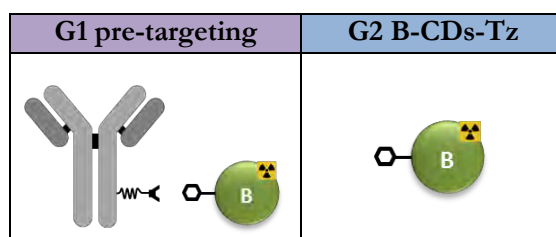
Figure 16: Experimental set up with two experimental groups for *in vivo* evaluation of pre-targeting B-CDs. The pre-targeting group (G1) was injected with Trastuzumab-TCO followed by [18F]B-CDs-Tz after 24 h; the second group (G2) received only [18F]B-CDs-Tz.

To visualize the results after PET quantification with PMOD software the 45 min scans were averaged in 5 timeframes. First, we looked at the biodistribution profile and plotted the uptake in major organs. A fast clearance by elimination through kidneys and bladder could be observed, which was very similar for both groups (Figure 17 and Figure 18).
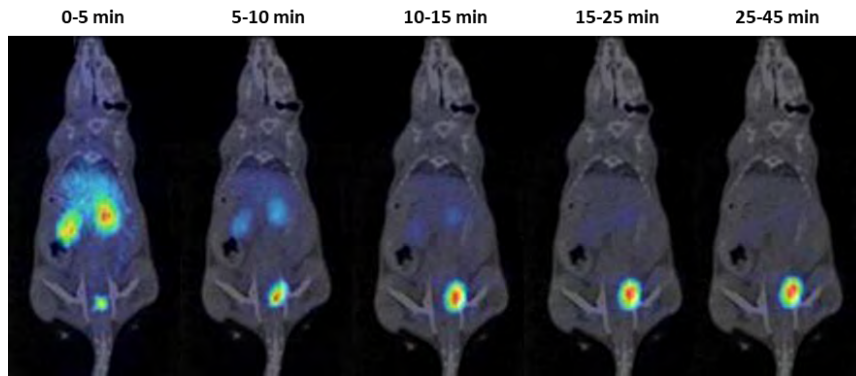
Figure 17: Representative coronal PET images for each time frame (average of each timeframe) after intravenous administration of [^{18}F]B-CDs-Tz. PET images have been co-registered with CT images (representative slice) for localization of the radioactive signal.
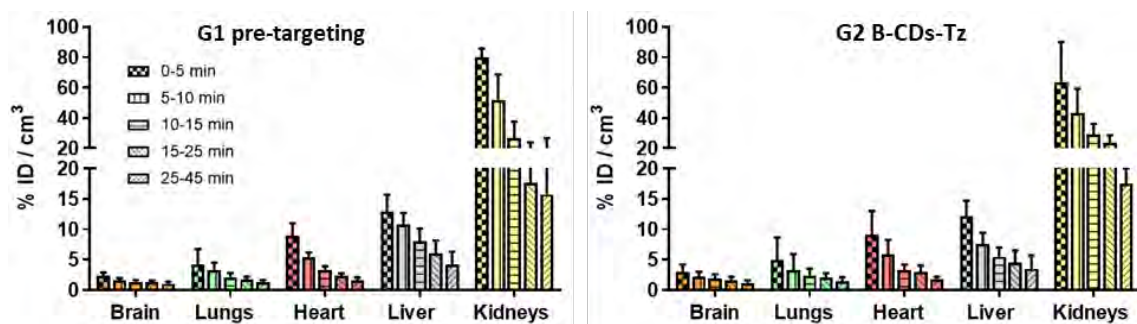
Figure 18: Accumulation of [^{18}F]B-CDs-Tz in different organs at 5 timeframes up to 45 min after intravenous administration, analyzed by PET imaging, obtained for the pre-targeting and control group (values are expressed as mean ± standard error mean, n = 3).

However, a closer look to the tumor uptake revealed clear differences. In G2 the [^{18}F]B-CDs-Tz are washed out from the tumor, whereas the amount of dots in the pre-targeted tumors seems to be stable which lead to the conclusion that the desired retention of the dots was achieved. Further verification was given by the significant difference in the time frame 25–45 min (P = 0.0005) (Figure 19).
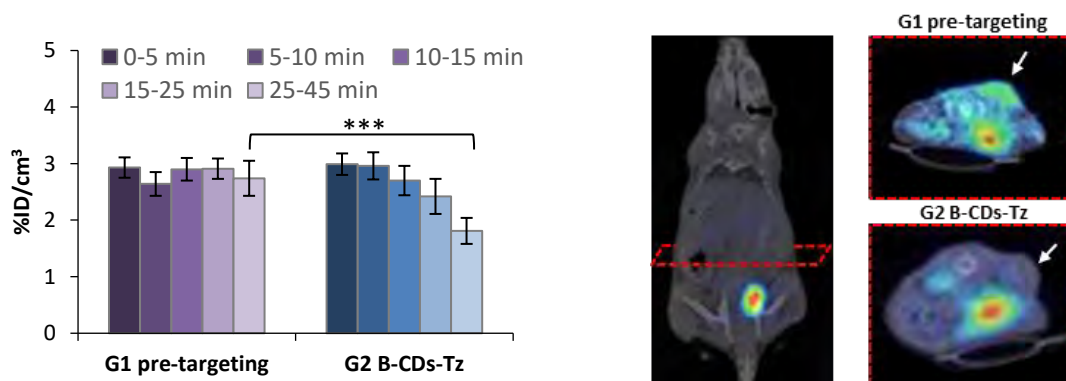
Figure 19: Left: Accumulation of [^{18}F]B-CDs-Tz in the tumor, analyzed by PET imaging, at different timeframes after intravenous administration for the pre-targeting and control group (values are expressed as mean ± standard error mean, n = 3). Significant differences are found in the time frame 25–45 min (P = 0.0005). Right: representative axial slices in the region of the tumor corresponding to PET-CT images obtained after administration of [^{18}F]B-CDs-Tz in the time frame 25-45 min for the pre-targeting and control group.

The results obtained confirm the effect of the pre-targeting strategy in terms of tumor retention. However, higher accumulation in the tumor would be desirable. This could be achieved by using a slower- or non-internalizing mAb which results in higher availability of the mAb at tumor site. Furthermore, it would allow a later administration of the B-CDs to achieve enhanced clearing of the mAb from non-targeted tissue. Finally, an increase of the circulation time of the CDs could enhance tumor accumulation.

5.4 Summary and conclusion

This chapter describes the successful approach of pre-targeting boron carbon dots (B-CDs) for the application in BCNT. The particles were successfully synthesized using a one-step microwave method, characterized among other by AFM, XPS and for their fluorescence, functionalized with tetrazine and radiolabeled with the prosthetic group [^{18}F]FPyTFP which finally resulted in their evaluation *in vivo* in BT-474 breast cancer xenograft bearing NOD/SCID mice. Bio-compatibility was confirmed prior performing an MTT cytotoxicity test.

The biodistribution of the B-CDs showed a rapid clearance over kidneys and bladder from blood, organs and tissue, including the tumor. However, in pre-targeted tumors a clear retention of the dots could be found, hence, the B-CDs-Tz clicked to the TCO-functionalized mAb in tumor tissue, preventing the wash out as seen in the control group.

Yet, low accumulation in tumor of, in average, only 2.8 ± 0.2 %ID/cm^3 (which maintained almost the same over the 45 min PET scan) was observed. To obtain a higher tumor uptake and therefore higher boron concentrations in the tumor, necessary for a successful BNCT approach, a slow- or non-internalizing mAb should be used. It would allow a longer mAb clearing time before the injection of the B-CDs (e.g. from 24 h to 48 h) as well as an increase of available mAb on the cell membrane at tumor site.

Nevertheless, the results of this chapter clearly show the desired retention of the boron delivery agent, the B-CDs, due to pre-targeting. Hence, B-CDs, combined with a pre-targeting strategy, are promising new BCNT agents!

5.5 Experimental part

5.5.1 Reagents

All reagents were obtained from Sigma-Aldrich unless otherwise stated. Milli-Q water (resistivity 18.2 MΩ·cm at 25 °C) was used in all experiments. NHS-Cy3 was purchased from BroadPharm. The antibody Trastuzumab was purchased from Roche Farma, S.A. España. A stock of BT-474 cells was kindly donated by Instituto de Investigación Sanitaria Biodonostia (San Sebastián, Spain). Animals were purchased from Charles River Laboratories France.

$[^{18}F]$ was generated in an IBA Cyclone 18/9 cyclotron by irradiation of $[^{18}O]H_2O$ with high energy (18 MeV) protons via (p, n) reaction, and trapped on a QMA cartridge and the activity eluted with aqueous K_2CO_3.

5.5.2 Instrumentation

The synthesis of B-CDs was performed using a CEM Focused Microwave™ Synthesis System, Discover® SP.

Atomic force microscopy (AFM) studies were performed using a Veeco Multimode AFM attached to a Nanoscope V controller. The sample was imaged in tapping mode in air, using TESPA-V2 doped silicon probe with $k = 42$ N/m. A drop of a diluted solution of the particles was placed on a glass substrate, the sample left to evaporate at room temperature and afterwards imaged.

X-ray Photoelectron Spectroscopy (XPS) experiments were performed in a SPECS Sage HR 100 spectrometer (Berlin, Germany) with a non-monochromatic X ray source (aluminum Kαline of 1486.6 eV energy and 252 W), placed perpendicular to the analyzer axis and calibrated using the 3d5/2 line of Ag with a full width at half maximum (FWHM) of 1.1 eV. The selected resolution for the spectra was 15 eV of Pass Energy and 0.15 eV/step. All measurements were made in an ultra-high vacuum (UHV) chamber at a pressure around $6×10^{-8}$ mbar. An electron flood gun was used for charge neutralization. Gaussian Lorentzian functions were used for fittings (after a Shirley background correction) where the FWHM of all the peaks were constrained while the peak positions and areas were set free. Main C1s peak was used for charge reference and set at 284.8 eV.

HPLC analysis was carried out using an Agilent 1200 series HPLC equipped with a quaternary pump, a multiple wavelength detector and a radiometric detector (Gabi, Raytest). A size exclusion column (TSKgel SuperOligo PW, 150x6 mm, 3 μm) was used as stationary phase with 100 % 0.1 M ammonium formate (AMF, pH = 6) or for radio-HPLC with 80 % 0.1 M AMF and 20 % acetonitrile as mobile phase at a flow rate of 0.4 mL/min. UV detection at λ = 280 nm or, for radio-HPLC at 365 nm. Injection volume was 20 μL.

Fluorescence spectra were measured at room temperature using a Perkin Elmer (LS 55) Fluorimeter. Excitation source: Pulsed Xenon lamp 8 W, Detector: PMT (200-650 nm), Polarizers anisotropy / polarisation measurements, Emission monochromator cut off filter set: 290, 350, 390, 430 y 515 nm, attenuator 1% T, FL-WinLab software for data acquisition and analysis.

Cell observer microscopy experiments were carried out using a Zeiss Axio Observer Fluorescence microscope using Ibidi clear bottomed μ-slide 8-well microscopy plates and analyzed by ZEN2012-ZEISS.

Successful preparation of synthetic products was confirmed by NMR spectroscopy. NMR spectra of $CDCl_3$ or acetonitrile-d_3 solutions were recorded on Bruker Avance III 500 MHz spectrometer at 302 K. The chemical shifts (δ) are reported in *parts per million* (*ppm*) and are referenced to the deuterated solvent used. The coupling constants (*J*) are reported in Hz, and the splitting patterns are indicated as s (singlet), d (doublet), dd (doublet of doublets), t (triplet), and tt (triplet of triplets).

Radio-thin layer chromatography (radio-TLC) was performed using silica gel coated aluminum sheets and methanol/dichloromethane 3:7 as the stationary and mobile phases, respectively. TLC plates were analyzed using a TLC-reader (MiniGITA, Raytest).

PET experiments were performed using an eXploreVista-CT small animal PET-CT system (GE Healthcare). Anesthesia was induced with 3-5 % isoflurane and maintained by 1.5-2 % of isoflurane in 100% O_2.

5.5.3 Tumor growth

Cells
BT-474 cells were cultured in DMEM medium (100X, 10378-016 Gibco; 10 % fetal bovine serum, 1 % penicillin-streptomycin) at 37 °C with 5% CO_2 in a humid atmosphere. Cells were confirmed, using a Lonza Mycoplasma test, to be free of mycoplasma contamination.

Animals
All animal experiments were performed in accordance with the Spanish policy for animal protection (RD53/2013), which meets the requirements of the European Union directive 2010/63/UE regarding the protection of animals used in experimental procedures. All experimental procedures were approved by the Ethical Committee of CIC biomaGUNE and authorized by the local authorities. All animals were housed in ventilated cages and fed on a standard diet *ad libitum*. The studies were performed on female NOD.CB17-Prkdcscid/J mice.

Tumor growth
To grow BT-474 cell line breast cancer xenografts on female NOD.CB17-Prkdcscid/J mice 5-6 weeks old mice were operated to implant a 17β-estradiol pellet (belma technologies) subcutaneously at their neck. The next day $10*10^6$ BT-474 tumor cells were inoculated per animal subcutaneously at the flank of the mouse. Prior to each inoculation cells were diluted in sterile PBS:Matrigel (1:1). The sizes of the tumors were measured every 2-3 days with a digital calliper and volumes calculated ($V = \frac{\text{short diameter}^2 * \text{long diameter}}{2}$). At the time the tumour reached 200-300 mm^3 (around 2 weeks after inoculation) *in vivo* studies could be performed. The defined human endpoints were: (i) weight loss greater than 20 % in one week, (ii) one or more of the following clinical signs: abdominal distension, dyspnoea, cachexia or stooping, (iii) the absence of response to stimuli and lethargy, (iv) a tumor larger

than 1.5 cm in average diameter and (v) ulcerated or necrotic tumors or wounds / aggressions severe infected.

5.5.4 Chemistry and Radiochemistry

Conjugation of TCO-NHS to Trastuzumab
The antibody Trastuzumab was diluted in PBS (phosphate-buffered saline, pH 7.4) to a concentration of 3.0 mg/mL. The pH was adjusted to 8.6 – 9.1 with 0.1 M Na_2CO_3. 50-55 moles eq. TCO-NHS (20 mM in DMSO) was added. After incubation (120 min, RT) non-reacted TCO-NHS was removed by spin filtration (100 kDa, 12000 rpm) and the conjugated mAb washed three times with PBS. After recovering the mAb from the filter with PBS its concentration was determined by NanoDrop®.

Synthesis of B-CDs and functionalization with tetrazine
To a 10 mL microwave vessel were added citric acid monohydrate (1 eq., 18.0 mg), ethylendiamine (10 eq., 57.0 μL), sodium tetraborate (3 eq., 51.7 mg) and 300 μL MQ water. The vial was capped and introduced into the microwave. The reaction was performed in 5 min with stirring at 220 °C, 200 W, 370 PSI and with 2 min ramp time. Purification was performed by sephadex size exclusion column (NAP5® GE Healthcare) and the collected fractions lyophilized. To attach tetrazine 6 mg B-CDs were dissolved in 500 μL PBS. The solution had a pH around 9 and Tz-PEG$_5$-NHS (1.6 mg in 30 μL DMSO, 110 mM) was added without further adjustment of the pH. After incubation overnight purification was performed by sephadex size exclusion column (NAP5® GE Healthcare) and the collected fractions lyophilized. A yield of 12.4 % of pure B-CDs-Tz could be achieved.

Agarose (1.5 %) gel electrophoresis
A 1.5 % agarose gel was prepared following standard protocol. In brief 1.5 g agarose were suspended in 100 mL Tris-Borate-EDTA (TBE) buffer and heated until it almost reached its boiling point. The solution was poured in a gel chamber, the comb placed and let settle to polymerize. Samples were prepared in 20 μL aqueous batches, including 5 μL loading buffer. 10 μL were loaded on the gel and run for approximately 1 h at 100 V.

Proof of click reaction using SE-HPLC
To proof the occurrence of the click reaction between TCO-functionalized Trastuzumab and the B-CDs-Tz, SE-HPLC analysis was performed. Therefore, a size exclusion column (TSKgel SuperOligo PW, 150x6 mm, 3 μm) was used as stationary phase with an isocratic mobile phase of 0.1 M ammonium formate (pH = 6). Chromatograms were first executed for controls of each component alone (non-functionalized Trastuzumab (2 mg/mL), TCO-functionalized Trastuzumab (2 mg/mL) and B-CDs-Tz (1 mg/mL)) as well as a mix of non-functionalized Trastuzumab (1 mg/mL) and B-CDs-Tz (1 mg/mL) in a ratio of 2:1. Finally, chromatograms of the two pre-targeting components combined in different ratios were executed (functionalized Trastuzumab (1 mg/mL) and B-CDs-Tz (1 mg/mL) in ratios of 2:1, 20:1, 50:1).

Synthesis of [^{18}F]FPyTFP precursor 4
The precursor for the preparation of [^{18}F]FPyTFP was synthesized in a 3-step sequence as described previously (12). In brief, a solution of 6-chloronicotinic acid (900 mg, 5.7 mmol),

2,3,5,6-tetrafluorophenol (750 mg, 4.5 mmol) and N,N'-dicyclohexylcarbodiimide (1.9 g, 9 mmol) in dioxane (40 mL) was stirred at room temperature for 2 h. The mixture was filtered, the solvent evaporated, and the crude crystallized from hot hexane (25 mL), to give 6-chloronicotinic acid 2,3,5,6-tetrafluorophenyl ester (945 mg, 3.1 mmol; 69 %) as a white solid.

^{1}H NMR (500 MHz, Chloroform-d) δ 9.21 (dd, J = 2.4, 0.8 Hz, 1H), 8.42 (dd, J = 8.4, 2.4 Hz, 1H), 7.57 (dd, J = 8.4, 0.8 Hz, 1H), 7.11 (tt, J = 9.8, 7.0 Hz, 1H) (matches the literature data).

Nicotinic ester (760 mg, 2.5 mmol) was dissolved in trimethylamine solution in tetrahydrofurane (1 M, 20 mL) and stirred at room temperature for 5 h. The white precipitate was collected by vacuum filtration and washed with diethyl ether (2 × 5 mL) to obtain N,N,N-trimethyl-5-((2,3,5,6-tetrafluorophenoxy)carbonyl)pyridin-2-aminium chloride (605 mg, 1.7 mmol; 68 %) as an off-white solid. This was suspended in trimethylsilyl triflate solution in dichloromethane (2 % w/w, 25 mL). The mixture was exposed to ultrasound for 10 min, the solvent was evaporated and the crude washed with diethyl ether (2 × 10 mL) to give N,N,N-trimethyl-5-((2,3,5,6-tetrafluorophenoxy)carbonyl)pyridin-2-aminium trifluoro-methanesulfonate (792 mg, 1.7 mmol; 100 %) as an off-white solid.

^{1}H NMR (500 MHz, Acetonitrile-d3) δ 9.28 (d, J = 2.3 Hz, 1H), 8.79 (dd, J = 8.7, 2.3 Hz, 1H), 8.01 (d, J = 8.8 Hz, 1H), 7.37 (tt, J = 10.5, 7.3 Hz, 1H), 3.54 (s, 9H) (matches the literature data).

Radiosynthesis of [^{18}F]FPyTFP

The synthesis of [^{18}F]FPyTFP was performed using a TRACERlab FXFN synthesis module (GE Healthcare) by ^{18}F-fluorination of the trifluoromethanesulfonate precursor, inspired by previously described procedure (12). The radiosynthesis was carried out in a fully automated manner and included HPLC purification and reformulation.

Fluorine-18 (^{18}F) was generated in an IBA Cyclone 18/9 cyclotron by irradiation (target current = 44 μA) of ^{18}O-enriched water with high energy (18 MeV) protons via ^{18}O(p, n)18F reaction. [^{18}F]F$^-$ was trapped on a pre-conditioned Sep-Pak® Accell Plus QMA Light cartridge (Waters, Milford, MA, USA), and then eluted with a solution of Kryptofix K2.2.2/K2CO3 in a mixture of water and acetonitrile. After complete elimination of the solvent by azeotropic evaporation, a solution containing the precursor (10 mg) in a mixture of t-butanol and acetonitrile (4/1, v/v; 0.5 mL) was added and the mixture was kept at 40 °C for 15 min. The crude was diluted with acetonitrile/water (1/1, v/v; 2 mL) and purified by HPLC using RP Mediterranea Sea18 (10 × 250 mm, 5 μm particle size; Teknokroma, Spain) as a stationary phase and acetonitrile/0.1% TFA in milliQ water (80/20, v/v) as a mobile phase at a flow rate of 3 mL/min. The desired fraction (tR = 29–30 min) was collected, diluted with water (25 mL), and the radiotracer was retained on a C-18 cartridge (Sep-Pak® Light, Waters, Milford, MA, USA). The cartridge was washed with water (5 mL) and the radiotracer eluted with acetonitrile (1 mL). Chemical and radiochemical purity were determined by HPLC using a Mediterranean C18 column (4.6 x 150 mm, 5 μm) as stationary phase and 0.1% TFA/acetonitrile (0-1 min 25% acetonitrile; 9-12 min 90% acetonitrile; 13-15 min 25% acetonitrile) as the mobile phase at a flow rate of 1.5 mL/min (retention time = 23 min).

HPLC analysis confirmed high radiochemical purity (> 99 %) of [^{18}F]FPyTFP, obtained in 14 % non-decay corrected yield. For the purpose of further use of the radiolabeled prosthetic group, [^{18}F]FPyTFP was used dissolved in acetonitrile as obtained after elution from the cartridge.

Radiolabeling of B-CDs-Tz with [^{18}F]FPyTFP

To radiolabel B-CDs-Tz 1.2 mg were dissolved in 100 μL PBS (phosphate buffered saline, pH 7.4) and 8 mCi (300 MBq) [^{18}F]FPyTFP in acetonitrile added. After 10 min incubation at 70 ºC the labeling was complete as monitored by radio-TLC (silica gel 60 F254 on aluminum sheets (Merck), methanol/dichloromethane 3:7) and radio-HPLC (TSKgel SuperOligo PW column, 150x6 mm, 3 μm, 0.1 M AFM/acetonitrile 80:20).

5.5.5 *in vitro* studies

Cytotoxicity studies

To determine cell viability, BT-474 human breast cancer cells were incubated with functionalized B-CDs over 48 h and 72 h. Cells were seeded (3×10^4 cells/well, 100 μL/well, 96-well plate), allowed to adhere overnight in complete media and maintained in a humid atmosphere at 37 °C and 5 % CO_2. Then, media was removed and cells were left untreated (control) or incubated with the B-CDs-containing formulations, diluted accordingly in media. The experiments were performed in triplicates. After the desired time, cell supernatant was removed and 100 μL/well of MTT reagent (Roche), diluted in the corresponding media to the final concentration of 0.25 mg/mL, was added. After 1 h incubation at 37 °C and 5 % CO_2, the excess reagent was removed and formazan crystals were solubilized by adding 200 μL of DMSO per well. The optical density of each well was measured in a TECAN Genios Pro 96/384 microplate reader at 550 nm. Data was represented as the percentage of cell survival compared to control wells.

In vitro internalizing studies of B-CDs-Tz-Cy3

B-CDs-Tz were fluorophore-labelled with TCO-Cy3, using the click-coupling reaction and purified by sephadex size exclusion column (NAP5® GE Healthcare). BT-474 cells (ps. 17) were seeded in a poly-L-Lysine treated 'Ibidi' μ-slide 8-well-plate (30 000 cells/well in 0.3 mL) and incubated overnight to adhere (37 °C, 5% CO_2, humid atmosphere). The media was removed and 0.1 mL Hoechst 33342 (1 μg/mL medium) added to stain the nucleus. After 10 min incubation (37 °C, 5% CO_2, humid atmosphere) 0.1 mL LysoTracker deep red (1 μg/mL in media) was added to stain the lysosomes. After 20 min incubation (37 °C, 5% CO_2, humid atmosphere) media was removed and 0.3 mL of Cy3-labeled B-CDs (75 μg/mL medium) added. After 2 h incubation (37 °C, 5% CO_2, humid atmosphere) the media was removed and replaced with fresh media. The images were taken with a Cell Axio Observer Fluorescence Microscope. Controls of single staining for each fluorophore were included. Images were analyzed by ZEN-ZEISS software.

5.5.6 *in vivo* studies

In vivo PET imaging studies

Two groups of animals (n = 3) were selected out of female, BT-474 breast cancer xenograft bearing NOD/SCID mice. For the pre-targeting group approximately 100 μg of TCO

functionalized Trastuzumab (~2 TCO/mAb, determined by the direct method described in chapter 3) per mouse were injected intravenously via tail vein. 24 h post injection the [^{18}F]B-CDs-Tz (150-250 μg B-CDs-Tz in 100 μL PBS with 200-300 μCi (7.4-11.1 MBq) per mouse) were injected intravenously. The same amount of [^{18}F]B-CDs-Tz was injected to the second group which did not receive Trastuzumab beforehand. Imaging studies were conducted using positron emission tomography (PET) in combination with computerized tomography (CT), using an eXploreVista-CT small animal PET-CT system (GE Healthcare). Dynamic whole-body images (2 beds) were acquired immediately after injection for 45 min. PET images were analyzed using PMOD image analysis software (PMOD Technologies Ltd, Zürich, Switzerland).

5.6 References

1. *Microwave-assisted synthesis of carbon dots and their applications.* **Tayline V. de Medeiros, John Manioudakis, Farah Noun, Jun-Ray Macairan, Florence Victoriaab and Rafik Naccache.** 2019, J. Mater. Chem. C, pp. 7175-7195.

2. *Surface modification and chemical functionalization of carbon dots: a review.* **Zhou, Fanyong Yan & Yingxia Jiang & Xiaodong Sun & Zhangjun Bai & Yan Zhang & Xuguang.** 2018, Microchimica Acta - Springer, pp. 1-34.

3. *Synthesis-Modification Integration: One-Step Fabrication of Boronic Acid Functionalized Carbon Dots for Fluorescent Blood Sugar Sensing.* **Xia, Pengfei Shen and Yunsheng.** s.l. : American Chemical Society, 2014, Analytical Chemistry, Vol. 86, p. 5323−5329.

4. *B-doped carbon quantum dots as a sensitive fluorescence probe for hydrogen peroxide and glucose detection.* **Xiaoyue Shan, Lujing Chai, Juanjuan Ma, Zhaosheng Qian, Jianrong Chen and Hui Feng.** s.l. : The Royal Society of Chemistry, 2014, Analyst, Vol. 139, pp. 2322–2325.

5. *One-pot synthesis of boron and nitrogen co-doped carbon dots as the fluorescence probe for dopamine based on the redox reaction between Cr(VI) and dopamine.* **Tian Tian, Yu He, Yili Ge, Gongwu Song.** s.l. : Elsevier B.V., 2017, Sensors and Actuators B: Chemical, Vol. 240, pp. 1265–1271.

6. *N, B-doped carbon dots as a sensitive fluorescence probe for Hg^{2+} ions and 2,4,6-trinitrophenol detection for bioimaging.* **Qianghua Ye, Fanyong Yan, Dechao Shi, Tancheng Zheng, Yinyin Wang, Xuguang Zhou, Li Chena.** s.l. : Elsevier B.V., 2016, Journal of Photochemistry & Photobiology, B: Biology, Vol. 162 , pp. 1–13.

7. *Surrounding media sensitive photoluminescence of boron-doped graphene quantum dots for highly fluorescent dyed crystals, chemical sensing and bioimaging.* **Zetan Fan, Yunchao Li, Xiaohong Li, Louzhen Fan, Shixin Zhou, Decai Fang, Shihe Yang.** s.l. : Elsevier Ltd, 2014, CARBON, Vol. 70, pp. 149–156.

8. *Fluorescence quenchometric method for determination of ferric Fluorescence quenchometric method for determination of ferric.* **Lei, Fengxiang Wang & Qingli Hao & Yuehua Zhang & Yujuan Xu & Wu.** s.l. : Springer-Verlag Wien, 2015, Microchim Acta.

9. **John F. Moulder, William F. Stickle, Peter E. Sobol, Kenneth D. Bomben.** *Handbook of X ray Photoelectron Spectroscopy.* s.l. : Perkin-Elmer Corporation, Physical Electronics Division, 1995.

10. **Biesinger, M.C.** X-ray Photoelectron Spectroscopy (XPS) Reference Pages. [Online] [Cited: October 01, 2020.] http://www.xpsfitting.com/.

11. *Green and simple route toward boron doped carbon dots with significantly enhanced non-linear optical properties.* **Athanasios B. Bourlinos, Georgios Trivizas, Michael A. Karakassides, Maria Baikousi, Antonios Kouloumpis, Dimitrios Gournis, Aristides Bakandritsos, Katerina Hola, Ondrej Kozak, Radek Zboril, Irene Papagiannouli, Panagiotis Aloukos, Stelios Couris.** s.l. : Elsevier Ltd., 2015, CARBON, Vol. 83, pp. 173 – 179.

12. *One Step Radiosynthesis of 6-[18F]Fluoronicotinic Acid 2,3,5,6-Tetrafluorophenyl Ester ([18F]F-Py-TFP): A New Prosthetic Group for Efficient Labeling of Biomolecules with Fluorine-18.* **Dag E. Olberg, Joseph M. Arukwe, David Grace, Ole K. Hjelstuen, Magne Solbakken, Grete M. Kindberg, and Alan Cuthbertson.** 4, s.l. : American Chemical Society, 2010, Journal of Medicinal Chemistry, Vol. 53, pp. 1732–1740.

Chapter 6: General conclusion and future perspective

6.1 General conclusion

1. The analysis of antibodies for their number of moieties per mAb, conjugated with small ligands, can be carried out using different techniques, including direct titration, MALDI/TOF MS (Matrix-Assisted Laser Desorption-Ionization / Time Of Flight Mass Spectrometry) and UPLC/ESI-TOF MS (Ultra High Performance Liquid Chromatography / Electrospray ionization - Time Of Flight Mass Spectrometry).

2. The different analytical techniques show overall similar trends and values, although UPLC/ESI-TOF MS offers reliable quantitative information about the different species present when functionalization with the desferrioxamine derivative *p*-NCS-Bz-DFO is carried out.

3. TCO conjugation of Trastuzumab did not compromise its binding ability to the target. However, the characteristic to internalize after binding to its receptor was a potential problem. Yet, *in vivo* internalization studies showed remaining mAb (about 55 %) on the cell membrane 24 h postinjection.

4. Small, spherical AuNPs (core size 3-5 nm) functionalised with polyethyleneglycol and cobalt-bis-dicarbollide (COSAN), show slow elimination and high uptake in organs of the mononuclear phagocytic system, such as the spleen and the liver. Hence, they didn't follow the desired properties for pre-targeting.

5. Nontheless, high boron loading was achieved and tumor uptake due to the EPR effect could be witnessed in a xenograft mouse model of breast cancer.

6. Boron doped carbon dots show rapid elimination via kidneys and bladder, and therefore promising properties for pre-targeting. The use of a pretargeting strategy significantly increases retention of the boron-rich carbon dots in the tumour, as demonstrated using a xenograft mouse model of breast cancer.

6.2 Future perspective

Future studies should address the low tumor accumulation of the B-CDs in tumor tissue. Therefore several strategies can be followed. Using a non-internalizing mAb would lead to an increase of available mAb on the cell membrane at tumor site. Therefore, more dots could attach and be retained. Furthermore, a later administration of the B-CDs-Tz, that is, moving from 24 h to e.g. 48 h after the mAb injection, would enable enhanced clearing of the mAb from non-targeted tissue, hence, preventing the click reation with the dots to occur at other sites and increase their bioavailablity. Another way to enhance tumor accumulation could be to prolong the blood circulation time of the dots, which could, for example, be achieved by additional PEG liagnds, increasing size and biocompatibilty of the particles. It could increase the accumulation in tumor tissue, however, it is non-selective and could enhance uptake also

in non targeted tissues. Finally, the way of administration could be addressed. An alternative of giving a one time high dose could be a continus infusion which would allow more B-CDs to pass through the tumor and attach to the pre-injected antibodies, hence higher overall accumulation in tumor could be achieved.